論文 / 著書情報
Article / Book Information

題目(和文)	
Title(English)	Evaluation of Local Site Amplification in Lima, Peru using Earthquake Ground Motion Records
著者(和文)	ミレイビセレネキスペガメロ
Author(English)	Mileyvi Selene Quispe Gamero
出典(和文)	学位:博士（学術）, 学位授与機関:東京工業大学, 報告番号:甲第10016号, 授与年月日:2015年9月25日, 学位の種別:課程博士, 審査員:山中　浩明,田村　哲郎,浅輪　貴史,盛川　仁,松岡　昌志,海江田　秀志
Citation(English)	Degree:Doctor (Academic), Conferring organization: Tokyo Institute of Technology, Report number:甲第10016号, Conferred date:2015/9/25, Degree Type:Course doctor, Examiner:,,,,,
学位種別(和文)	博士論文
Type(English)	Doctoral Thesis

Evaluation of Local Site Amplification in Lima, Peru using Earthquake Ground Motion Records

Mileyvi Selene Quispe Gamero

Supervisor: Prof. Hiroaki Yamanaka

A Thesis presented to

the Department of Environmental Science and Technology

Tokyo Institute of Technology

September, 2015

ACKNOWLEDGEMENT

I would like to express my sincere gratitude to my supervisor Prof. Hiroaki Yamanaka and Dr. Kosuke Chimoto, professor and assistant professor of the Department of Environmental Science and Technology, Tokyo Institute of Technology, respectively, who sincerely supervised and guided me throughout my study. This study would not be possible without their significant contributions, enthusiasm, continuous motivation, comments and suggestions during this research.

I would like also to extend my gratitude to my thesis committee members: Professor Tetsuro Tamura, Prof. Takashi Asawa, Professor Hitoshi Morikawa and Prof. Masashi Matsuoka from Tokyo Institute of Technology, as well as Professor Hideshi Kaieda from Central Research Institute of Electric Power Industry for their fruitful suggestions, discussions and for reviewing the manuscript.

I am really indebted to Professor Zenón Aguilar, Professor Luis Fernando Lázares and Professor Diana Calderón from Japan Peru Center for Earthquake Engineering and Disaster Mitigation (CISMID), Lima, Peru as well as Professor Hernando Tavera from Geophysical Institute of Peru (IGP), for their highly intensive support in the preparation and execution of the field surveys and discussions. I would like also to express my thanks to the CISMID staff for their assistance during the field surveys, especially Mr. Armando Sifuentes and Mr. Carlos Gonzáles.

This study would not be possible without the Monbukagakusho (Ministry of Education, Culture, Sports, Science and Technology – Japan) Scholarship Student.

I would like to thank all my fellow lab-mates in Yamanaka lab: Dr. Hussam Eldein, Dr. Koichiro Saguchi, Rama san, Uddin san, Ozlem san,

Mohamed san, Tsuchiya san, Imai san, Sorimachi san, Nogami san, Kojima san, Noyori san, Hirose san, Liu san, Ishihara san, Harigaya san, Ishige san, Shimizu san, Seita san, Chujo san and Miyanaga san for their support and stimulating discussions, as well as for all the fun we have had together in the last three years. Thanks also to Shimamoto san for her assistance in the laboratory documents during my stay.

I would like to take this opportunity to express my love and gratitude to my parents and two brothers for their love, encouragement and support in all my life. I would like also to say thank you to my best friends Daniel, Alejandra, Yani and Faizah for their honest friendship and support during these last three years in Japan.

To all of you, I am eternally grateful.

TABLE OF CONTENT

ABSTRACT

The present thesis intends to contribute the state of the art of Earthquake Engineering as it exists in Peru today. The understanding of local site amplification in Peru is still poor due to the lack of knowledge, the limitation in data, and the access to it. Previous studies in Lima Metropolitan Area stress the obtained results are still in their preliminary stages. This work focuses on overcoming the above-mentioned limitations using as a reference these previous works. New results and contributions in relation to the evaluation of site response on ground motion are obtained in this study for Lima Metropolitan Area.

First off, measurement campaigns were carried out at sites based on the location of earthquake seismic stations. The selected sites were five sediment sites and one rock site. In this study, the SPatial Autocorrelation Coefficient (SPAC) technique was applied to define the S-wave velocity structure for the sediment sites, while the Multichannel Analysis of Surface Waves (MASW) method was used to determine the Vs model for the rock site. From the measurements conducted at sediment sites as well as using information from previous studies, this work concludes gravel deposits have S-wave velocities ranging from ~400 to ~1500 m/s which gradually increase with depth. The sand deposits have S-wave velocities that vary between ~100 and ~500 m/s, while the clays have S-wave velocities ranging between ~200 and ~500 m/s. This study also succeeded to estimate the 1-D S-wave velocity model at the rock site. The profile reached a depth of 30 m, where the bottom layer has a S-wave velocity of ~2200 m/s. This information is pivotal for the evaluation of site response in Lima Metropolitan Area.

The observed site response was also evaluated using earthquake ground motion records in the frequency range from 1 to 20 Hz. Most of the earthquakes used in the analysis were small events with a Local Magnitude ML between 4.0 and 5.0. The Spectral Inversion Method (SIM) was applied in order to analyze the amplification effects for earthquake recording stations installed on different surface conditions such as sands, clays, and gravels. This study reveals and explains how the sedimentary layers over the basement control the amplification in a wide frequency range. The

explanation is described based on the results estimated from the inversion technique (SIM), the microtremor measurements conducted around the stations and information consulted from previous studies. Results in relation to the path and source effects are also presented in this work. These parameters were previously unknown for Lima Metropolitan Area. The results indicate the estimated Qs-value for the crust and mantle in Lima is modeled as $95.6f^{0.66}$. Source factors for each earthquake – such as seismic moment and corner frequency – are also estimated.

This research was also focused on the determination of the frequency-dependent quality factor Qs for sedimentary layers. The observed site response estimated from the Spectral Inversion Method was inverted for the calculation of Qs. Qs as a function of frequency and S-wave velocity was classified into three groups – gravels, sands, and clays – based on the main soil formations over Lima Metropolitan Area. This study reveals frequency-dependent Qs has a strong influence on the site response for clays deposits, while the effect on gravels and sands is negligible.

Finally, this study succeeded to estimate the observed site response, as well as the parameters that control the amplification – the S-wave velocity distributions and the frequency-dependent Qs for the sedimentary layers, as previously explained. These three parameters – site response, S-wave velocity and frequency-dependent Qs – were previously unknown in Lima Metropolitan Area.

CHAPTER 1

INTRODUCTION

1.1 Location of Study Area

Lima Metropolitan Area or Lima, Peru is the name given to the area formed by the Province of Lima and the Province of Callao as shown in Fig. 1. This place located on the coast of the Pacific Ocean at a longitude of 77º03' west, and latitude of 12º04' south (Calderon D., 2012) currently counts on 49 districts, 43 districts belong to Lima Province and 6 districts belong to Callao Province. The geographic area is approximately 2,819.3 km^2, but the current urban area covers only about 800 km^2 with a population of more than 8 million (INEI, 2008). This place has the highest population over Peru mainly due to the fact that Lima Province is the capital of Peru. A quick growing of population is expected to occur in the following years for Lima Metropolitan Area (INEI, 2012).

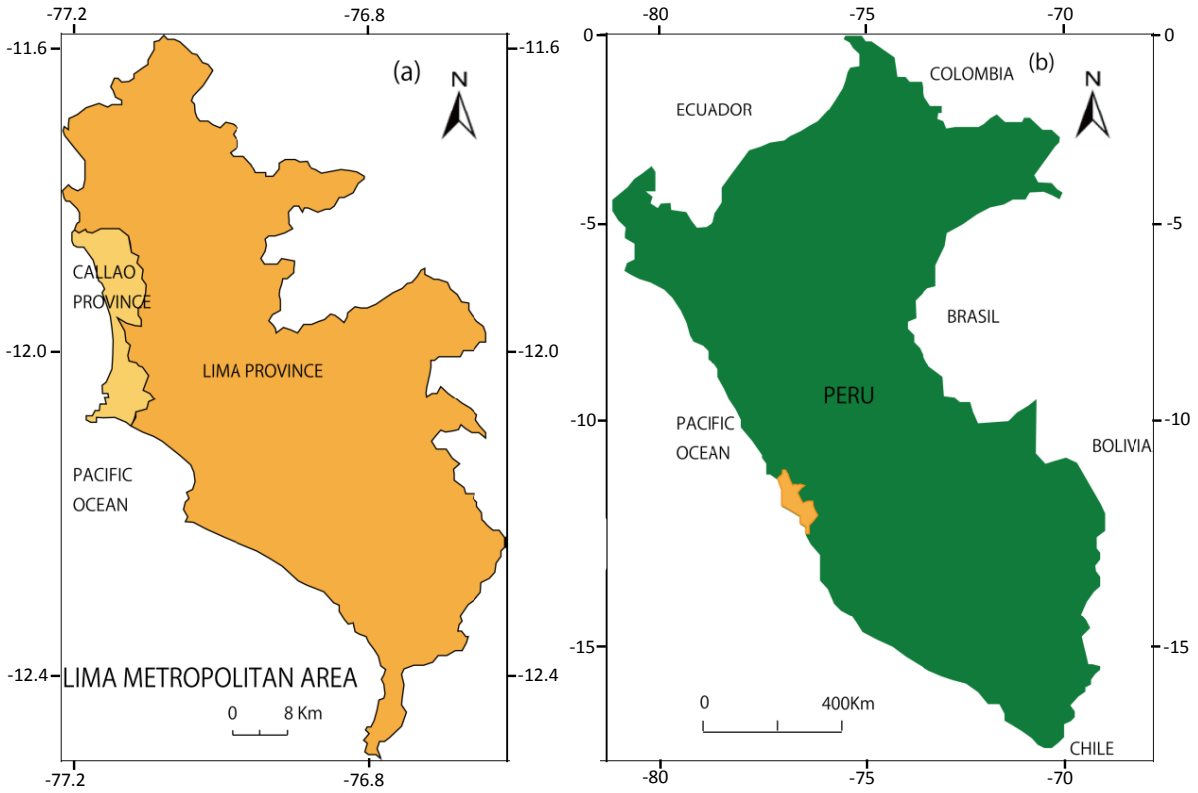

Figure. 1. Study area (adapted from Calderon D. (2012)). (a) Lima Metropolitan Area located in the central coast of (b) Peru.

1.2 Seismicity in Lima

The area used for this study, Lima Metropolitan Area in Peru, is situated in a seismically active region, due to subduction of the Nazca Plane beneath the South American Plate. Historical records show that large earthquakes ($Mw > 7.5$) have struck the region in the past. One of the most destructive events occurred in 1746 with a moment magnitude of ~8.8 (Dorbath et al., 1990). Subsequently, a period of quiescence that lasted almost two centuries followed. After this quiet period, Lima experienced some smaller events with magnitudes between 7.5 and 8.2 in 1940, 1966, 1974 and 2007 (Dorbath et al., 1990; Sladen et al., 2010). The damage caused for these earthquakes in Lima city varied from very severe to minor. The 1974 earthquake (Mw 8.0) is the last reported event that struck in front of Lima. High concentration of damages was observed upon the city. In particular, most of them were related to the local subsurface conditions of the soil. The damage distribution map induced by the 1974 earthquake was presented by Repetto, et al. (1984). This map was constructed based on the damage which is not related to structural details, but rather related to the local subsurface conditions. According to this map, areas underlain gravel deposits showed a very low concentration of damages (<<< 1%). Areas underlie soft sediments with a relatively large thickness; the concentration of damage was very high. For example, some areas the percentage of damage was over 50% such as La Molina district (Repetto et al., 1984).

Additionally based on the studies of Dorbath et al. (1990), Sladen et al. (2010) and Pulido et al. (2012), a megathrust earthquake like 1746 event is likely to affect Lima Metropolitan Area in the near future, given that Lima has not experienced any major earthquake since 1746. The estimated moment magnitude for this very large event might be larger than 8.8. Therefore, earthquake disaster mitigation is one of the important issues in Lima Metropolitan Area due to the impact that this natural disaster might have on Peruvian society regarding human losses and building damage.

1.3 Geological and Geomorphological Aspects

The geology of Lima Metropolitan Area reflects the complex tectonic process that Lima has been subjected in the past due to the subduction of Nazca Plate beneath South American Plate. The occidental branch of Andes Cordillera is observed in the eastern part of Lima with an elevation above 1000 meters as shown in Fig. 2. The main cause of the rise of Andes has been the compression of the two aforementioned tectonic plates (Jordan et al., 1983). Fig. 3 shows the geologic units of Andes Cordillera in the study area composed mainly of sedimentary and intrusive rocks from the Cretaceous age. Cretaceous deposits from the Puente Piedra group appear to the northwest of Lima, while deposits of the Morro Solar and Lima Groups are exposed in the southwest. In addition, rocks from the Casma Group outcrop in many parts of the city, and intrusive rocks are found exposed mainly in the eastern part of the study area.

Figure 2 displays that the Lima coastal plain is found between Andes Cordillera and Pacific Ocean. The plain's average elevation is less than 500 meters above sea level. According to the literature (Repetto et al., 1974; Le Roux et al., 2000; and CISMID, 2005), this plain lies on alluvial fan deposits from Chillón and Rímac Rivers as shown in Fig. 2. Both rivers have eroded deep valleys on the coastal plain in the past; especially Rímac River has had a big contribution in the formation of the plain, due to its short length, steep gradient and considerable flow. In the geologic past, a considerable amount of large-diameter material was transported from Andes Cordillera – the origin of the rivers – to the sea level. This material corresponds to the Quaternary deposits of Lima as shown in Fig. 3. Most of the Lima's population is concentrated in this area.

The geological map of Lima city (Fig. 3) shows that the Quaternary deposits are composed of alluvial, marine and aeolian material. The distribution of the alluvial materials is very wide. The alluvial deposits extend from the ground surface to the rock, and mainly consist of medium dense to very dense coarse gravel and sand with cobbles, known locally as Lima Conglomerate. The thickness of this material (to the base rock) is reported to be over 100 m.

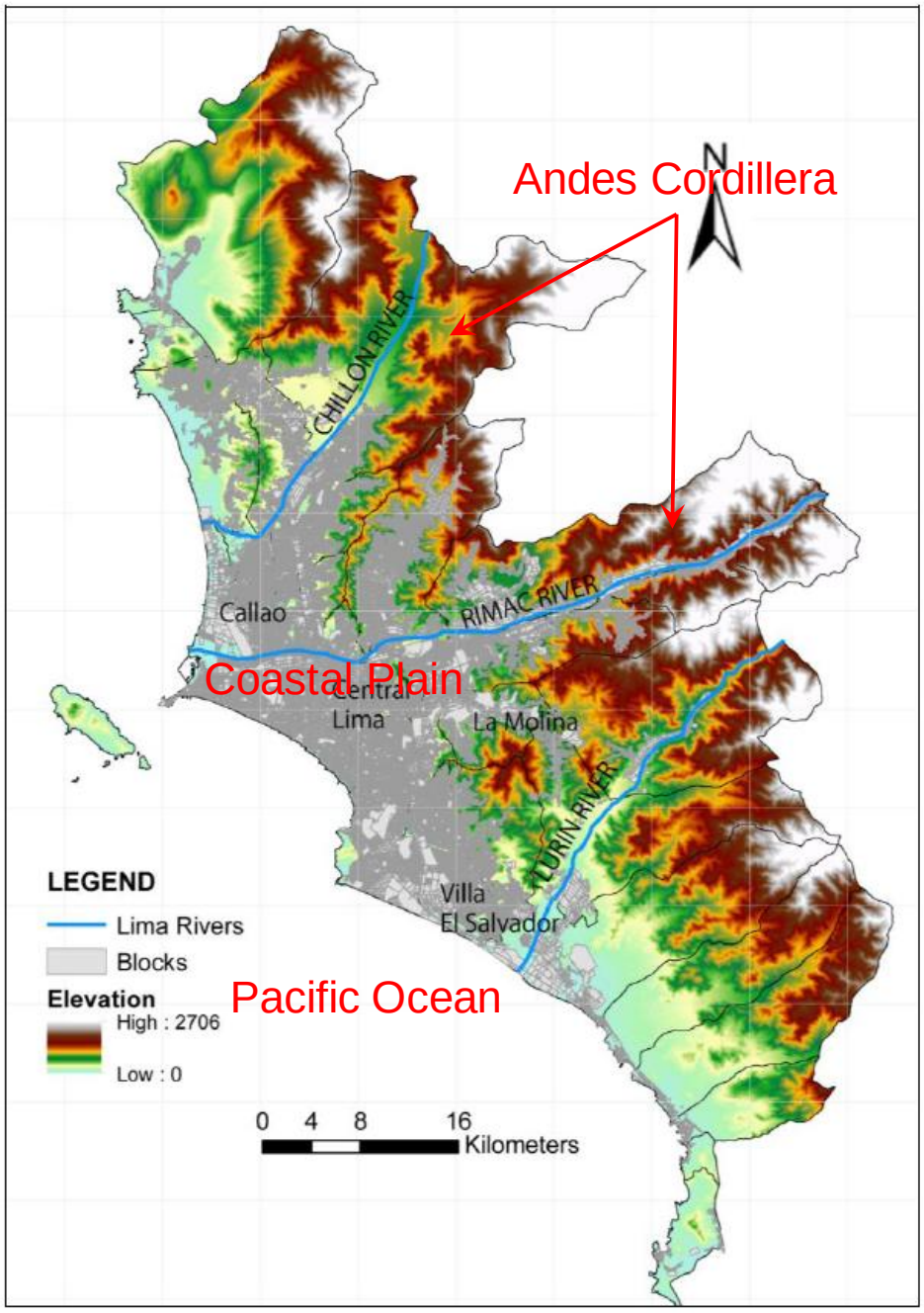

Figure 2. Elevation Map of Lima Metropolitan Area (adapted from Calderon D. (2012)).

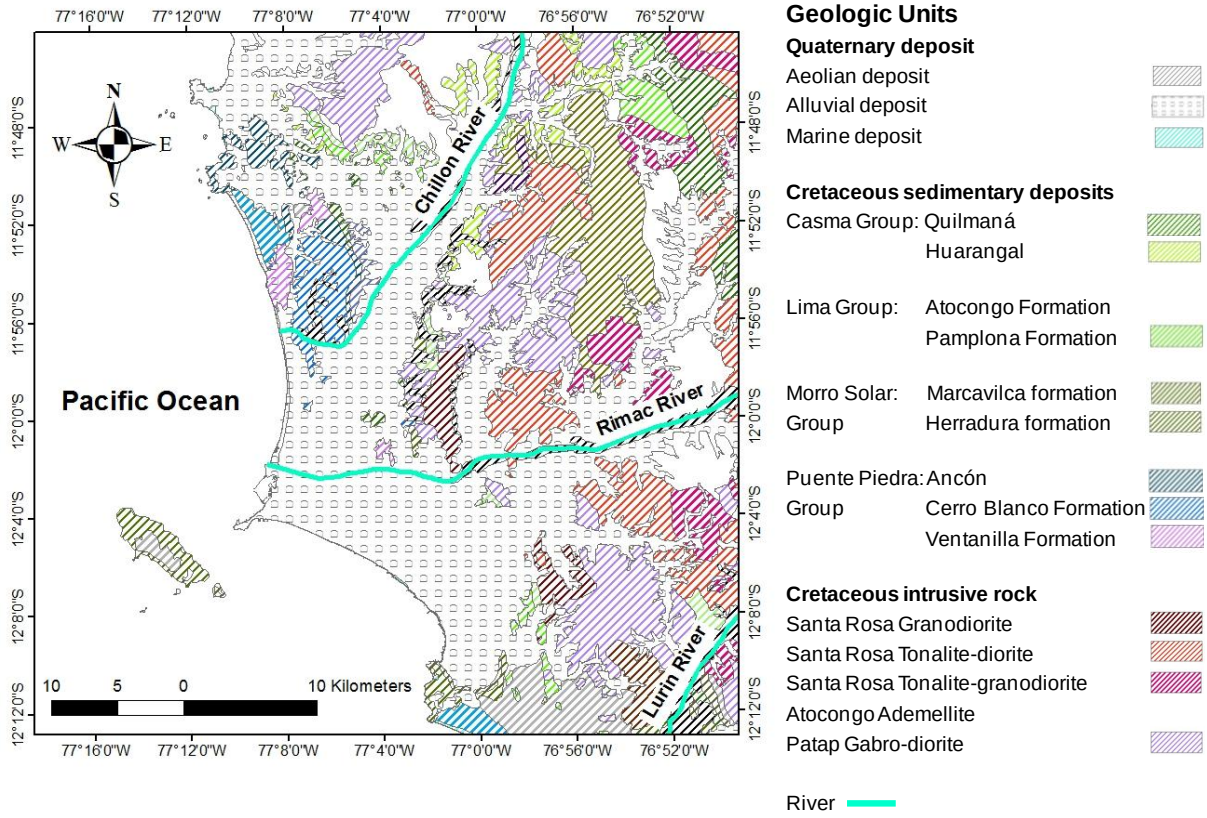

Figure 3. Geological map of Lima city (Martínez et al., 1975).

1.4 Summary of Previous Works on Site Amplification Effects in Lima

Based on the experience of past seismic events such as the last reported earthquake in 1974 (Mw 8.0) – high damage concentration was observed for areas underlying soft materials with a relatively large thickness – as well as the probability of occurrence of a megathrust earthquake with a moment magnitude 8.8 or larger which has been absent since 1746 (Dorbath et al., 1990; Sladen et al., 2010; and Pulido et al., 2012), a comprehensive study of Lima's soil dynamic characteristics started to be a major concern.

The seismic microzonation of Lima Metropolitan Area has mainly been studied as part of two projects. The first project took place from 2003 to 2005 and it was under the requirement and auspices of APESEG (Peruvian Association of Insurance Companies). Experts from Japan-Peru Center for Earthquake Engineering Research and Disaster Mitigation (CISMID), research center belongs to the National University

of Engineering (Lima, Peru), aimed to develop a preliminary geotechnical seismic microzonation map of Lima (CISMID, 2005 and Aguilar Z., 2005). In March 2010, another 5 years project entitled “Enhancement of Earthquake and Tsunami Disaster Mitigation Technology in Peru” started. This project recently finished in March 2015 and was sponsored by Japan Science and Technology Agency (JST) and Japan International Cooperation Agency (JICA). There was strong collaboration between Japanese and Peruvian researchers over the last 5 years, most importantly, the contribution of Japanese science and technology to earthquake disaster mitigation in Peru (Yamazaki F. and Zavala C., 2013).

Outcomes from these two projects are described in the following sections. It is important to mention results of these previous studies in Lima Metropolitan Area are the starting point in this research.

1.4.1 Soil Distribution Map of Lima

CISMID (2005) proposed a soil distribution map of Lima (Fig. 4) in order to obtain a more accurate picture of the distribution and properties of the various subsurface soils in Lima. A large number of geotechnical borehole logs and water well records were collected and consulted. Furthermore, a geotechnical investigation was conducted over Lima Metropolitan Area to define further the soil formations covering the study area. Figure 4 shows the main soil formations beneath Lima Metropolitan Area are composed of (CISMID, 2005 and Aguilar Z., 2005):

Alluvial gravels: This formation consists of thick alluvial deposits. This deposit appears in Rímac basin as well as some areas of Chillón and Lurín basins. This soil type covers a large portion of the study area, and presents a good geomechanic behavior.

Colluvial gravels: This formation consists of gravel deposits of considerable thickness. This material covers the hillsides and the bottom of outcropping rocks that surround the city. This soil type presents as good geomechanic behavior as alluvial

gravels, but in some areas this deposit is cemented by soluble salts making this material a collapsible soil.

Sand and silt deposits with a thickness of about ~10 m or less: This soil formation overlies the alluvial gravel with a thickness ranging from ~3 to ~10 m. The alluvial gravel is regarded as the layer with enough geotechnical stability for supporting shallow foundations of conventional structures.

Sand and silt deposits with a thickness from about ~10 to ~20 m: This soil formation overlies the alluvial or colluvial gravel with a thickness ranging from ~10 to ~20 m.

Sand and silt deposits with a thickness larger than ~20 m: This soil formation overlies the alluvial or colluvial gravel with a thickness larger than ~20 m.

Clay and organic soil deposits with a thickness of about ~10 m or less: This formation consists of sandy silts or clays with highly organic soils. The thickness of this deposit is less than ~10 m. The water table is from ~1 to ~3 m below the surface. Alluvial gravels from Rímac and Chillón basins underlie this unconsolidated material.

Thick layers of gravel and clay: Layers of gravel with a thickness from about ~10 to ~20 m overlie the clay deposits. These two soil materials – gravels and clays – alternate in depth. The water table is from ~1 to ~3 m below the surface.

Soft clay: This formation consists of soft saturated clays and organic soils with a thickness ranging from ~5 to ~15 m. The water table is from ~1 to ~2 m below the surface. Layers of gravels and clays alternating in depth underlie this soil type.

Aeolian sand: This formation consists of loose sands. This soil material has been transported and deposited by wind on the hillsides. In several areas, the aeolian sand is cemented by soluble salts making this soil type a collapsible material.

Swampy soils: This formation consists of clayey and organic soils. The water table is close to the surface. The bearing capacity of this soil type is quite low.

Lima cliffs: This steep surface reaches a height of up to ~80 m along the shore. Lima cliffs consist of alluvial gravels.

Marine sand deposits: This formation consists of loose sands. Soil liquefaction is expected in this soil type during large earthquakes.

Solid waste deposits: This deposit consists of solid wastes with a thickness ranging from ~5 to ~15 m.

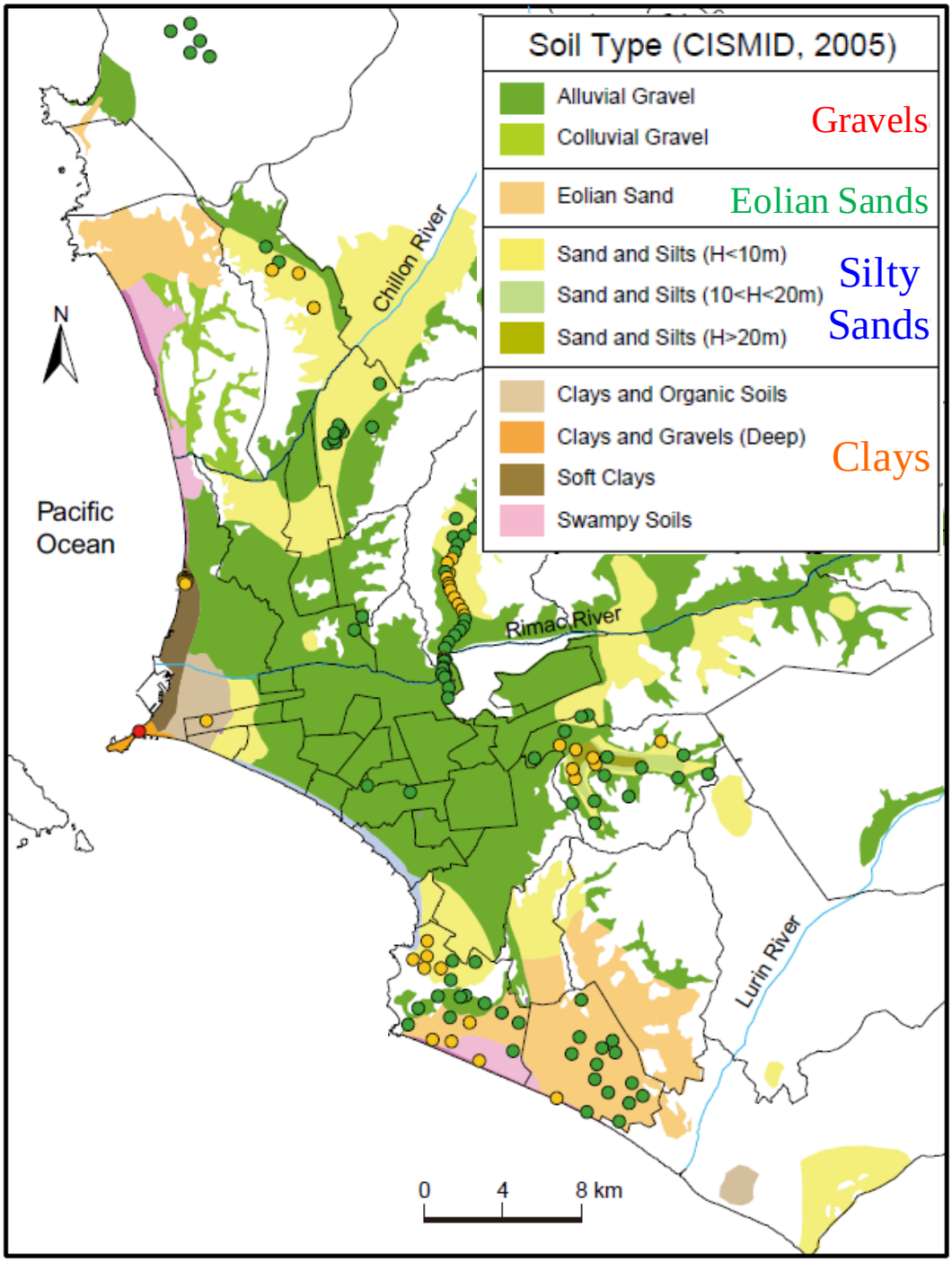

Figure 4. Soil Distribution Map of Lima (CISMID, 2005 and Aguilar Z., 2005).

1.4.2 H/V Peak Period Distribution Map

A comprehensive microtremor survey using the Horizontal-to-Vertical (H/V) spectral ratio technique was conducted under APESEG project in order to know the dynamic properties of soil deposits in Lima Metropolitan Area (CISMID, 2005). This information was previously unknown. Calderon D. (2012) gathered all this data (CISMID, 2005) as well as data from another project (CISMID, 2010), and plot all this information on a map as shown in Fig. 5. Each point represents the fundamental predominant period observed from microtremor data.

Although the information existed many years ago (CISMID, 2005; 2010), there was not an official map with the location of the microtremor measurements as displayed in Fig. 5. CISMID (2005, 2010) concluded most of the soil formations over Lima have a predominant period in the range between 0.0 and 0.2 sec, represented by green points in the figure, while some soil deposits have a predominant period over 0.4 sec, represented by orange and red points.

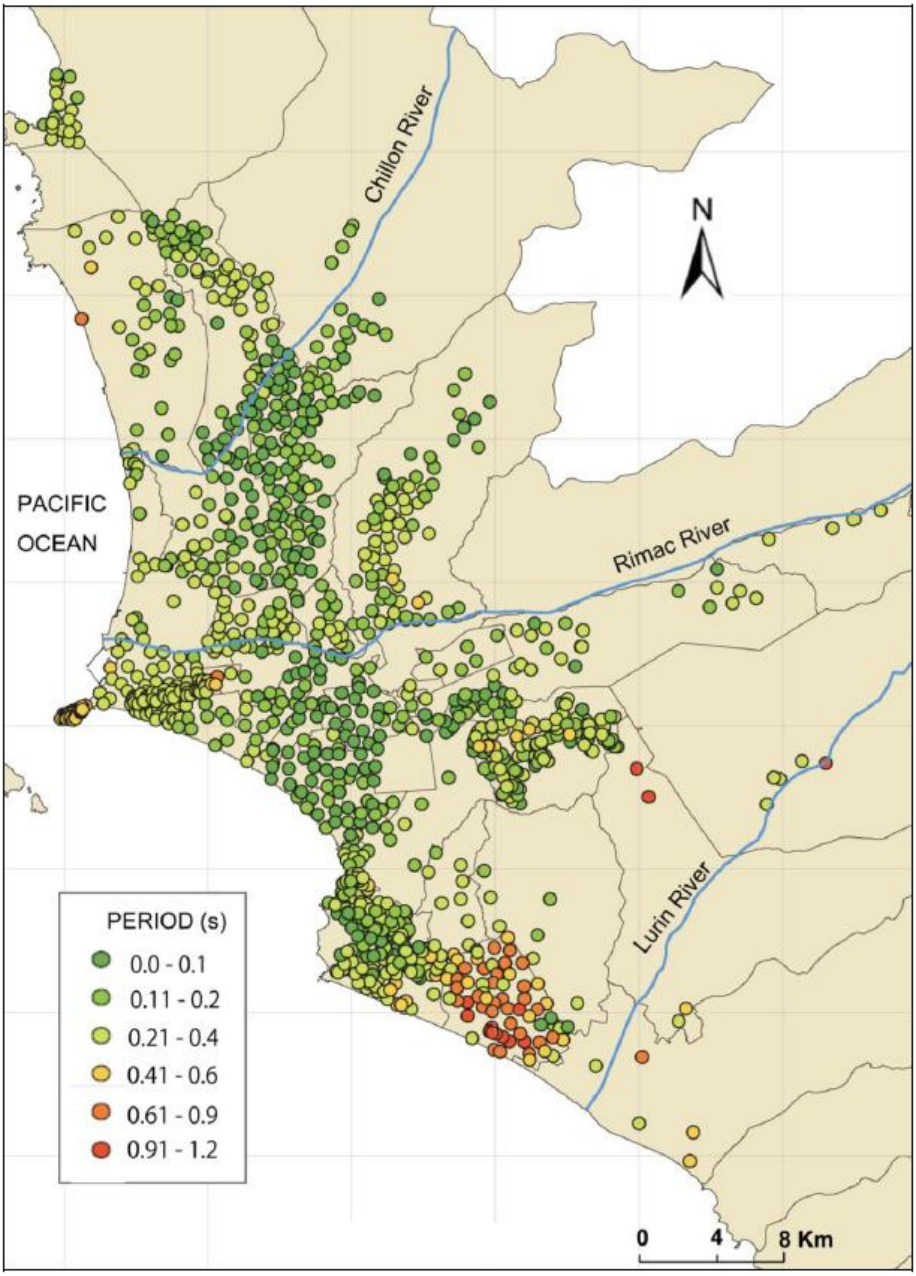

Figure 5. H/V Peak Period Distribution Map (Calderon D., 2012).

1.4.3 Zonation Map

Based on the Soil Distribution Map of Lima (Fig. 4) as well as information obtained from the dense microtremor observations (Fig. 5), the zonation map of Lima Metropolitan Area was proposed (CISMID, 2005; 2010) as shown in Fig. 6. This map is the first attempt to estimate and map the dynamic characteristics of all soil

formations covering Lima Metropolitan Area. The zonation zones were classified into five groups.

Zone I: The soil formation in this zone consists of outcropping rocks and alluvial gravel deposits from Rímac and Chillón basins. The predominant period of the soil materials in this zone varies from 0.1 to 0.3 sec. The soil formations included in this zone present the best geotechnical characteristics for building foundation. This zone classifies as Type I Soil according to the seismic code.

Zone II: The soil formation in this zone consists of sand and silt deposits with a thickness ranging from ~3 to ~10 m, and this overlies alluvial and colluvial gravel deposits. The predominant period of the soil materials in this zone varies from 0.3 to 0.5 sec. This zone classifies as Type II Soil according to the seismic code.

Zone III: The soil formation in this zone consists of aeolian sand and silt deposits. This soil type appears to the northern and southern of Lima. The predominant period of the soil materials in this zone varies from 0.5 to 0.7 sec. This zone classifies as Type III Soil according to the seismic code.

Zone IV: The soil formation in this zone consists of aeolian sands, saturated marine sands, and swampy soils, as well as deposits of thick layers of gravel and clay are also included in this zone. The predominant period of the soil materials in this zone is expected to be larger than 0.7 sec. This zone classifies as Type IV Soil according to the seismic code.

Zone V: This zone is composed of solid waste deposits with a thickness ranging from ~5 to ~15 m. This material has been used as a foundation material for construction, creating severe foundation engineering problems, related to bearing capacity. There is no information concerning the engineering characteristics of solid waste deposits, so this material is not considered in the seismic code.

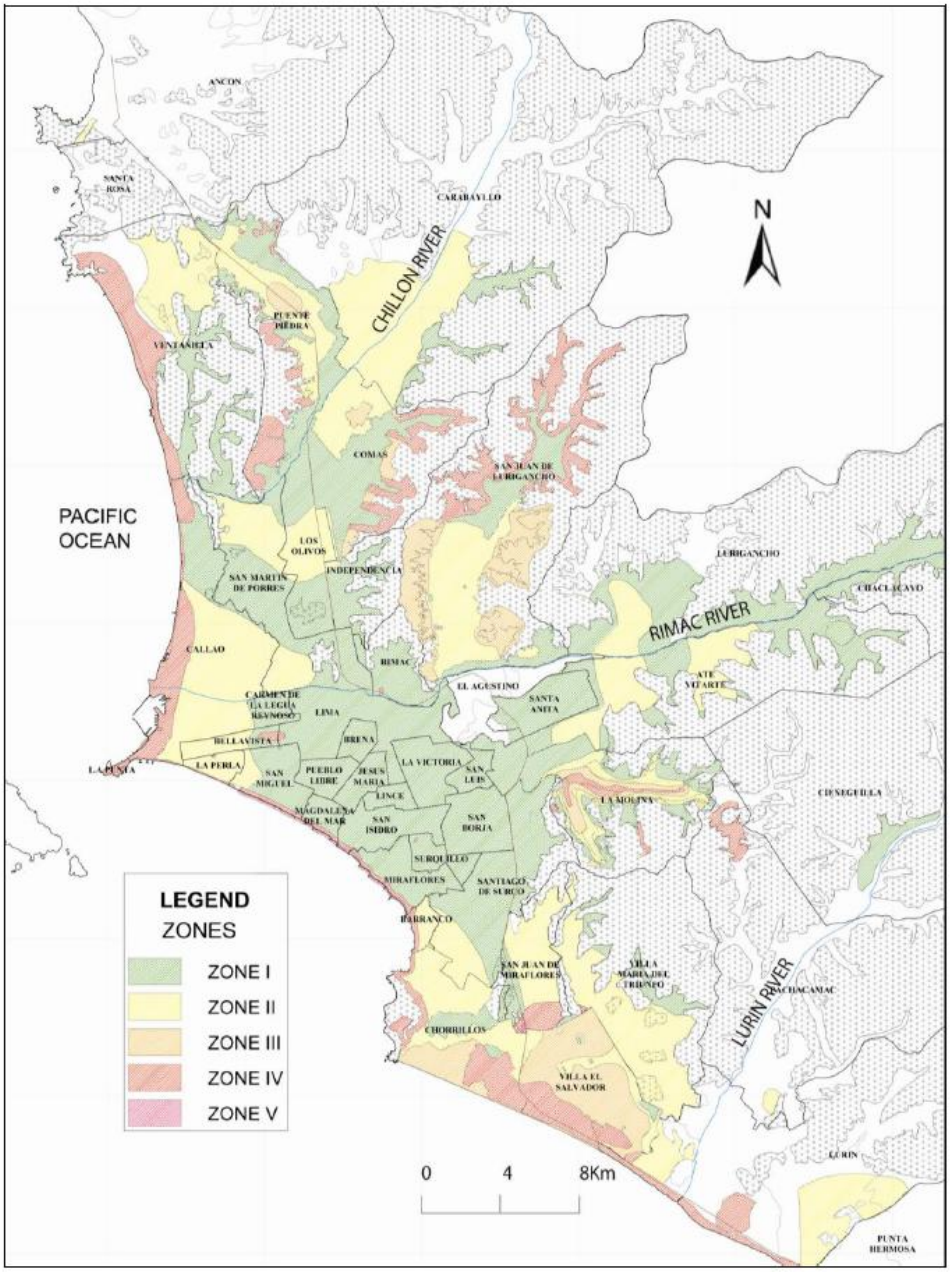

Figure 6. Zonation Map (CISMID, 2005; 2010).

1.4.4 Exploration of S-wave Velocity Structure

It is well-know that, S-wave velocity (Vs) profile is one of the important parameters for assessing the site effects of earthquake ground motion (e.g., Horike, 1985). Calderon D. (2012) and Sekiguchi et al. (2013) stress the zonation map (CISMID 2005; 2010) is still preliminary due to the lack of information on S-wave

velocity structure for estimating the site amplification. One of the main objectives of the JICA/JST project was the determination of S-wave velocity of sedimentary layers reaching the seismic basement. Calderon et al. (2012) conducted microtremor measurements to estimate the Vs structures of shallow and deep soil formations in Lima Metropolitan Area. The selection of the sites was based on the location of seismic recording stations, as well as places where a high concentration of damage has previously occurred during previous earthquakes. The microtremor array measurements were carried out at eight sites within the city. Calderon et al. (2012) estimated the seismic basement has a S-wave velocity of ~3 km/s.

1.4.5 Amplification Map for Lima Metropolitan Area

One of the important outcomes of the five-year JICA/JST project has been the amplification map for Lima Metropolitan Area proposed by Sekiguchi et al. (2013). The $AVs10$ (average S-wave velocity for the top 10 m of soils) map was first assessed before the developing of the amplification map. Fig. 7 displays the $AVs10$ map for Lima. Subsequently, the amplification map was produced based on correlations between $Avs10$ and three more parameters: elevation, H/V peak period, and soil type. Fig. 8 displays the soil amplification map for the study area.

The author mentions the current amplification map proposed by Sekiguchi et al. (2013) was constructed based on Vs profiles. The profiles used do not reach a depth more than 30 meters; therefore the estimated amplification is due to the contribution of the shallow soil structure. Amplification caused by the shallow and deep sedimentary layer over the basement is still unknown.

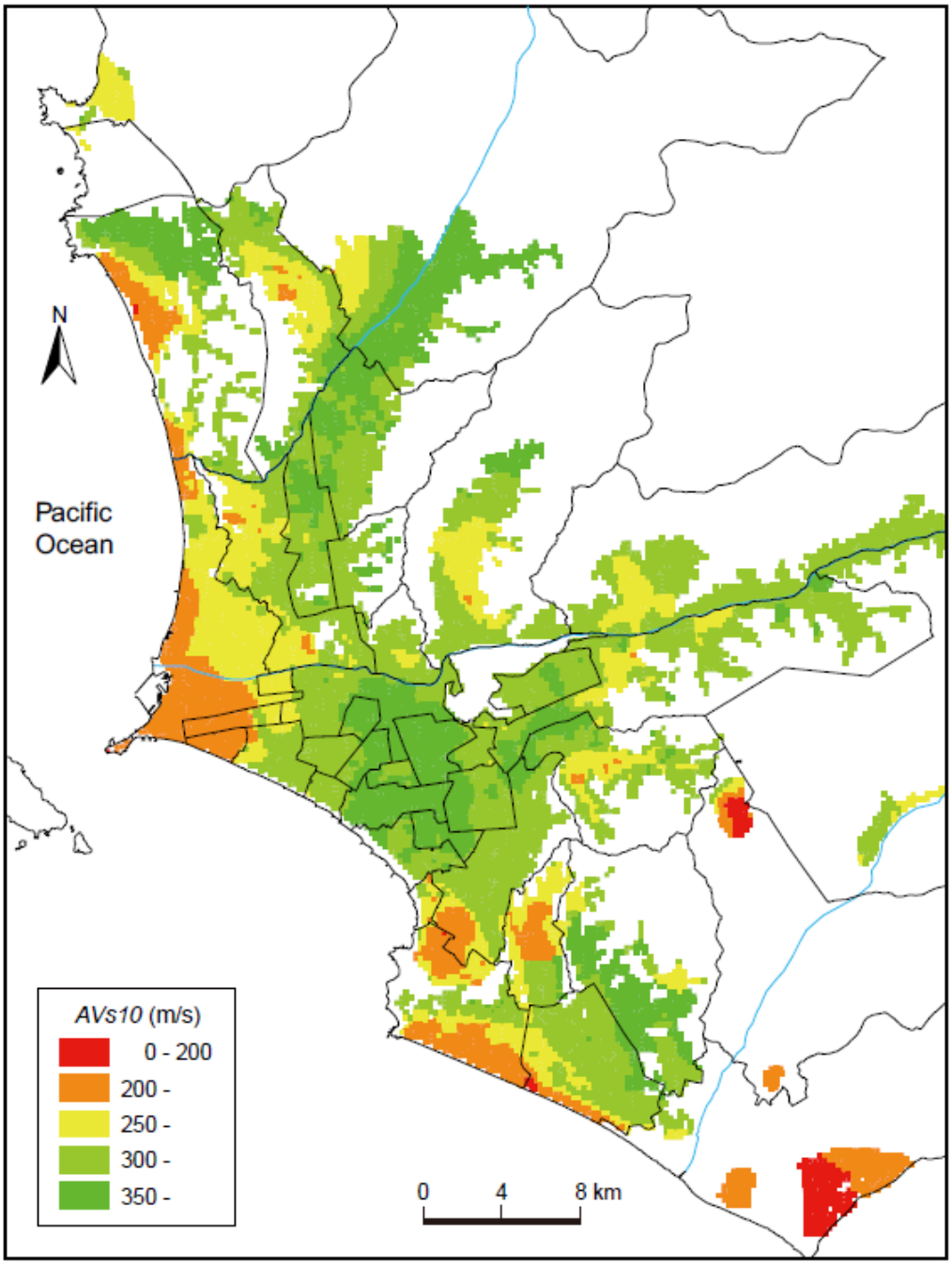

Figure 7. AVs10 map for Lima Metropolitan Area (Sekiguchi et al., 2013).

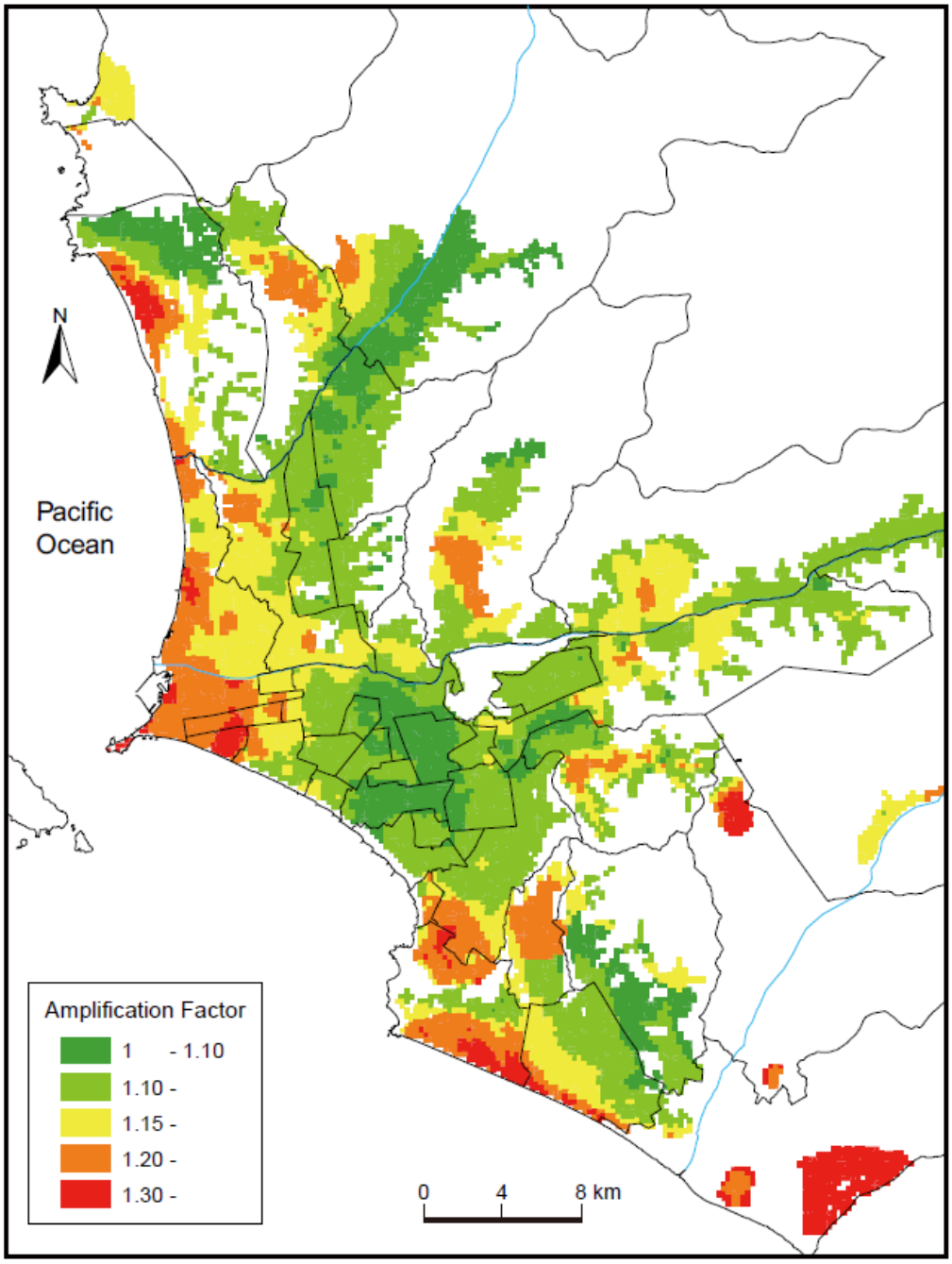

Figure 8. Soil amplification map for Lima Metropolitan Area (Sekiguchi et al., 2013).

1.4.6 Evaluation of Observed Site Response using Earthquake Ground Motion Records

Part of the JICA/JST project was the evaluation of the observed site response using ground motions records (Quispe et al., 2013), however the authors stress the assessment is still in its preliminary stages mainly due to the lack of knowledge, the limitation in data, and the access to it. Quispe et al. (2013) applied the Spectral Inversion Method (Iwata and Irikura, 1988) to earthquake recordings observed along the Pacific coast of Lima, Peru, for site response estimation. The information used was limited regarding the number of earthquake stations and consequently the number of seismic records, so their study stresses to reanalyze their results with new data in order to overcome this limitation as well as to have a better understanding how the subsurface conditions control the factors of site amplification in the frequency range of interest.

1.4.7 Collection of Earthquake Ground Motion Records

As mentioned in the section 1.4.6, the limitation of Quispe et al. (2013)'s study was the number of earthquake stations and consequently the number of seismic records. In Lima Metropolitan Area, the strong motion instruments are operated by two institutions: Japan-Peru Center for Earthquake Engineering Research and Disaster Mitigation (CISMID) and Geophysical Institute of Peru (IGP). By 2011, there were working 04 stations maintained by CISMID (blue solid triangles) and 06 stations maintained by IGP (red solid triangles), as shown in Fig. 9. Most of the earthquake data recorded by these stations were not available to the public at that time, and because of that the study of Quispe et al. (2013) just analyzed the site response of few stations. Before the doctoral program started in 2012, several requests were done in order to get this information formally. This study succeeded to have open access to the earthquake data recorded before 2011 and for the coming years until the end of this research.

Stations represented by blue and red solid triangles show the distribution of the seismic network over Lima by 2011, as displayed in Fig. 9. The number of stations was few, and that is why 10 new seismic recording stations were installed over Lima in 2011 during the project “Enhancement of Earthquake and Tsunami Disaster mitigation Technology in Peru” (Calderon, D., 2012). The new equipments are represented by blue open triangles in Fig. 9, and they are operated by CISMID. The author was truly involved in the installation of the new stations as shown in Fig. 10. Events recorded by these new equipments were also included in the analysis of this research

The author expresses without the effort to collect the earthquake data before this research started in October, 2012 until the end of the program, this study would not succeed. Conclusions and contributions from this research will be explained in the following chapters.

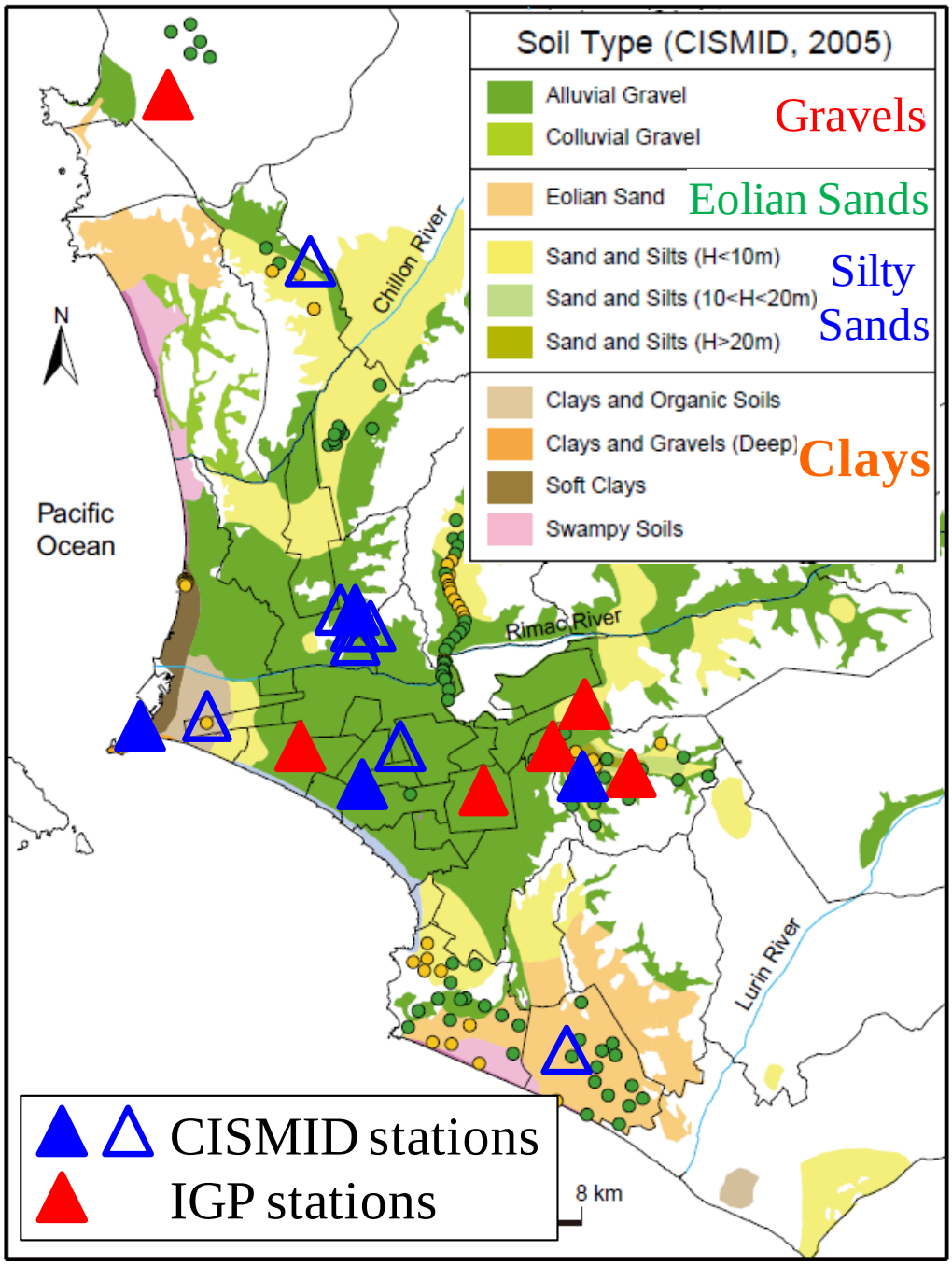

Figure 9. Distribution of the earthquake recording stations over the soil distribution map of Lima (CISMID, 2005). The blue and red triangles represent stations operated by Japan-Peru Center for Earthquake Engineering Research and Disaster Mitigation (CISMID) and Geophysical Institute of Peru (IGP), respectively. The blue open triangles indicate the new stations installed over Lima during the project "Enhancement of Earthquake and Tsunami Disaster mitigation Technology in Peru" in 2011.

Figure 10. Installation of one new seismic recording station over Lima Metropolitan Area in 2011. The author was also involved in the installation of the new equipments as shown in this picture. The picture was taken from this website http://ares.tu.chiba-u.jp/peru/E/meeting/meeting_110401.html.

1.5 Motivation and Objectives

The author would like to start expressing first the present thesis intends to contribute the state of the art of Earthquake Engineering as it exists in Peru today. Several years have already passed since seismic hazard assessment in Peru started to be a major concern of the government, but the understanding of local site amplification is still poor compared to develop countries such as Japan. Consequently, the works previously described (Calderon et al., 2012; Sekiguchi et al., 2013, Quispe et al., 2013) stress the seismic microzonation map of Lima (CISMID, 2005; 2010) – presented in the Section 1.4.3 – is still in its preliminary stages because the evaluation of the site response for the different soil conditions over Lima has still not been analyzed. Site amplification is controlled by two parameters the S-wave velocity Vs and the quality factor Qs. Site amplification, Vs and Qs were unknown when the seismic microzonation was proposed. This study is focused in evaluating these three parameters – site amplification, Vs, and Qs – in order to include the results obtained from this work and improve the microzonation map as a future work. In this part, it is important to mention again the big effort that was done for collecting the earthquake

data before this doctoral program started in October, 2012 (as explained in Section 1.4.7), without this effort this study would not succeed. Based on what the author just expressed, the main objectives of the present thesis are:

- Estimation of S-wave velocity profiles for sediment and rock sites, based on the location of earthquake stations.
- Assessment of site amplification effects using actual ground motion data.
- Determination of S-wave frequency dependent quality factor Qs for sedimentary layers.

This research was focused on these results since they are relevant and urgent for earthquake disaster mitigation in Peru. The author states again outcomes from this research will be included for the improvement of the seismic microzonation map of Lima Metropolitan Area.

1.6 Thesis Organization

Chapter 1 presents the background of this study. Main facts about the study area are explained in this chapter, such as location, seismicity, and geology. This chapter also presents a summary of previous works in Lima Metropolitan Area, as well as the author's motivation and main objectives in this research.

Chapter 2 explains and discusses the results in relation to the measurement campaigns conducted at 05 sediment and one rock sites in order to estimate S-wave velocity distributions in soil deposits. The target sites were based on the location of seismic earthquake stations installed in Lima Metropolitan Area. Vs profiles conducted at sediment sites are described from a geotechnical point of view in order to understand how the subsurface condition affects ground motion. Results regarding S-wave velocity with depth at the rock site are also described, useful information for site response evaluation.

Chapter 3 presents the assessment of site response in Lima Metropolitan Area using ground motion data. The earthquake observation network and ground motion records used are shown in this section. The technique Spectral Inversion Method applied in this work is also described. Results obtained from this methodology such as path, source and site effects are explained and discussed. Inversion results related to site response are compared with spectral ratio techniques in order to discuss which technique is the most appropriate and accurate for analyzing site amplification. In this section, how the surface conditions control the amplification effects in a wide frequency range is explained too. Correlations for estimating site amplification using average S-wave velocity are proposed in this study in order to be used in Lima Metropolitan Area.

Chapter 4 presents the determination of frequency-dependent quality factor Qs for different soil conditions in Lima Metropolitan Area. The observed site response calculated from the spectral inversion method is inverted in order to estimate Qs as a function of frequency and S-wave velocity. In this section, the influence when estimating the theoretical transfer function with frequency-dependent Qs is also discussed.

Chapter 5 presents the outcomes from this research as well as future tasks that should be completed.

CHAPTER 2

ESTIMATION OF S-WAVE VELOCITY PROFILES FROM MICROTREMOR EXPLORATIONS

2.1 Site Selection

The knowledge of S-wave velocity distribution in soil deposits and basement is one of the key parameters controlling amplification of seismic motion (e.g. Zaineh et al., 2012). Measurement campaigns were conducted at sites based on the location of earthquake seismic stations. Calderon et al. (2012) conducted an extensive campaign of microtremor measurements around several seismic stations operated by Japan-Peru Center for Earthquake Engineering Research, and Disaster Mitigation (CISMID); nonetheless stations maintained by Geophysical Institute of Peru (IGP) were not included in their program. In this study, the selected sites were the six stations operated by IGP stations, five stations installed on sedimentary layers (Quispe et al., 2014) and one rock site.

Figure 11 shows the location of the earthquake observation network in Lima represented by triangles on the soil distribution map of Lima (CISMID, 2005). The red and blue triangles are the stations maintained by IGP and CISMID, respectively The target sites for this study are represented by green (sediment sites) and pink (rock site) pentagons, while the grey pentagons indicate the location of microtremor measurements conducted by Calderon et al. (2012) at CISMID stations.

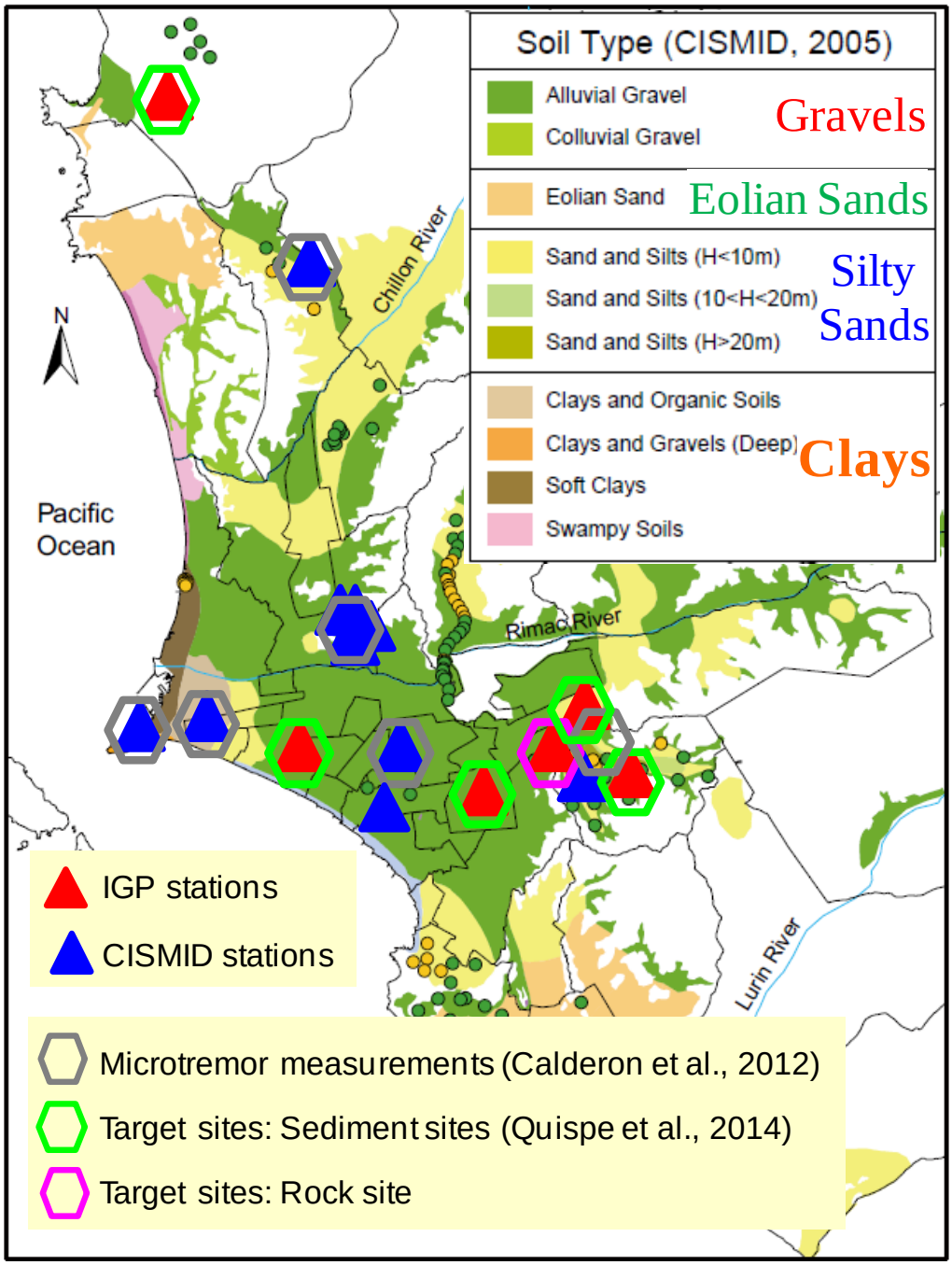

Figure 11. The soil distribution map of Lima (CISMID, 2005) with location of earthquake stations represented by triangles. Red and blue triangles indicate the stations operated by IGP and CISMID, respectively. In this study, the selected sites for determining the Vs structure around IGP stations are represented by green (stations installed on sedimentary layers) and pink pentagons (rock site). In this figure is also shown the microtremor measurements conducted at CISMID stations by Calderon et al. (2012), represented by grey pentagons.

2.2 Estimation of Vs Structure at Sediment Sites

Microtremor array measurements were conducted at IGP sediments sites (PUCP, CER, MAY, RIN, and ANC) in order to define the Vs structure (Quispe et al., 2014). This technique is becoming more and more popular in worldwide due to the fact that it is affordable, not time-consuming, and can be conducted in urban and crowded areas such as Lima Metropolitan Area. This research has applied the Spatial Autocorrelation Coefficient (SPAC) method introduced by Aki (1957) and Okada (2003) to extract the dispersion curve of Rayleigh waves from microtremor measurements. Then, the Genetic Simulated Annealing Algorithm technique (Yamanaka, 2007) was applied for the inversion of the phase velocity dispersion curve in order to estimate the 1-D S-wave velocity model.

2.2.1 Array Configuration

A circular array configuration was applied throughout the observation. Figure 12 shows the schematic layout of the installation. Seven 3-component sensors were placed on the ground's surface: six were distributed at the vertices of two equilateral triangles inscribed within two circles of different radii, and one was placed at the center (Grutas et al., 2012). For each site, the size of the array (side length of equilateral triangle) varied from small to large. Small arrays (the smallest was 1.5 m) gave information of the near-surface layers, while the large ones characterized deeper soil layers. Although large arrays with side lengths larger than 300 m were conducted for all the sites, the coherence was so low at a low frequency that it was not possible to use data from the large arrays in the analysis for most sites. The size and number of deployed circular arrays that defined the observed phase velocity dispersion curve for each site is presented in Table 1.

The test equipment used in this exploration was a GPL-6A3P portable recording systems designed by the Mitutoyo Corporation, which has a flat response in the frequency range between 0.25 to 25 Hz for estimating the phase velocity (Grutas et al.,

2012). Each recording lasted between 10 and 60 minutes, and data were recorded at a sampling rate of 100 samples per second.

Figures 13 (a) and (b) show the installation of the equipments for conducting the microtremor measurements. As mentioned previously, the distribution of the sensors followed the schematic layout illustrated in Fig. 12.

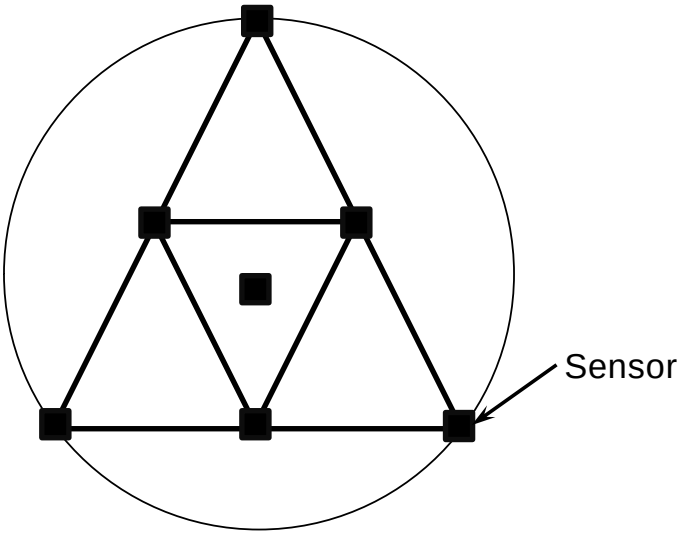

Figure 12. Geometry of the microtremor array.

Table 1. Array information.

Site ID	Location (District)	Latitude (deg)	Longitude (deg)	Array Min* (m)	Array Max* (m)	Number of deployed arrays
PUCP	San Miguel	-12.0734	-77.0796	1.5	346.4	4
CER	San Borja	-12.1040	-76.9992	1.5	48.0	3
MAY	Ate	-12.0549	-76.9441	1.5	173.2	4
RIN	La Molina	-12.0873	-76.9240	1.5	48.0	3
ANC	Ancón	-11.7767	-77.1510	1.5	173.2	4

*Side length of equilateral triangle

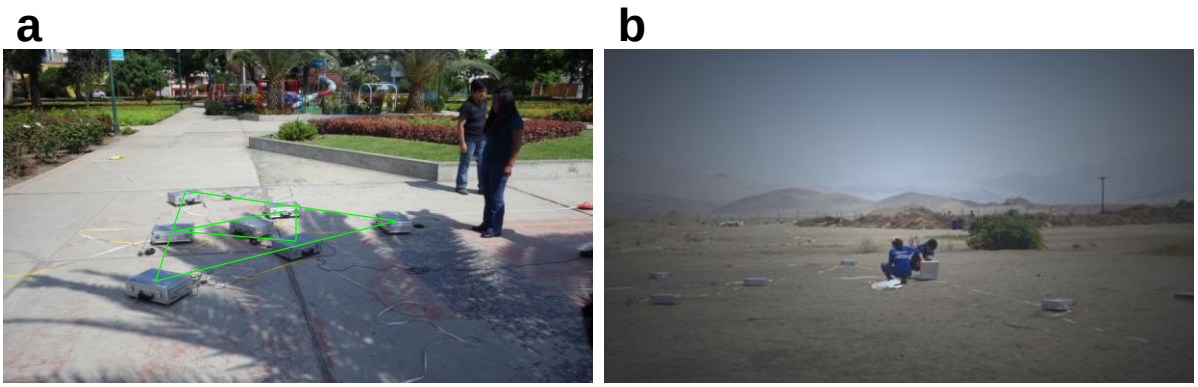

Figure 13. Installation of the equipments for conducting the microtremor measurements at (a) CER and (b) ANC sites, respectively.

2.2.2 Estimation of Phase Velocity Dispersion Curve

The Spatial Autocorrelation Coefficient (SPAC) method was applied in this study to define the observed dispersion curve of Rayleigh waves from array data. This technique uses SPAC coefficients, $\rho(r,\omega)$, in the calculation of phase velocity at different frequency ranges. Spatial autocorrelation coefficients are defined as the average SPAC function at all observation sites on the circular array with same sensor separation distance, r, and sampled many different azimuths, θ. Assuming stationary of microtremors, Aki (1957) showed that

$$\rho(r,\omega) = J_0\left(\frac{r\omega}{c(\omega)}\right) \quad (1)$$

where $c(\omega)$ is the phase velocity at frequency ω at the site, and $J_0(\blacksquare)$ is the Bessel function of the first kind and the order zero. SPAC coefficients can be directly calculated in a frequency domain using the Fourier transform of microtremors, that is,

$$\rho(r,\omega) = \frac{1}{2\pi}\int_0^{2\pi} \frac{real\,[S_{CX}(\omega;r,\theta)]}{\sqrt{S_C(\omega;0,0)\cdot S_X(\omega;r,\theta)}} \quad (2)$$

where real [·] stands for the real part of cross spectrum $S_{CX}(\omega; r, \theta)$ between one record obtained at coordinate (r, θ) and the record obtained at the center of the circle $(0,0)$, and $S_C(\omega; 0,0)$ and $S_X(\omega; r, \theta)$ are the power spectra of microtremors at sensors located at coordinates $(0,0)$ and (r, θ), respectively. SPAC coefficients are obtained by averaging the coherence functions with regard to the azimuth, θ, where the coherence functions are defined as the real part of cross spectrum $S_{CX}(\omega; r, \theta)$ at sensor pairs with same separation distance, r, and normalized by the power spectrum of microtremors, as shown in Eq. (2). Phase velocity is calculated from Eq. (1) by fitting SPAC coefficients to the Bessel function. Details relating to SPAC analysis can be found in literature (Aki, 1957; Okada, 2003).

Using the assumption that Rayleigh waves mainly dominate vertical motion, vertical records from each sensor were analyzed in the processing of data. The microtremor recording data were divided into time segments with lengths of 81.92 sec, and time segments clearly contaminated by noise were removed.

Figures 14 (a) and (b) illustrate the SPAC coefficients for small and large arrays recorded at the RIN and PUCP sites, respectively. In this study, a seven-sensor configuration was used to obtain measurements, Fig. 14 (a) and (b) show five SPAC coefficients for each array that correspond to five combinations of sensor separation distances.

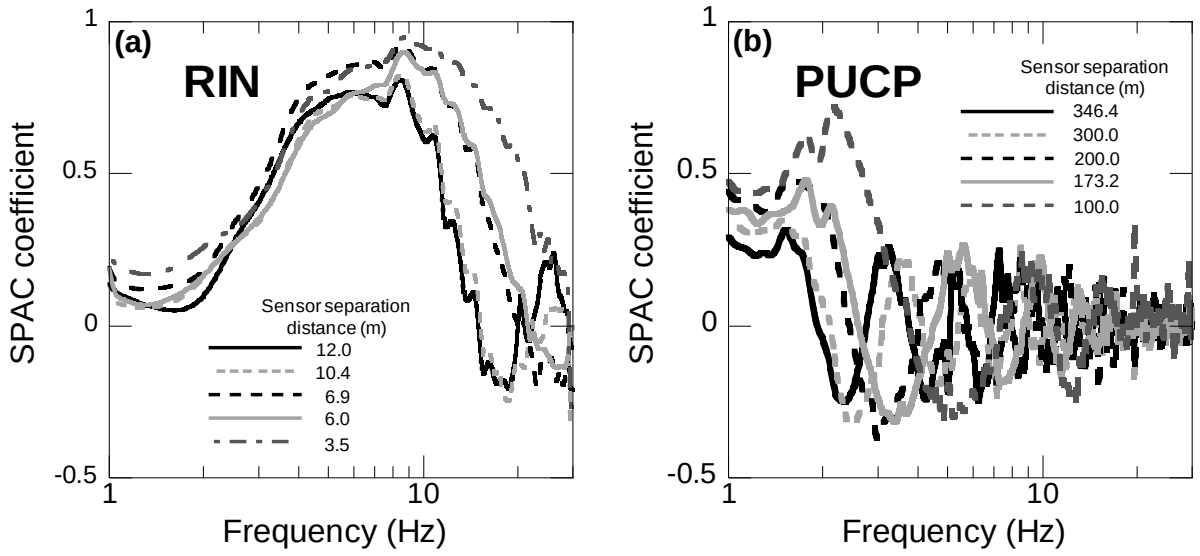

Figure 14. SPAC coefficients as a function of frequency for different sensor separation distances at (a) the RIN site (with a maximum side length of 12.0 m) and (b) the PUCP site (with a maximum side length of 346.4 m).

Figure 15 shows the observed dispersion curves recorded at the sediment sites. For all sites, the phase velocities were estimated in the frequency range from 4 to 30 Hz, except for at the PUCP site, which had the widest frequency range until 1 Hz (due to the contribution from large arrays with a maximum side length of 346.4 m, that were used when exploring the deeper structure of the soil). In term of the velocity, Fig. 15 shows that the phase velocity values vary from between 200 and 2000 m/s. The PUCP and MAY sites reached the highest velocity values of ~2000 m/s at frequencies of ~1 Hz and ~4 Hz, respectively. The high velocity layer (~2000 m/s) at the MAY site suggests a shallower basement depth than at the PUCP site. Table 2 displays the values of the observed phase velocity dispersion curve estimated from the microtremor measurements for each site.

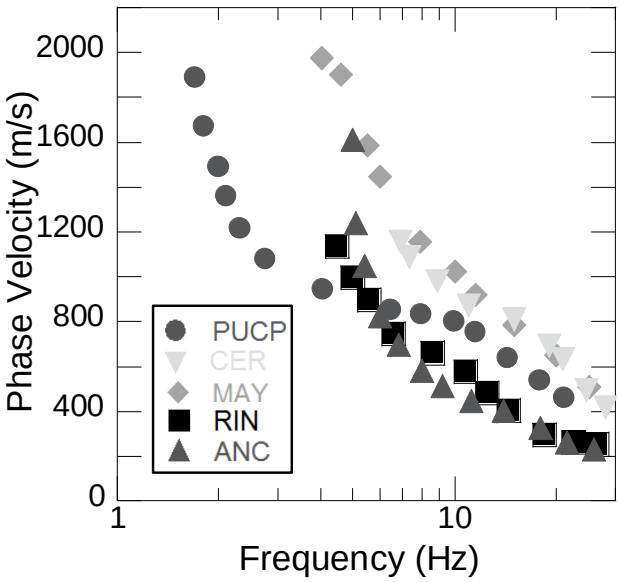

Figure 15. Observed dispersion curves obtained from microtremor data using the SPAC technique.

Table 2. Values of the observed phase velocity dispersion curve estimated from the microtremor measurements for each site.

PUCP		CER		MAY		RIN		ANC	
Freq	**Phase Vel**	**Freq**	**Phase Vel**	**Freq**	**Phase Vel**	**Freq**	**Phase Vel**	**Freq**	**Phase Vel**
1.71	1882.6	6.91	1154.7	4.04	1976.6	4.50	1134.3	5.00	1612.3
1.82	1669.3	7.32	1089.1	4.60	1903.5	5.00	995.4	5.10	1237.6
2.01	1485.4	8.91	978.6	5.51	1586.6	5.60	896.7	5.41	1046.1
2.12	1356.1	11.01	870.3	6.01	1447.1	6.60	744.3	6.01	825.3
2.33	1210.8	15.00	808.3	7.91	1156.2	8.61	656.5	6.81	697.2
2.76	1075.6	19.10	692.1	10.01	1023.3	10.80	576.5	8.01	578.9
4.10	938.9	21.01	634.8	11.51	917.4	12.50	482.2	9.20	510.2
6.51	849.4	24.61	495.6	15.00	782.2	14.50	403.1	11.21	445.1
8.01	827.4	28.00	416.8	20.01	650.0	18.51	296.7	14.00	403.7
10.06	798.3			25.01	505.3	22.51	259.1	18.01	324.4
11.60	750.2					26.47	251.5	21.51	259.5
14.50	633.8							26.00	228.7
18.01	533.9								
21.30	456.8								
26.05	370.8								

2.2.3 Estimation of Vs profile

SPAC analysis provides the dispersion curve of Rayleigh waves, and this is subsequently inverted using the Genetic Simulated Annealing Algorithm technique to determine a 1-D S-wave velocity model at each of the sediment sites. The inversion technique was introduced by Yamanaka (2007), and it searches model parameters to fit (as much as possible) the observed model, $U_0(f_i)$, with the calculated values of phase velocity for fundamental mode Rayleigh waves, $U_C(f_i)$, by using the misfit function $\emptyset_j$ defines as:

$$\emptyset_j = \frac{1}{N}\sum_{i=1}^{N}[U_0(f_i) - U_C(f_i)]^2 \quad (3)$$

where N and f_i represent the number of the observed data and frequency, respectively. In the calculation of the final optimal Vs model, 10 inversions with 100 generations were conducted using different random numbers. In doing so, good models with a smaller amount of misfit were more likely to survive in the next generation, and poor models were replaced by newly generated ones. The unknown parameters to be determined in the inversion were Vs and thickness. P-wave velocities and densities of the layers were fixed. P-wave velocity value was calculated using the equation proposed by Kitsunezaki et al. (1990) that correlates Vs and Vp values, as previously used by Calderon et al. (2012) in the same study area. Density values were set from 1.8 to 2.5 g/cm^3, depending on the soil type. The fundamental mode of Rayleigh waves was assumed in the inversion, as well as the knowledge that Vs increases with depth. Table 3 shows an example of the search limits at the RIN site.

Table 3. Search limits used for the determination of the optimal Vs profile at the RIN site.

Search limits			
Layer	**Vs (km/s)**	**Thickness (m)**	**Density (g/cm^3)**
1	[0.20-0.30]	[1-15]	1.8
2	[0.30-0.45]	[1-15]	1.9
3	[0.45-0.60]	[1-15]	2.0
4	[0.60-0.95]	[25-55]	2.1
5	[0.95-1.45]	-	2.2

Figure 16 shows the extent that the calculated dispersion curve (solid line) fits the observed one (open circles) for all the selected sites. All models are able to sufficiently explain the observed phase velocity in the entire frequency range. The inverted 1-D Vs profiles for all the sediment sites are shown in Fig. 17 and Table 4. The deepest profile was obtained for the PUCP array, with a depth over 280 m over the bottom layer and a S-wave velocity of ~2500 m/s, while the CER site (where the bottom layer has a lower velocity than 2500 m/s) only reached a depth of ~50 m. Fig. 17 displays the top layers at the PUCP, CER, and MAY sites show S-wave velocities of ~400 m/s, whereas the RIN and ANC sites show S-wave velocities of ~200 m/s; this is related to the phase velocity at the upper-limit of frequency. The phase velocities for PUCP, CER, and MAY at 30 Hz are relatively larger than those at the RIN and ANC sites (as shown in Fig. 16). All the Vs profiles estimated from the microtremor campaign detected the engineering bedrock, with a Vs larger than 500 m/s. A further description of the S-wave velocity structure is discussed in the following section.

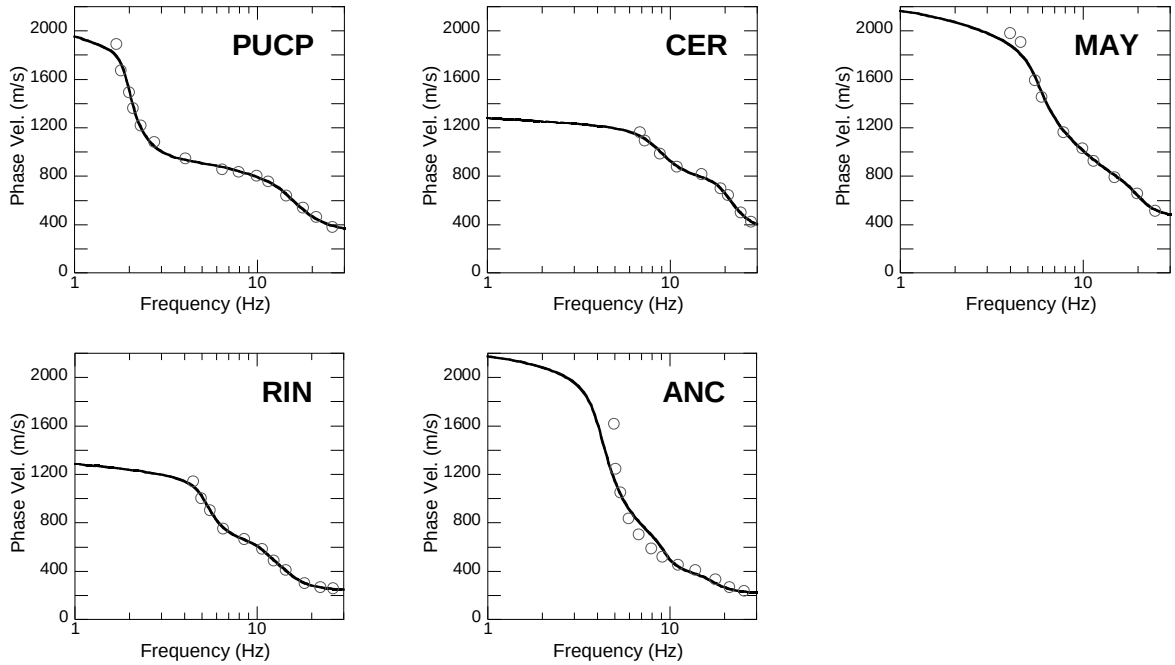

Figure 16. Comparison between the calculated dispersion curves (solid line) for inverted models and the observed ones (circles) for all sites.

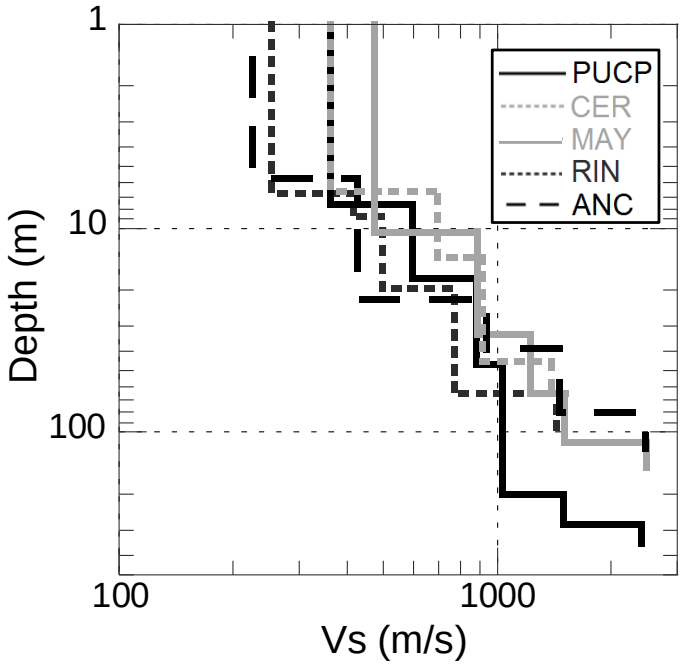

Figure 17. Estimated shear-wave velocity profiles.

Table 4. Estimated S-wave velocity structures from array observations of microtremors.

PUCP		CER		MAY	
Vs (m/s)	**Thickness (m)**	**Vs (m/s)**	**Thickness (m)**	**Vs (m/s)**	**Thickness (m)**
362	7.7	364	6.6	474	10.4
596	9.9	695	7.3	888	22.6
884	28.5	911	31.2	1225	31.3
1038	153.8	1396	-	1518	47.9
1503	82.9			2492	-
2412	-				
RIN		**ANC**			
Vs (m/s)	**Thickness (m)**	**Vs (m/s)**	**Thickness (m)**		
254	6.8	225	5.7		
418	2.0	429	16.7		
496	11.0	938	16.7		
769	44.7	1468	40.2		
1431	-	2477	-		

To support the validity of the results obtained from the inversion, the horizontal to vertical (H/V) spectral ratio calculated from the observed microtremor data (solid line) was compared with the theoretical ellipticity of the fundamental-mode Rayleigh wave from the inverted 1-D soil profile (broken line), as depicted in Fig. 18. The observed H/V spectrum was estimated from the recording data of the sensor placed at the center of the array configuration, which was smoothed using a Parzen window with a 0.05 Hz bandwidth. The comparison between the observed H/V and the computed ellipticity shows good agreement in the frequency range within 1 and 10 Hz. The dominant peaks observed in the spectral ratios of observed microtremor data were well modeled by the computed ellipticities of the Rayleigh waves.

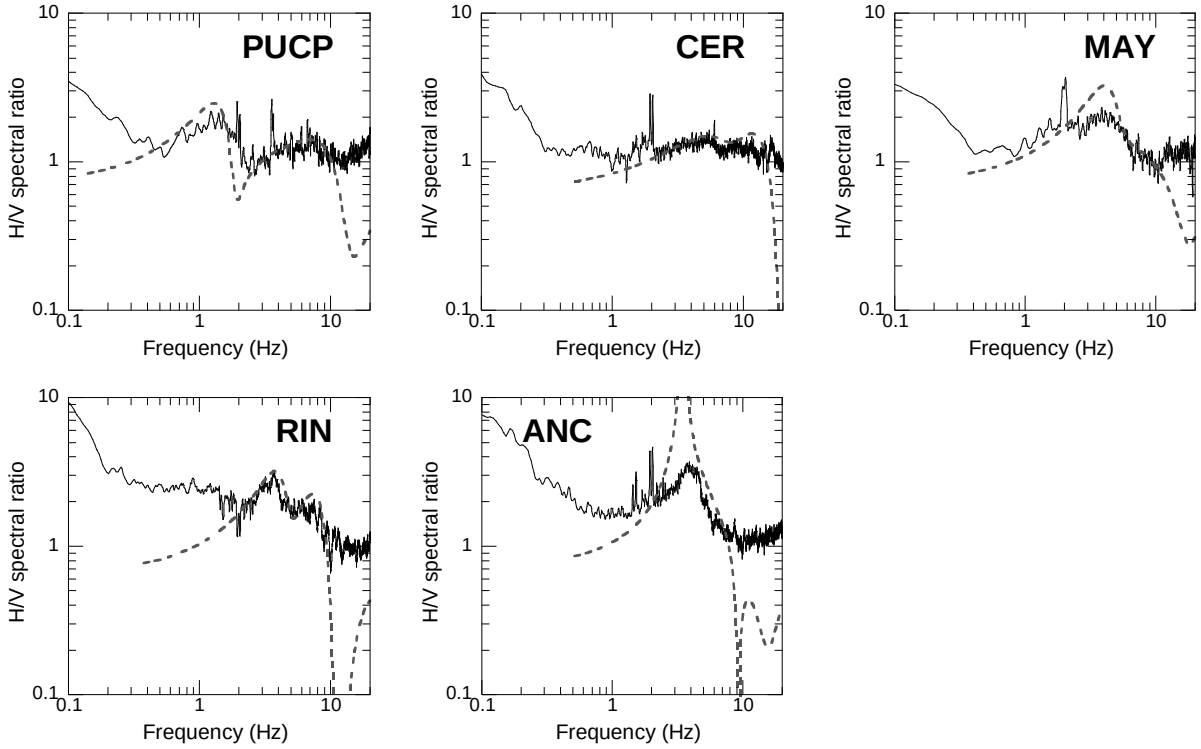

Figure 18. Comparison of H/V spectra of microtremors (solid lines) with computed ellipticities of fundamental-mode Rayleigh waves based on the obtained S-wave velocity structure (broken lines).

2.2.4 Geotechnical Description of Vs profile at sediment sites

All the Vs profiles at the sediment sites estimated in the present study are located on alluvial Quaternary deposits as shown in Fig. 19 (Quispe et al., 2014), but the subsurface condition for each site differs. Lima conglomerate is the predominant material over Lima city (Repetto, et al., 1980; Aguilar, Z., 2005; CISMID, 2005). Overlying the conglomerate, shallow layers of unconsolidated material such as sand, silt, or clay are found, and their thicknesses range from ~0.5 m to more than 30 m, depending on the location (Repetto, et al., 1980; Aguilar, Z., 2005; CISMID, 2005). CISMID (2005) proposed a soil distribution map of Lima (Fig. 4) in order to obtain a more accurate picture of the distribution and properties of the various subsurface soils in Lima. Sekiguchi et al. (2013) grouped the subsurface conditions into four soil types –gravels, silty sands, eolian sands, and clays– in order to simplify the variety of soil materials. Figure 20 displays the soil classification map of Lima with location of the Vs profiles at the sediment sites determined in this study.

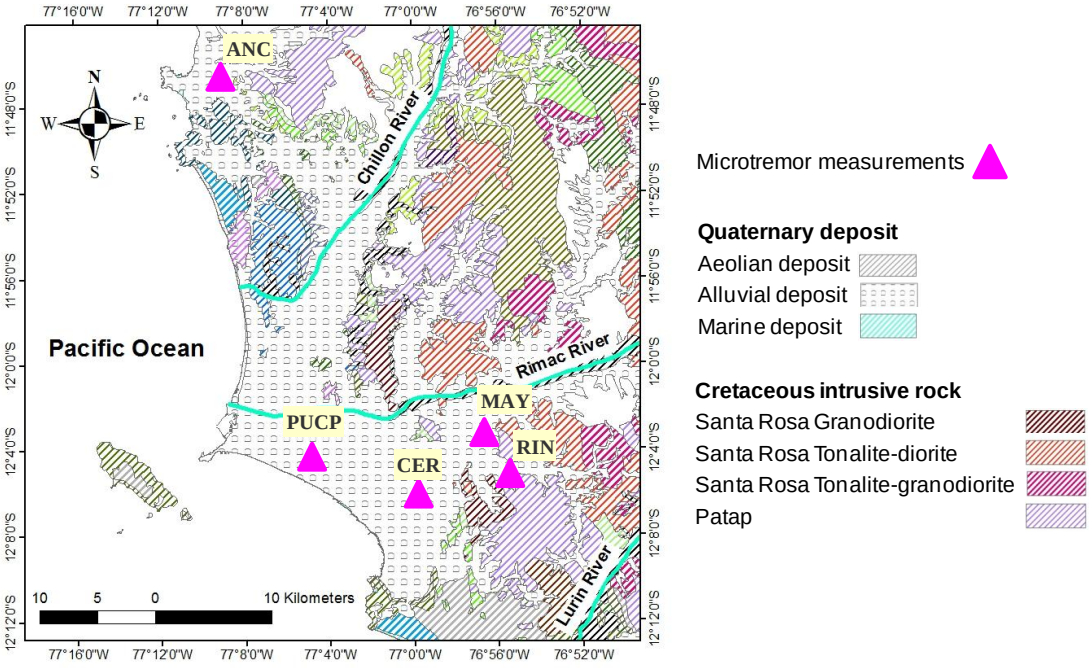

Figure 19. Geological map of Lima Metropolitan Area (Martínez et al., 1975) with location of microtremor measurements at sediment sites conducted in this study (Quispe et al., 2014).

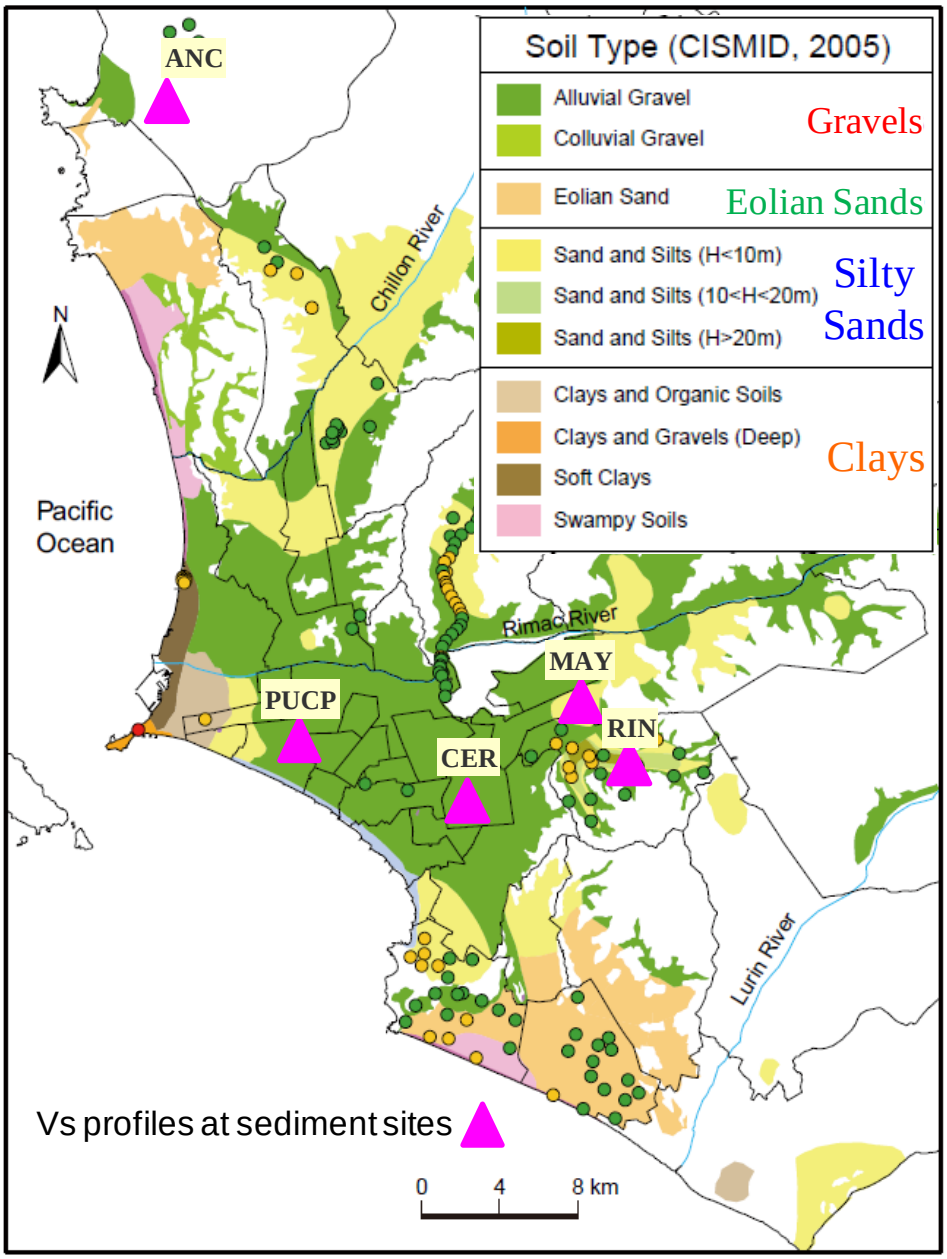

Figure 20. Soil Distribution Map of Lima Metropolitan Area (CISMID, 2005) with location of Vs profiles at sediment sites (Quispe et al., 2014).

According to the soil distribution map (CISMID, 2005), the PUCP and CER sites are located on gravels. The Vs profiles at the two sites show that the Lima conglomerate extends from near the ground's surface, with a Vs larger than ~400 m/s (Fig. 17). The PUCP site proves that Lima conglomerate, especially in the central part of the city, has a thickness of about 20 m, as previously reported by CISMID (2005)

using water well records. The S-wave velocity of the conglomerate increases gradually with depth from ~400 to ~1500 m/s, as shown in Fig. 17 (PUCP Vs profile).

In the eastern part of the city, sand and silt deposits overlie the Lima conglomerate (CISMID, 2005), and MAY and RIN array measurements were carried out on these materials. The results obtained from the microtremor measurements conducted in this study show that this deposit has S-wave velocities ranging within ~200 and ~500 m/s (Fig. 17), which is similar to that reported by Repetto et al. (1974) using a down-hole test. The RIN site is located in the La Molina district, a place where a high concentration of damage has previously occurred during previous earthquakes, due to the local subsurface conditions (Repetto et al., 1974; Bill Stephenson et al., 2009; Calderon et al., 2012). The Vs profile at RIN shows that the thickness of the sand and silt deposits is about 20 m, while the thickness in the Vs structure at MAY is about 10 m. Conglomerate is found underlying this unconsolidated material, with a Vs of between ~500 to ~1500 m/s. The MAY profile detected shear wave velocities of ~2500 m/s at a depth of over 120 m, and this high velocity layer (~2500 m/s) was also detected in the PUCP profile at a depth of over 280 m (Fig. 17); it is considered that this material may correspond to bedrock. Calderon et al. (2012) reported that the bedrock at Lima Metropolitan Area has S-wave velocity values of the order of 3000 m/s.

The ANC site is located on the outskirts of Lima to the north (Fig. 20). The soil distribution map of Lima Metropolitan Area proposed by CISMID (2005) provides scarce information related to the area where the earthquake observation coded ANC is located. Nonetheless, geological and geotechnical information indicates that layers of aeolian san overlie alluvial gravel deposits (CISMID, 2005). The Vs profile at ANC shows the top layers has S-wave velocities between ~200 to ~400 m/s, and this overlies thick high velocity layers (within ~1000 and ~1500 m/s) and a very high velocity layer (~2500 m/s).

2.2.5 S-wave velocity Ranges for the Different Subsurface Soil Conditions over Lima Metropolitan Area

After the S-wave velocity profiles were estimated at the IGP sediment stations (Quispe et al., 2014), this information was gathered with the profiles determined by Calderon et al. (2012) in order to propose the S-wave velocity ranges for the different soil formations over Lima Metropolitan Area. This information is still unknown in the study area. The predominant soil materials are gravels, sands – silty and aeolian sands – and clays.

Figure 21 displays the location of the profiles estimated by Calderon et al. (2012) and Quispe et al. (2013) on the soil distribution map of Lima (CISMID, 2005), represented by blue and red solid triangles, respectively. The total number of the profiles used is thirteen, eight models estimated by Calderon et al. (2012) and five models determined by Quispe et al. (2014). Profiles estimated at the same subsurface soil condition – gravels, sands, and clays – were gathered and plotted together as shown in Fig. 22. The blue and red lines indicate the profiles estimated by Calderon et al. (2012) and Quispe et al. (2014), respectively. Figure 22 (a) displays the S-wave velocity of the gravel deposits increase gradually with depth from ~400 to ~1500 m/s. The sand deposits have S-wave velocities that vary between ~100 and ~500 m/s, as shown in Fig. 22 (b). The few Vs profiles at clay deposits reveal this material have S-wave velocities ranging within ~200 and ~500 m/s, as displayed in Fig. 22 (c).

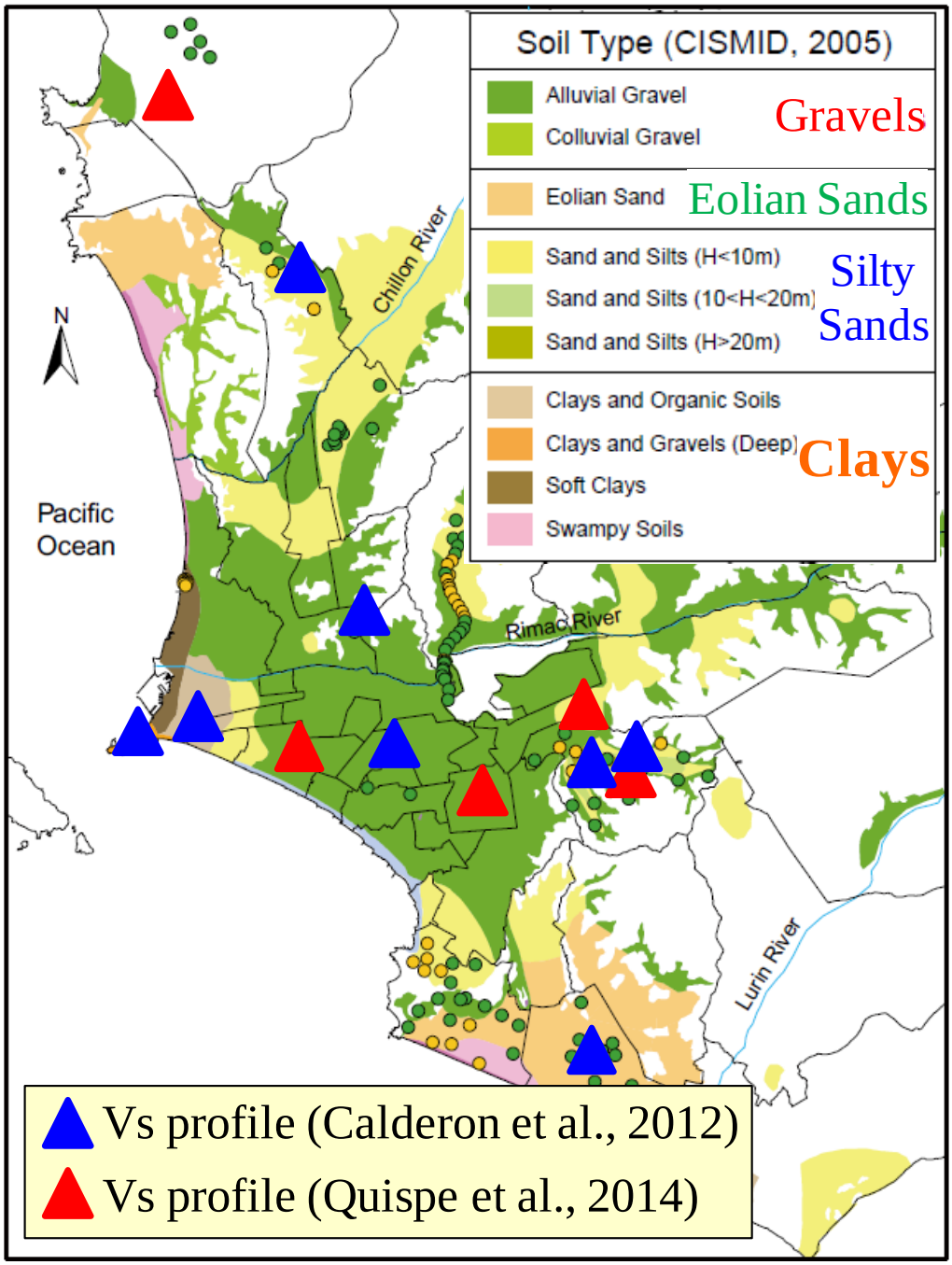

Figure 21. Location of the S-wave velocity profiles determined by Calderon et al. (2012) (blue triangles) and Quispe et al. (2014) (red triangles) on the soil distribution map of Lima (CISMID, 2005).

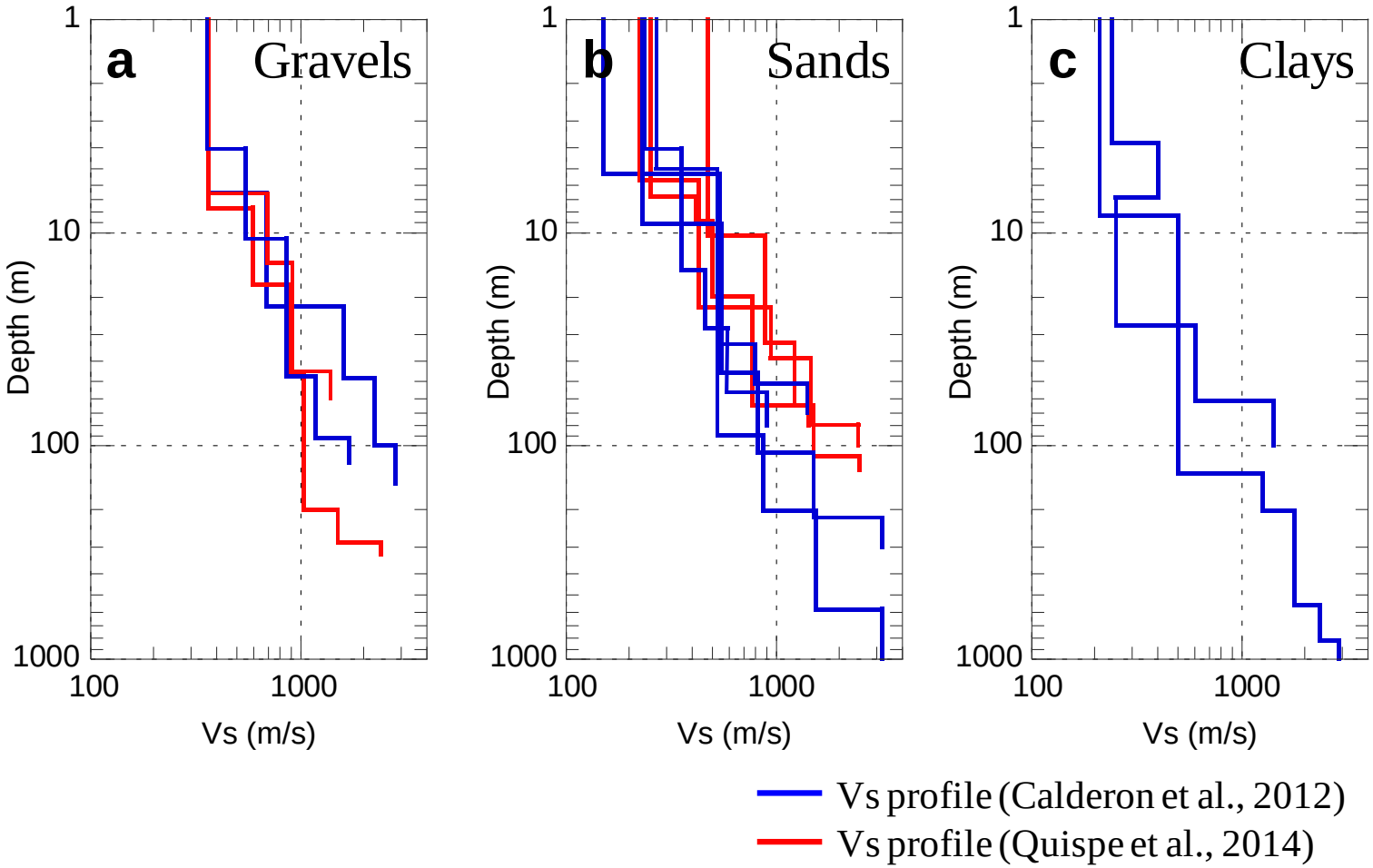

Figure 22. The S-wave velocity profiles estimated by Calderon et al. (2012) (blue lines) and Quispe et al. (2013) (red lines) were gathered and plotted together for the same soil formation (a) gravels, (b) sands, and (c) clays in order to define the S-wave velocity ranges for the different soil formations over Lima Metropolitan Area.

2.3 Estimation of Vs Structure at one Rock Site

One of the objectives in this work is the assessment of observed site amplification using ground motion data. A reference site or usually a rock site is the first rational practice to estimate site response (Satoh et al., 1995a).

A geophysical exploration using Multichannel Analysis of Surface Waves (MASW) method introduced by Park et al. (1999a) was performed at the rock site coded LMO to define the Vs structure; no dynamic information was previously available for this station. Figure 23 (a) shows the location of the station which is installed on outcropping hard rock, while Fig. 23 (b) displays where the geophysical test was conducted.

Microtremor array exploration was not conducted at the LMO rock site as it was done at the stations installed on sedimentary layers (PUCP, CER, MAY, RIN, and ANC sites), because this technique requires a suitable open space for the distribution of the sensors. Figure 23 (b) shows the open space was limited at LMO site. Nonetheless, the MASW technique is a low cost technology, and does not require a great open space when it comes to exploring the near-surface S-wave velocity structure such as the LMO rock site.

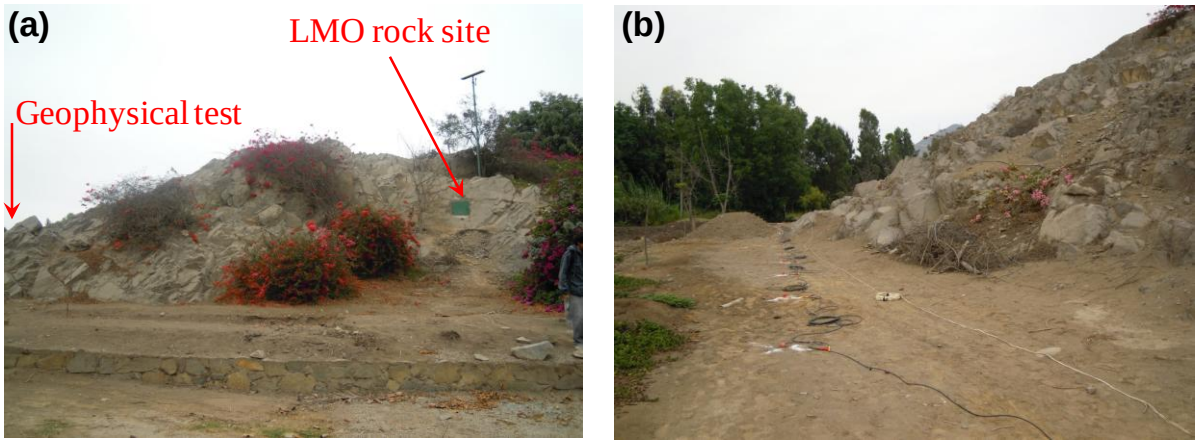

Figure 23. (a) A view of the rock site coded LMO, and (b) Location of MASW line test.

2.3.1 Array Configuration

Linear array configuration was applied for the exploration. Figure 24 illustrates a schematic layout in the installation. Twelve 4.5 Hz geophones were place on the ground surface, connected to a seismograph. The separation distance between them was 3 m. The source used was a 25 lb hammer to generate mainly Rayleigh wave vibrations in the ground. Figure 24 shows several shots of the hammer were performed at both extremes of the array. The seismic waves were gathered by an ES-3000 12 channel Geometrics seismograph and recorded on a computer. Figure 25 (a) and (b) display the time-domain shot gathers for the shot distance of 0.0 m (1st shot in Fig. 24) and 53 m (4th shot in Fig. 24), respectively.

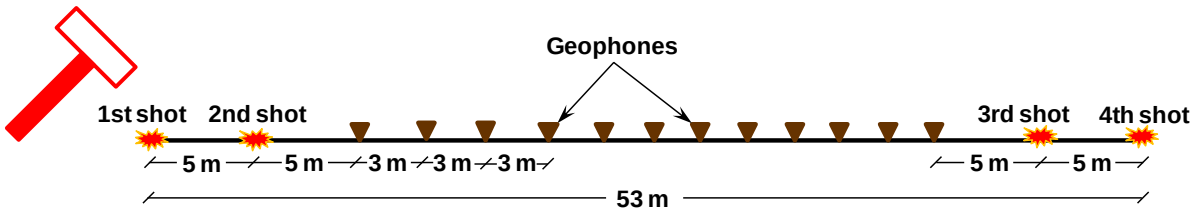

Figure 24. Sketch of survey design at LMO rock site.

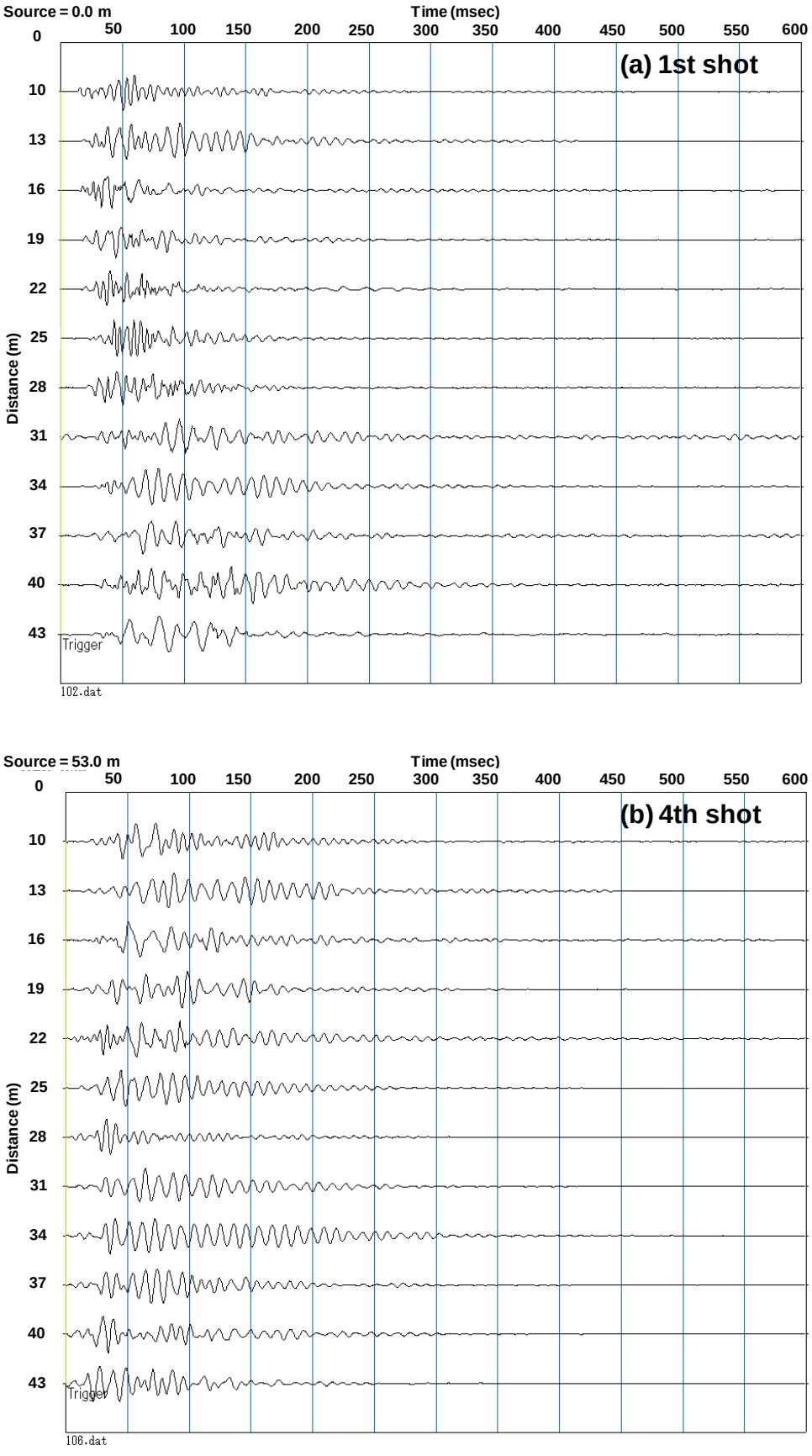

Figure 25. Time-domain shot gather for the shot distance of (a) 0.0 m and (b) 53.0 m.

2.3.2 Estimation of Phase Velocity Dispersion Curve

The Multichannel Analysis of Surface Waves (MASW) technique was applied in this study to determine the observed dispersion curve of Rayleigh waves from the field data. The raw data of the shot gathers is firstly transformed into the frequency-domain, and then phase velocity is calculated using phase shift secondary. The dispersion curve is defined by picking peaks from the phase-velocity image in the frequency domain (Park et al., 1999a).

Figures 26 (a) and (b) display images of dispersion curves obtained at LMO rock site for first and forth shots, respectively. Information from the second and third shots was not used in the analysis since they were very noise.

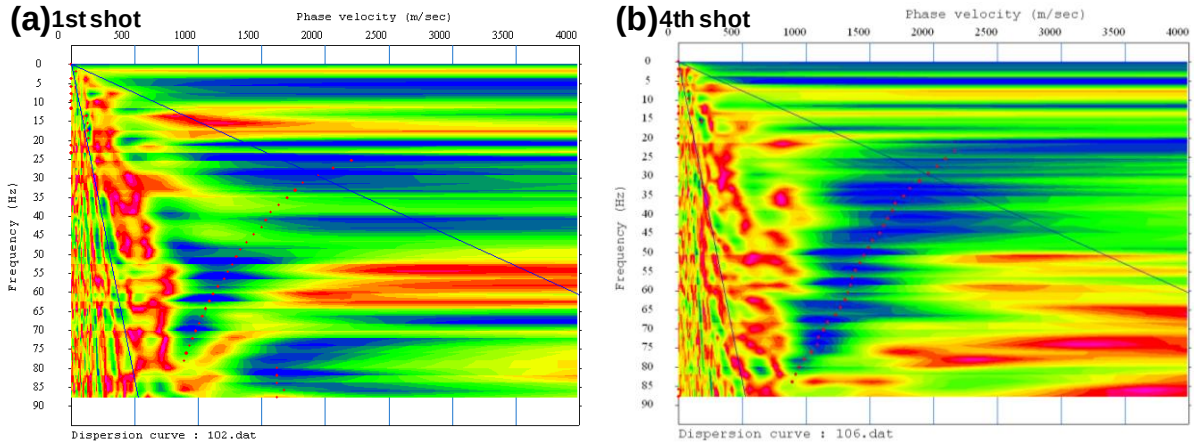

Figure 26. Images of dispersion curves obtained at LMO rock site for (a) first shot, and (b) forth shot.

2.3.3 Estimation of Vs profile

The MASW technique extracts the observed dispersion curve from field data, and this is subsequently inverted (using a traditional non-liner least square method) to define the S-wave velocity structure. The inversion process starts from a preliminary estimate of the Vs profile. The initial model for the inversion is defined using a simple inversion formula, in which the shear wave velocity is taken as a percentage (close to

110%) of phase velocity and assigned to a depth of 1/3 – 1/2 of the wavelength. The initial model is then adjusted to reduce the difference between the observed and the corresponding numerical dispersion curves. The fitting process is performed manually by trial and error (i.e. iteratively by changing the shear wave velocities from top to deeper layers). The inversion analysis in this study considered only the dispersion curve associated with the fundamental mode. Further details of the inversion technique can be found in the literature (e.g. Lin et al., 2004; Hayashi, 2008).

Figure 27 shows how the inverted phase velocities (black line) can explain well the observed dispersion curve (red line with open points). Results from first and forth shots are shown in this figure. Fig. 28 displays the corresponding Vs models obtained from inversion. Grey lines represent the profile for each shot, while black solid line represents the average S-wave velocity structure below the linear array. Information from top layers with a depth less than 5 m was not reliable. In order to overcome this difficulty, a geologist was consulted and the shallow soil structure was defined as shown in Fig. 28. Table 5 also gives pertinent information on the 1-D S-wave velocity structure. The profile estimated at the station installed on outcropping hard rock coded LMO reached a depth of ~30 m. S-wave velocity of the rock increases gradually with depth from ~1000 to ~2200 m/s, as shown in Fig. 28.

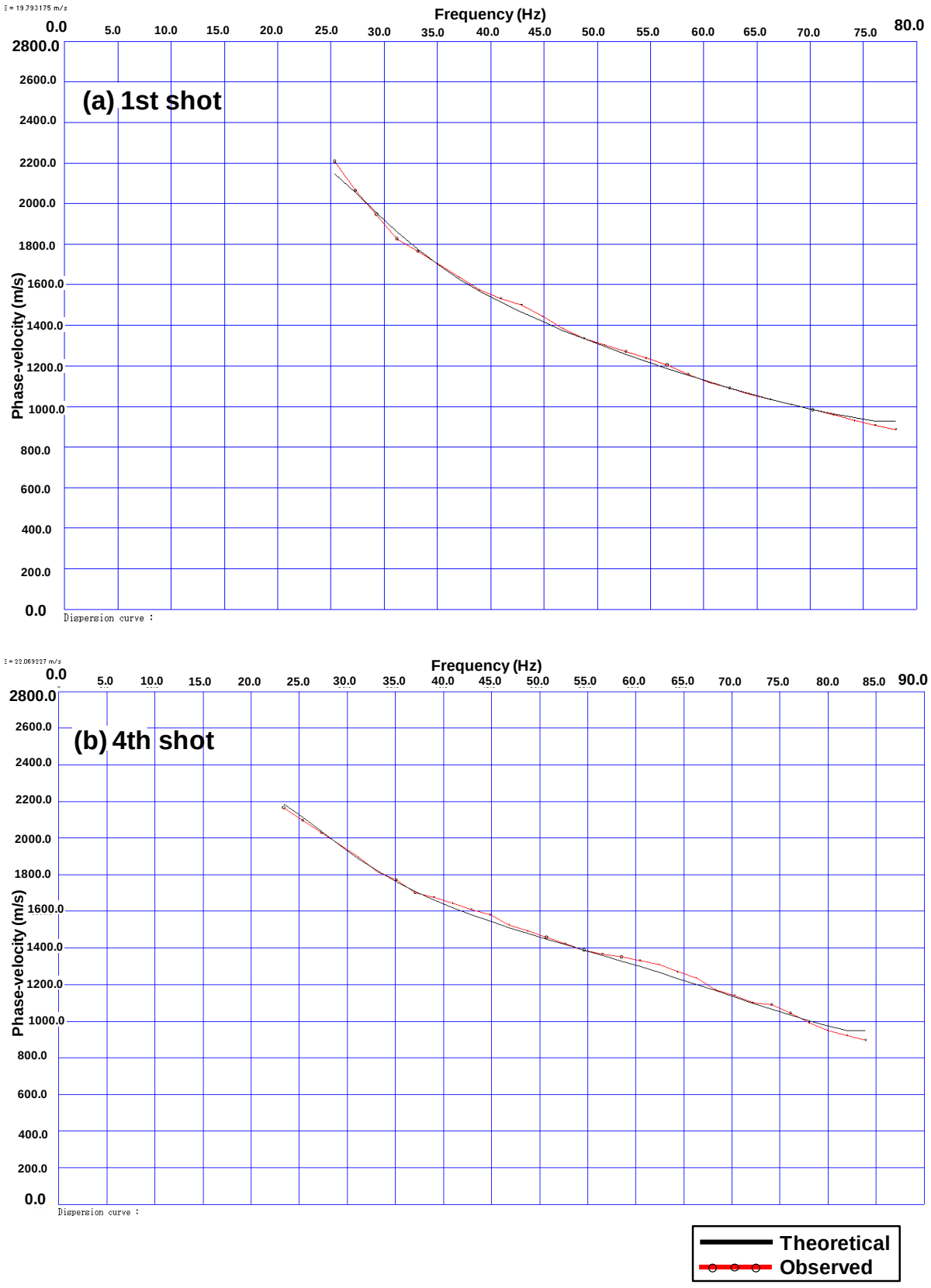

Figure 27. Comparison between the calculated dispersion curve (black line) with the observed ones (red line with open points) for (a) first shot, and (b) forth shot.

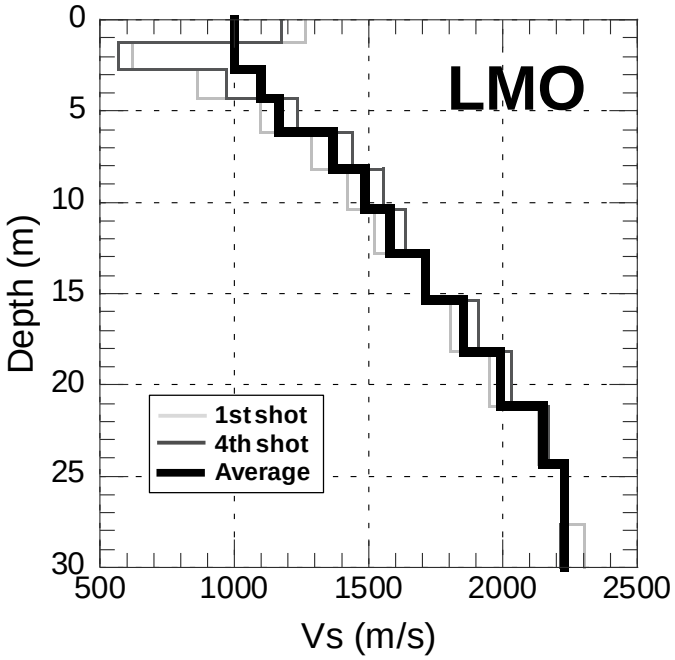

Figure 28. S-wave velocity model at the station installed on outcropping hard rock coded LMO. Grey lines indicate the inverted 1-D Vs profile, while black line represents the average S-wave velocity structure below the linear array conducted at the LMO station.

Table 5. Estimated S-wave velocity structure at LMO rock site.

LMO	
Vs (m/s)	**Thickness (m)**
1000	2.7
1100	1.6
1165	1.8
1366	2.0
1488	2.2
1578	2.4
1713	2.6
1855	2.8
1991	3.0
2152	3.2
2230	-

CHAPTER 3

EVALUATION OF LOCAL SITE AMPLIFICATION USING EARTHQUAKE RECORDS

3.1 Earthquake Observation Network

The strong motion network at Lima Metropolitan Area has been expanded continuously during the past decade (Calderon et al., 2012); being currently operated by two institutions: the Geophysical Institute of Peru (IGP) and the Japan-Peru Center for Earthquake Engineering Research, and Disaster Mitigation (CISMID), as mentioned before in the section 1.4.7. Figure 29 shows the location of the nineteen recording sites used in the present thesis. Stations indicated by solid squares are additional ones used in the present work, while those indicated by solid circles are the same as those used previously by Quispe et al. (2013). Site response of 14 new sites is been analyzed in this work, a part of the 05 stations previously analyzed by Quispe et al. (2013). Figure 29 shows all the stations are located on Quaternary deposits, less the LMO site located on intrusive rock. This rock station served as a reference site to estimate site amplification effects in the present work. Table 6 gives pertinent information on the earthquake stations related to each station's name, location, observation institution, geographical coordinates, and geology. In addition, average shear-wave velocities for the first 30 m (AVs30) and 10 m (AVs10) are also displayed in Table 6, since S-wave velocity (Vs) structures are known for most of the stations. Calderon et al. (2012) and Quispe et al. (2014) conducted microtremor explorations around a number of recording stations maintained by CISMID and IGP, respectively, in order to estimate the shear wave velocity profiles.

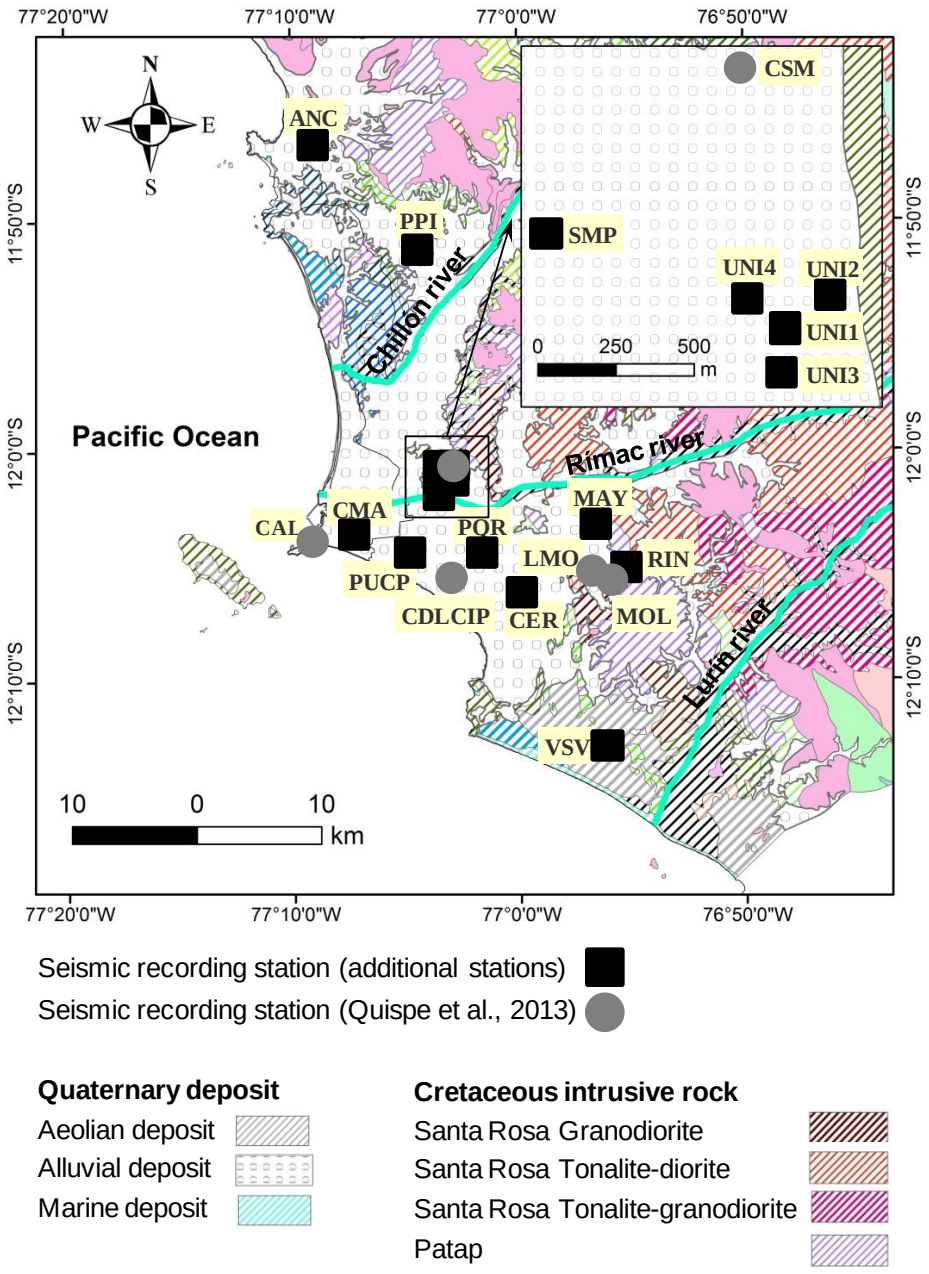

Figure 29. Geological map of Lima (Martínez et al., 1975) with location of earthquake stations. Solid squares represent new stations included in this study, while solid circles represent stations previously analyzed by Quispe et al. (2013).

Table 6. List of earthquake stations.

Station ID	Location		Institution	Latitude	Longitude	Geology	AVs30	AVs10
	District	Province		(deg)	(deg)		(m/s)	(m/s)
CSM	Rímac	Lima	CISMID	-12.013	-77.050	Quaternary Alluvial	659.8	436.5
CAL	Callao	Callao	CISMID	-12.066	-77.156	Quaternary Alluvial	275.1	278.5
MOL	La Molina	Lima	CISMID	-12.089	-76.930	Quaternary Alluvial	N/A	N/A
CDLCIP	San Isidro	Lima	CISMID	-12.092	-77.049	Quaternary Alluvial	565.8	391.0
LMO	La Molina	Lima	IGP	-12.085	-76.948	Santa Rosa Granodiorite	1598.4	1183.0
ANC	Ancón	Lima	IGP	-11.777	-77.150	Quaternary Alluvial	414.6	282.8
PUCP	San Miguel	Lima	IGP	-12.074	-77.080	Quaternary Alluvial	577.9	397.9
RIN	La Molina	Lima	IGP	-12.087	-76.923	Quaternary Alluvial	447.8	294.3
CER	San Borja	Lima	IGP	-12.103	-76.998	Quaternary Alluvial	647.8	434.3
MAY	Ate	Lima	IGP	-12.055	76.944	Quaternary Alluvial	681.6	474.0
UNI1	Rímac	Lima	CISMID	-12.021	-77.049	Quaternary Alluvial	N/A	N/A
UNI2	Rímac	Lima	CISMID	-12.020	-77.048	Quaternary Alluvial	N/A	N/A
UNI3	Rímac	Lima	CISMID	-12.022	-77.049	Quaternary Alluvial	N/A	N/A
UNI4	Rímac	Lima	CISMID	-12.020	-77.050	Quaternary Alluvial	N/A	N/A
VSV	Villa El Salvador	Lima	CISMID	-12.213	-76.938	Quaternary Marine	453.9	355.3
PQR	Lima	Lima	CISMID	-12.073	-77.032	Quaternary Alluvial	653.1	452.9
SMP	San Martín de Porres	Lima	CISMID	-12.018	-77.056	Quaternary Alluvial	N/A	N/A
PPI	Puente Piedra	Lima	CISMID	-11.852	-77.074	Quaternary Alluvial	370.3	228.1
CMA	Bellavista	Callao	CISMID	-12.060	-77.123	Quaternary Alluvial	324.1	238.6

3.2 Ground Motion Records

Hundreds of events have been recorded by the strong motion network in the last ten years. In this study, the author analyzed 55 moderate earthquakes observed at the 19 seismic recording stations from 2003 to 2013, including the same events as those analyzed by Quispe et al. (2013). Figure 30 shows the epicenters of the analyzed events. Dark red circles indicate new events, while light red circles indicate events previously used by Quispe et al. (2013). A total of 232 ground motion records were processed in this study. Figure 31 shows the hypocentral distribution of them with depths represented by black points. The grey points indicate the records used by Quispe et al. (2013), also analyzed in the present work. 201 seismic records more have been included in the analysis. The data set used (black points) shows a better coverage over hypocentral distance than those analyzed by Quispe et al. (2013) (grey points), as displayed in Fig. 31. The additional new events as well as the events previously analyzed by Quispe et al. are shallow and intermediate earthquakes (depth < 140 km). The hypocentral distribution of them is in the range between 40 km and 200 km. Figure 32 plots Local Magnitude (ML) versus average Peak Ground Acceleration (PGA). Solid points indicate the seismic records processed in this study, while open points mean the records previously analyzed by Quispe et al. (2013). The Local Magnitude of them ranges from 3.0 to 6.0. Most of the records used have a PGA less than 80 gals, including the records used by Quispe et al. (2013). Since the PGAs in the records used were less than 160 cm/sec^2, a nonlinear behavior of soil was not assumed in this study. Table 7 presents the earthquake parameters determined by the Geophysical Institute of Peru (IGP).

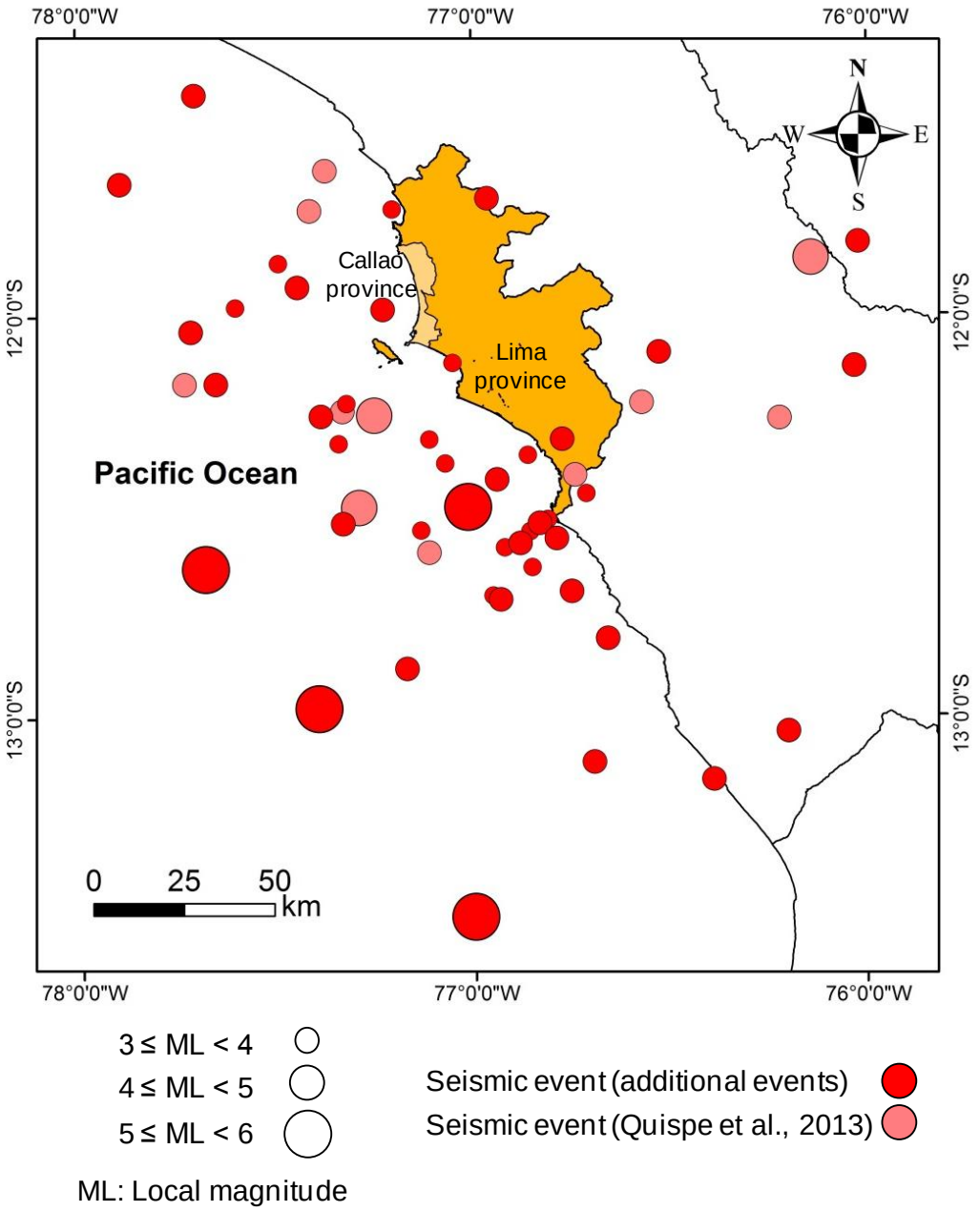

Figure 30. Lima Metropolitan Area with epicenter of seismic events. Dark red circles mean the epicenter of new events, while light red colors represent the earthquakes analyzed by Quispe et al. (2013).

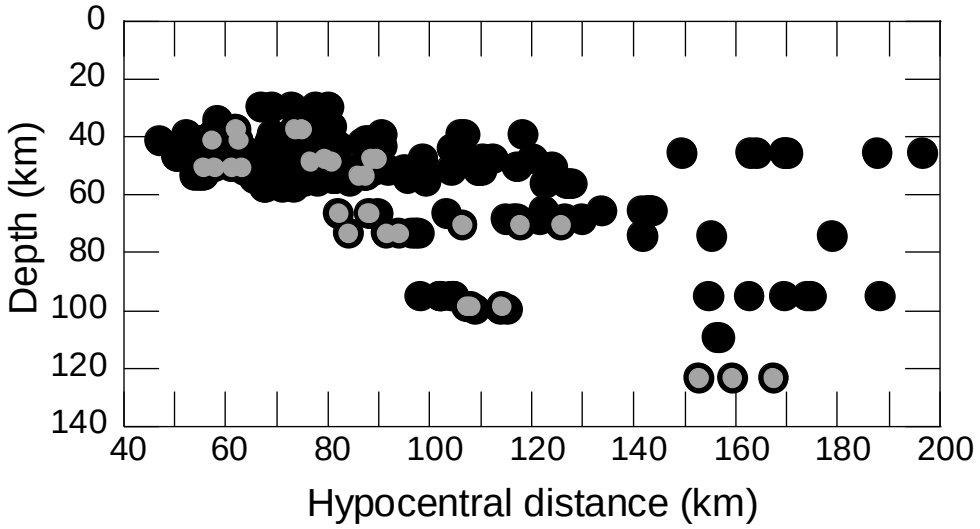

Figure 31. Distribution of hypocentral distance and depth. The present work has analyzed 232 seismic records represented by black points. Grey points represent the records previously analyzed by Quispe et al. (2013), also included in this study.

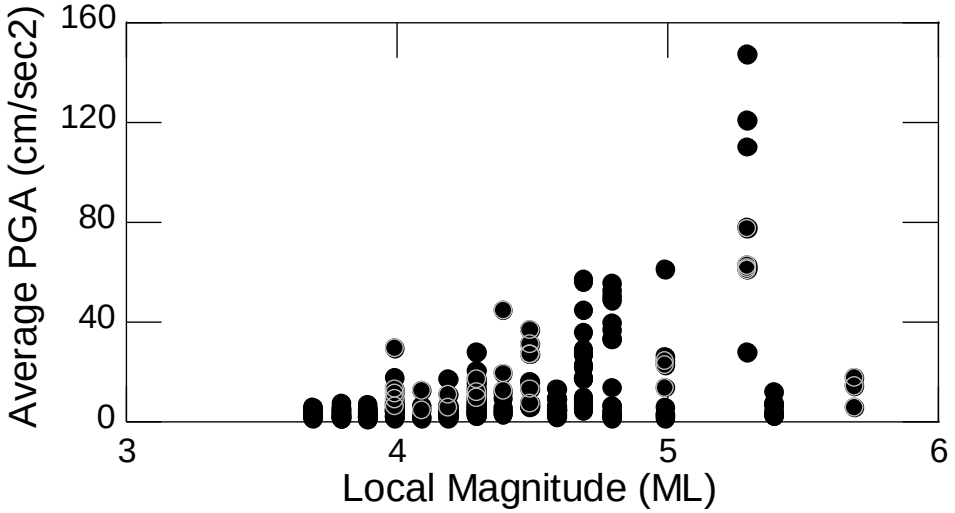

Figure 32. Distribution of average PGA versus Local Magnitude (ML). Solid points represent seismic records processed in this study, including the records previously analyzed by Quispe et al. (2013) represented by open points.

Table 7. Event information.

Date	Hour	Long.	Lat.	Mag.	Depth	Earthquake stations																		
yyyy/mm/dd	hr:min	(deg)	(deg)	(ML)	(km)	CSM	CAL	MOL	CDLCIP	LMO	ANC	PUCP	RIN	CER	MAY	UNI1	UNI2	UNI3	UNI4	VSV	PQR	SMP	PPI	CMA
2003/05/08	16:33	-77.395	-12.980	5.4	51	*						*												
2003/05/28	21:26	-77.013	-12.479	5.3	51	*						*												
2005/03/02	13:48	-76.140	-11.860	5.7	124	*	*	*																
2005/07/19	13:45	-77.110	-12.590	4.1	49	*		*																
2005/07/25	06:51	-77.330	-12.240	4.0	42	*		*			*													
2005/10/14	05:01	-76.740	-12.400	4.4	74	*	*	*																
2005/11/10	16:38	-76.220	-12.260	4.0	71	*	*	*																
2005/12/27	17:02	-76.570	-12.220	4.5	99	*		*																
2006/05/26	01:57	-77.410	-11.740	4.5	38	*		*		*														
2006/12/11	21:53	-77.370	-11.640	4.2	54			*		*			*											
2008/03/29	06:40	-77.730	-12.170	4.3	48	*	*		*						*									
2008/03/29	12:51	-77.250	-12.250	5.3	51	*	*		*	*	*		*		*									
2008/06/07	13:06	-77.290	-12.480	5.0	67	*	*			*	*				*									
2011/10/02	16:33	-76.880	-12.570	4.0	74	*											*							*
2011/11/20	03:00	-77.490	-11.870	3.9	56											*	*		*					
2011/12/19	05:37	-77.385	-12.252	4.7	44	*							*			*	*	*	*		*		*	
2011/12/26	20:29	-76.659	-12.807	4.4	52	*											*	*	*	*	*			
2011/12/29	13:45	-76.788	-12.558	4.6	52	*										*	*	*		*	*		*	*
2012/01/23	02:31	-77.713	-12.040	4.4	37	*																*		
2012/02/11	04:27	-76.695	-13.116	4.8	66	*							*			*	*	*		*		*		*
2012/02/14	04:42	-76.938	-12.411	4.8	42	*										*	*	*	*	*	*	*	*	*
2012/02/19	02:19	-77.225	-11.987	4.0	47	*							*				*	*	*		*	*		
2012/02/29	08:50	-76.750	-12.690	4.3	40	*							*							*				
2012/03/07	03:52	-77.110	-12.310	3.7	49						*									*	*	*	*	
2012/03/11	08:20	-77.132	-12.537	3.8	52															*	*		*	
2012/03/19	23:21	-77.442	-11.931	4.0	45						*		*			*	*	*	*					
2012/03/25	23:00	-77.680	-12.630	5.0	48					*	*		*			*	*	*				*		
2012/05/17	03:45	-76.526	-12.095	4.2	100	*							*					*			*			

The data surrounded with dense lines are those analyzed by Quispe et al. (2013)

Source parameters were determined by the Geophysical Institute of Peru (IGP)

(* means that the event was recorded)

Table 7 (*continued*)

Date	Hour	Long.	Lat.	Mag.	Depth	Earthquake stations																		
yyyy/mm/dd	hr:min	(deg)	(deg)	(ML)	(km)	CSM	CAL	MOL	CDLCIP	LMO	ANC	PUCP	RIN	CER	MAY	UNI1	UNI2	UNI3	UNI4	VSV	PQR	SMP	PPI	CMA
2012/06/21	22:17	-76.960	-11.710	4.7	96	*				*	*		*					*			*	*		*
2012/06/27	12:41	-76.200	-13.040	4.2	96								*					*		*	*	*	*	
2012/06/28	11:18	-77.650	-12.170	4.2	44					*	*		*		*			*			*	*		*
2012/07/04	16:01	-77.050	-12.120	3.8	54						*		*								*	*		
2012/07/16	17:21	-76.860	-12.350	3.8	40										*	*		*				*		
2012/08/01	13:02	-77.340	-12.320	3.7	46					*	*		*		*			*			*	*	*	
2012/08/07	10:30	-77.000	-13.500	5.4	46						*		*				*	*		*	*	*	*	
2012/08/11	09:35	-77.700	-11.450	4.3	69								*		*		*	*			*	*		*
2012/09/15	11:27	-77.330	-12.520	4.0	47								*	*	*		*	*		*	*	*		
2012/09/25	06:50	-77.320	-12.220	3.9	42								*	*	*		*	*			*	*		
2012/10/14	16:50	-77.600	-11.980	3.7	30					*			*	*			*	*			*			
2012/10/30	07:48	-76.855	-12.540	3.9	52								*	*			*	*		*	*	*	*	
2012/10/30	13:35	-76.920	-12.580	3.9	56								*				*			*			*	
2012/10/30	19:44	-76.830	-12.520	4.3	55					*			*	*	*		*	*		*	*	*	*	
2012/11/01	01:37	-76.020	-11.820	4.5	57												*	*		*	*	*		
2012/11/04	01:52	-76.030	-12.130	4.7	110												*	*				*		
2012/11/05	08:08	-76.810	-12.510	3.9	50												*	*			*			
2012/11/10	06:57	-76.712	-12.446	3.9	45												*			*		*	*	
2013/01/10	05:14	-77.890	-11.670	4.2	40											*		*	*					
2013/01/15	19:01	-77.070	-12.370	3.9	48											*		*	*	*	*	*		
2013/03/01	02:56	-76.950	-12.700	3.9	43											*				*				
2013/03/02	02:51	-76.930	-12.710	4.1	42											*				*		*		
2013/03/05	04:24	-76.850	-12.630	3.8	35											*		*		*				
2013/03/11	14:33	-77.170	-12.881	4.2	45										*	*				*				
2013/03/19	23:06	-76.390	-13.160	4.6	75										*					*			*	
2013/04/12	13:53	-77.201	-11.736	3.8	58										*			*			*	*		
2013/05/10	03:35	-76.772	-12.311	4.3	52													*		*	*			

Source parameters were determined by the Geophysical Institute of Peru (IGP)

(* means that the event was recorded)

3.3 Data Processing

The procedure for calculating S-wave spectra was the same as followed by Quispe et al. (2013). The illustration for the procedure is shown in Fig. 33. First, S-wave portion of two horizontal components, EW and NS, was selected, beginning at initial shear-wave arrival (Fig. 33a). For recognizing an onset time of S-wave, Husid plots (Husid, L. R., 1969) were used, where horizontal axis is the time and vertical axis is the accumulated horizontal component square for each horizontal component, as shown in Fig. 33b. The end moment of S-wave was picked up by using cumulative Root Mean Square (RMS) function (McCann and Shah, 1979). In this study, the time at which the S-wave window ended was defined as the point on the time axis at which cumulative RMS starts to decrease, as illustrated in Fig. 33c. The end moment of S-wave was estimated visually.

After the onset and end times of S-wave were determined, the S-wave portion was cosine-tapered 10 percent at each end of the time window, using the same criterion as that used by Takemura et al. (1991). Fig. 33a shows the tapered function represented by a solid line. The horizontal spectrum was then calculated, using the Fast Fourier Transform as shown in Fig. 33d. Spectral amplitudes were smoothed with a 1.2 Hz-width Parzen window. Next, S-wave Fourier amplitude spectra of the two horizontal components were summed vectorially for being used in the analysis.

Most of the analyzed seismic events were small with a length of S-waves from 2 to 4 s, offering a low resolution for frequencies lower than 1 Hz, as shown in the S-wave Fourier amplitude spectrum of Fig. 33d. Therefore, site, path, and source effects were evaluated in the frequency range from 1 to 20 Hz in the present work.

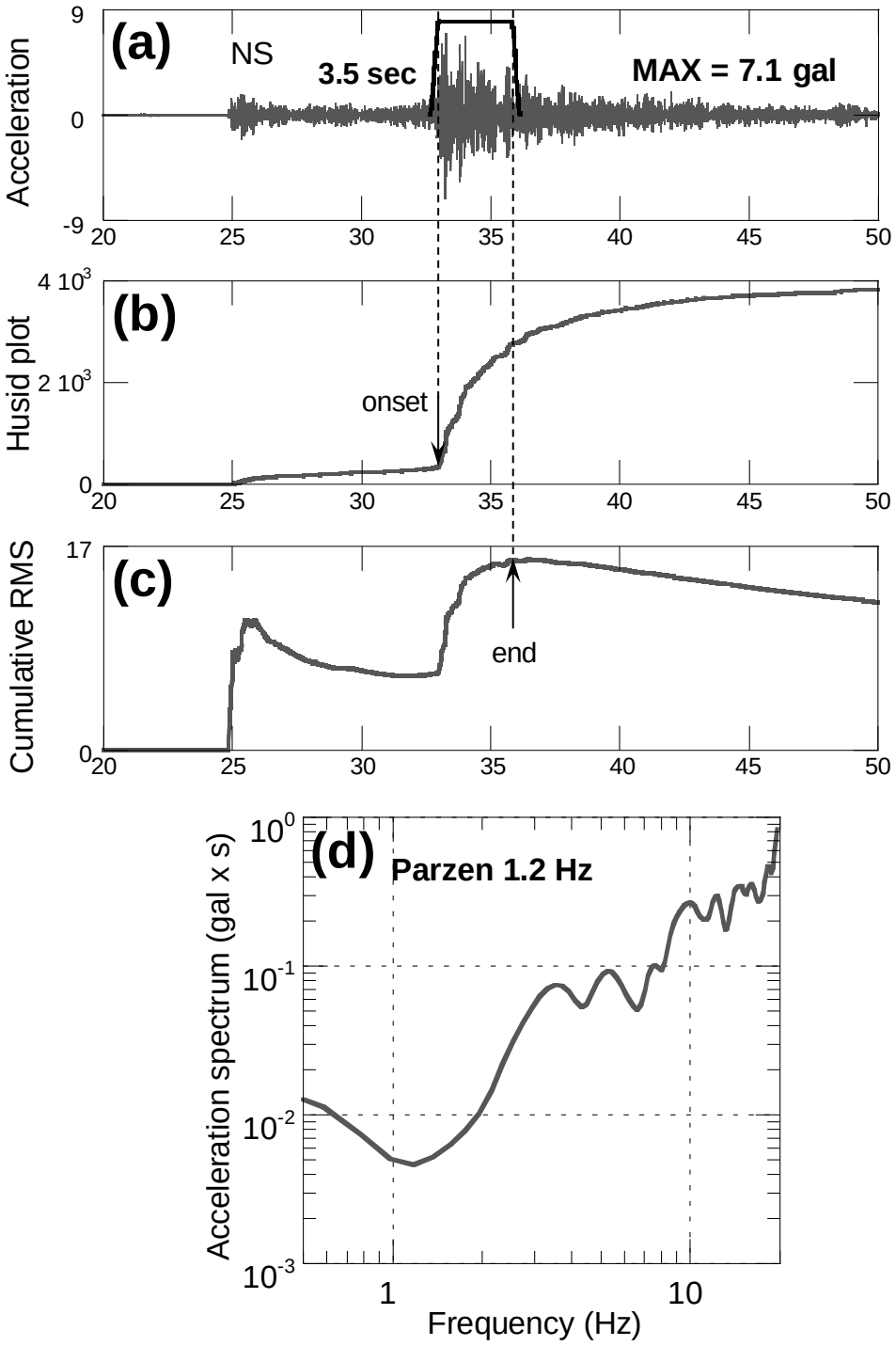

Figure 33. Procedure for extracting S-wave portion. (a) NS horizontal component recorded at CSM station during the event 2012/01/23 02:31 (ML 4.4) is shown as an example. (b) Husid plot is used for recognizing the onset time of S-waves. (c) End moment of S-waves is estimated using the cumulative root mean square (RMS) function. (d) The Fourier Amplitude Spectrum is calculated after obtaining the S-wave portion.

3.4 Spectral Inversion Method

3.4.1 Methodology

The earthquake records were analyzed by the Spectral Inversion Method (SIM) (Iwata and Irikura, 1988), in order to estimate effects of site response, path and source spectra. From a practical point of view, this technique offers the advantage that records from some events can be included in the inversion even if these events are not recorded at all sites. This offers the advantage of a more complete exploitation of the data set (Riepl et al., 1998).

The observed S-wave Fourier amplitude spectra of the i^{th} event recorded at the j^{th} site $O_{ij}(f)$ can be written in the frequency domain as a linear multiplication of a site-effect term $G_j(f)$, a path term $P_{ij}(f, R)$, and a source term $S_i(f)$:

$$O_{ij}(f) = G_j(f) \cdot P_{ij}(f, R) \cdot S_i(f) \tag{4}$$

The path effect includes two factors in the case of point source assumption: one is the geometrical spreading which can be expressed by means of R_{ij}^{-1}, and the other is the inelastic losses. The path effect term $P_{ij}(f, R)$ can be represented as follows:

$$P_{ij}(f) = R_{ij}^{-1} \cdot exp\left(-\pi R_{ij} f / Qs(f) Vs\right) \tag{5}$$

where R_{ij} is the hypocentral distance between the i^{th} event and the j^{th} station, $Qs(f)$ and Vs are S-wave frequency dependent quality factor and velocity along the wave propagation path, respectively. Note that Vs equal to 3.5 km/sec were assumed in this study. As a result, $O_{ij}(f)$ would be represented as:

$$O_{ij}(f) = G_j(f) \cdot R_{ij}^{-1} \cdot exp\left(-\pi R_{ij} f / Qs(f) Vs\right) \cdot S_i(f) \tag{6}$$

Performing a logarithmic operation to Eq. (6), the following equation is obtained:

$$lnO_{ij}(f) = lnS_i(f) + lnG_j(f) - \left(\pi f R_{ij}/Vs\right) \cdot Q(f) - lnR_{ij} \quad (7)$$

The Eq. (7) is also represented as a compact matrix formulation in the following manner:

$$[Y] = \left[A\left(\frac{Source}{1 \ldots i, I}\middle|\frac{Site}{1 \ldots j, J}\middle|Path\right)\right][X] \quad (8)$$

$$\begin{bmatrix} log_{10}O_{11}(f) \\ \vdots \\ log_{10}O_{ij}(f) \\ \vdots \\ \dfrac{log_{10}O_{ij}(f)}{log_{10}G_r(f)} \end{bmatrix} = \left[\begin{array}{cccc|cccc|c} 1 & 0 & 0 & 0 & 1 & 0 & 0 & 0 & R_{11} \\ \vdots & \vdots & \vdots & \vdots & \vdots & \vdots & \vdots & \vdots & \vdots \\ 0 & 0 & 1 & 0 & 0 & 0 & 1 & 0 & R_{ij} \\ \vdots & \vdots & \vdots & \vdots & \vdots & \vdots & \vdots & \vdots & \vdots \\ 0 & 0 & 0 & 1 & 0 & 0 & 0 & 1 & R_{IJ} \\ 0 & 0 & 0 & 0 & 1 & 0 & 0 & 0 & 0 \end{array}\right] \begin{bmatrix} log_{10}S_1(f) \\ \vdots \\ log_{10}S_I(f) \\ log_{10}G_1(f) \\ \vdots \\ \dfrac{log_{10}G_J(f)}{Q} \end{bmatrix}$$

N + 1 N + 1 X I + J + 1 I + J + 1

The Eq. (8) is solved using the singular value decomposition method (Lawson and Hanson, 1974). *N* corresponds to the number of earthquakes *I* recorded at the total number of stations *J*. The unknown parameters to be determined for each frequency are *I* (source spectrum) + *J* (site effect) + 1 (Qs-value) from $I \times J$ data, that means an unconstrained degree of freedom exists in the equation. In order to solve the undetermined degree of freedom in the Eq. (8), a constraint condition should be given by choosing at least one reference site or event. This study used a reference site. Many authors (Takemura et al., 1991; Yamanaka et al., 1998; Yamanaka et al., 2011) used a rock site as a constraint condition by constraining its site response. The site response was computed numerically by one-dimensional vertical multiple reflection of S waves, as well as geological and geotechnical information was consulted since rock sites suffer from local site effects. It is important to mention the three effects – source, path and site – are automatically separated after applying the above-mentioned procedure.

3.4.2 Constraint Condition

As discussed above, a constraint condition is needed to remove the undetermined degree of freedom in the inversion process. In this work, a geophysical exploration at the rock site coded LMO was conducted to estimate the S-wave velocity structure at this site, as previously explained in Chapter 2. The estimated Vs profile reached a depth of 30 m, where the bottom had a S-wave velocity of ~2200 m/s, as shown in Fig. 34 (a). This picture was previously shown in Fig. 28. Figure 34 (b) displays the site response of LMO calculated numerically, estimated from the profile. The quality factor Qs for each layer was computed with the assumption $Qs = Vs/10$. Slight amplification is observed at frequencies higher than 9 Hz. The theoretical site amplification of LMO was the constraint condition in the present work, the free surface effects were considered.

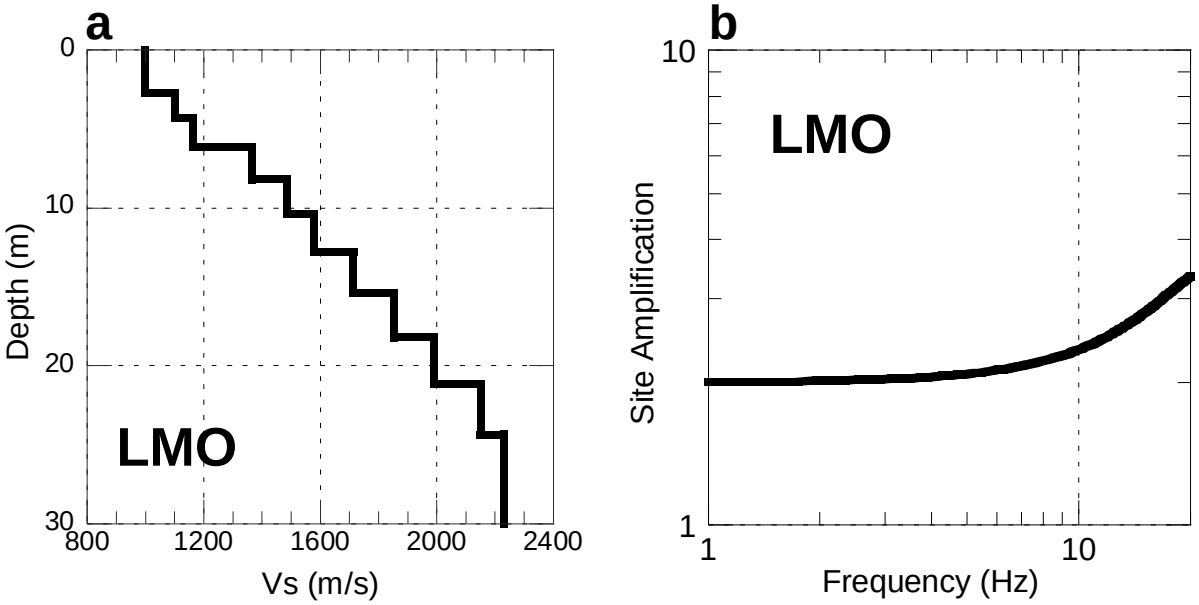

Figure 34. Seismic information at LMO station. (a) S-wave velocity profile. (b) 1-D amplification of SH waves.

3.4.3 Qs-values for propagation path

S-wave quality factor, source spectra and site response were simultaneously obtained applying the inversion technique to the selected database. The estimated S-wave quality factor (Qs-values) denoted by points is shown in Fig. 35. The black solid line in the figure is a regression line for $Qs(f) = 95.6f^{0.66}$ in this study, while the grey line represents the quality factor estimated by Quispe et al. (2013). This study included new additional data, overcoming the limitation of data reported by Quispe et al. (2013). The data set used shows better coverage over hypocentral distance than those used by Quispe et al. (2013) (Fig. 31), indicating Qs-values are more stable than those obtained by Quispe et al. (2013). The seismic records used in their study only covered a limited hypocentral distance interval, as illustrated in Fig. 31. Figure 35 also shows the estimated Qs factor is slightly larger than the results previously obtained by Quispe et al. (2013). One possibility might be related to the analysis of new stations with much better spatial distribution (Fig. 29), as well as the inclusion of more records from shallow and deep earthquakes as shown in Fig. 31.

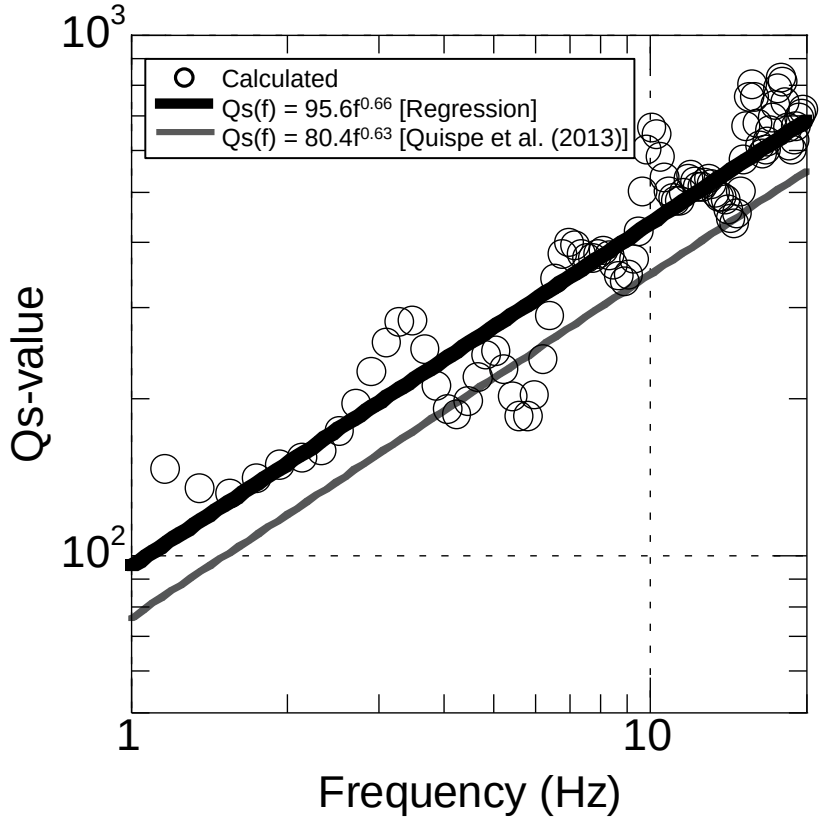

Figure 35. Qs-values determined by the inversion as a function of frequency. The black solid line represents the best-fit relation between Qs-values and frequency for the present work. The grey solid line indicates the result estimated by Quispe et al. (2013).

3.4.4 Source Effects

Source acceleration amplitude spectra $S_i(f)$ of the 55 events were obtained from the inversion analysis, and the seismic moment density function $M_i(f)$ for each event was calculated applying this equation $S_i(f) = R_{\theta\phi} M_i(f)/4\pi\rho v_S^3$ – which was also used in these studies (Brune, J. N., 1970; Kanamori, H., 1972; Takemura, et al., 1990). In the equation, $R_{\theta\phi}$ is the radiation pattern coefficient, ρ is density, and v_S is the S-wave velocity in the source layer. The author used the same coefficients as previously used in the study of Quispe et al. (2013) for the calculation of $M_i(f)$, $R_{\theta\phi} = 0.6$, $\rho = 3.0\ g/cm^3$, and $v_S = 4.0\,km/s$. Figure 36 displays three examples of computed $M_i(f)$ with different magnitudes. The amplification level of seismic moment depends

significantly on magnitude as shown in Fig. 36. The Brune's omega-square model (Brune, 1970) represented by solid lines in Fig. 36 was also calculated. The theoretical model can fit well the observed values in the frequency range between 1.0 and 10.0 Hz.

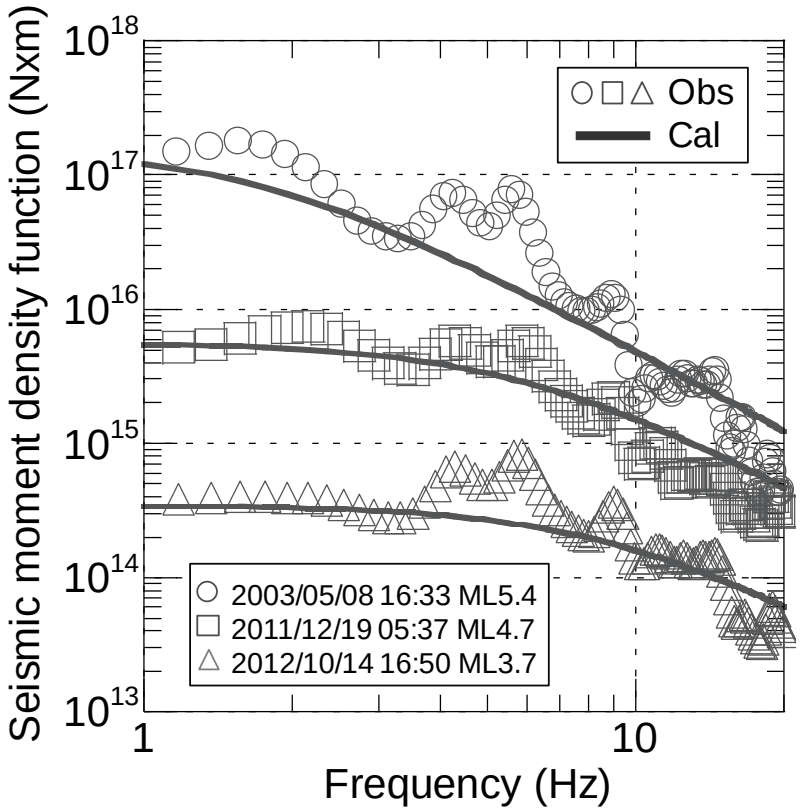

Figure 36. Examples of seismic moment density functions (open circles, squares and triangles) and approximated omega-squared model shown by solid lines.

Seismic moment M_0 and corner frequency f_c for each event were also calculated and plotted as shown in Fig. 37. From the source displacement amplitude spectrum, the corner frequency f_c and flat level of the displacement spectrum Ω_0 were estimated visually (Iwata and Irikura, 1988). The seismic moment M_0 was derived from the flat level of the displacement spectrum based on Brune's model (Brune, 1970). The fitting between M_0 and f_c yields a slope of -3.82, as shown in Fig. 37. The estimated value deviates from the scaling law $M_0 \alpha f_c^{-3}$ (Aki, 1967). The explanation might be in relation to the source depth. The events analyzed in this study have a focal depth larger than 20 km, while in his study (Aki, 1967) shallow events with a focal depth less than

20 km were used. Table 8 shows the estimated seismic moment M_0 and corner frequency f_c for the 55 seismic events used in this study.

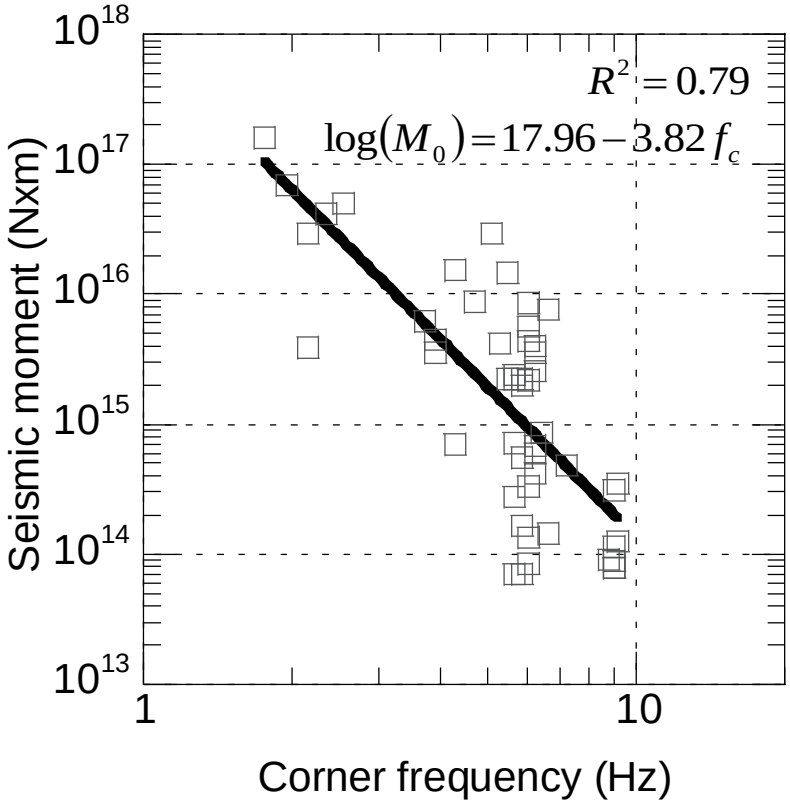

Figure 37. Plot of seismic moment M_0 versus corner frequency f_c. The solid line in the figure is the regression line for M_0 and f_c.

Table 8. Estimated corner frequency f_c and seismic events for the seismic events used in this study.

Seismic event	fc (Hz)	Mo (N.m)
2006/05/26 01:57 ML4.5	5.859	2.247E+15
2008/03/29 12:51 ML5.3	1.953	6.863E+16
2008/06/07 13:06 ML5.0	2.148	2.946E+16
2008/03/29 06:40 ML4.3	4.297	1.541E+16
2005/07/25 06:51 ML4.0	5.469	2.242E+15
2003/05/08 16:33 ML5.4	1.758	1.610E+17
2003/05/28 21:26 ML5.3	2.344	4.120E+16
2011/12/26 20:29 ML4.4	3.906	4.534E+15
2012/02/14 04:42 ML4.8	5.664	2.215E+15
2012/03/07 03:52 ML3.7	5.859	1.671E+14
2012/01/23 02:31 ML4.4	5.664	7.121E+14
2011/12/19 05:37 ML4.7	6.055	5.597E+15
2011/12/29 13:45 ML4.6	5.859	1.986E+15
2012/02/19 02:19 ML4.0	9.180	1.259E+14
2012/10/30 19:44 ML4.3	6.055	2.185E+15
2012/10/30 13:35 ML3.9	5.859	5.495E+14
2012/10/30 07:48 ML3.9	5.664	2.776E+14
2012/10/14 16:50 ML3.7	9.180	3.478E+14
2012/09/25 06:50 ML3.9	5.859	6.974E+13
2012/09/15 11:27 ML4.0	6.250	6.811E+14
2012/08/11 09:35 ML4.3	5.273	4.194E+15
2012/08/07 10:30 ML5.4	2.539	4.984E+16
2012/08/01 13:02 ML3.7	6.055	3.329E+14
2012/07/16 17:21 ML3.8	5.664	7.077E+13
2012/07/04 16:01 ML3.8	8.984	7.873E+13

Table 8 (*continued*)

Seismic event	fc (Hz)	Mo (N.m)
2012/06/27 12:41 ML4.2	4.688	8.882E+15
2012/06/28 11:18 ML4.2	4.297	6.924E+14
2011/10/02 16:33 ML4.0	7.227	4.855E+14
2012/03/25 23:00 ML5.0	6.055	4.384E+15
2012/02/11 04:27 ML4.8	6.250	3.963E+15
2012/06/21 22:17 ML4.7	6.055	8.574E+15
2012/05/17 03:45 ML4.2	6.250	3.563E+15
2012/03/19 23:21 ML4.0	2.148	3.891E+15
2012/03/11 08:20 ML3.8	6.641	1.435E+14
2012/11/01 01:37 ML4.5	5.469	1.477E+16
2012/11/04 01:52 ML4.5	5.078	2.940E+16
2011/11/20 03:00 ML3.9	6.055	1.340E+14
2012/11/05 08:08 ML3.9	6.055	8.501E+13
2012/02/29 08:50 ML3.9	6.250	5.987E+14
2012/11/10 06:57 ML3.9	8.984	8.888E+13
2013/01/10 05:14 ML4.2	6.250	2.553E+15
2013/01/15 19:01 ML3.9	8.984	7.933E+13
2013/03/01 02:56 ML3.9	8.789	9.136E+13
2013/03/02 02:51 ML4.1	6.250	4.180E+14
2013/03/05 04:24 ML3.8	8.984	1.138E+14
2013/03/11 14:33 ML4.2	6.445	8.633E+14
2013/03/19 23:06 ML4.6	6.641	7.710E+15
2013/04/12 13:53 ML3.8	8.984	3.084E+14
2013/05/10 03:35 ML4.3	5.664	2.405E+15

3.4.5 Inverted Site Amplification

Figure 38 displays the results related to the site amplification obtained from the inversion technique in this study, represented by a black solid line. The results previously obtained by Quispe et al. (2013) for CMS, CAL, MOL and CDLCIP sediment sites are also shown in Fig. 38, represented by a grey dash line. Differences are observed between each other. Quispe et al. (2013) reported that their results still have difficulties in the solution because of the limitation in data, as previously explained in section 1.4.6. This study has overcome such limitation, indicating the site response estimated in this study is more stable in the frequency range of interest from 1 to 20 Hz.

The amplification estimated in this study is predominantly caused by the input motion of SH-waves propagating vertically from the bottom layer (Vs ~2200 m/s) of the model for the reference site. The inversion results (black solid lines) were also compared with the theoretical amplification from the 1-D S-wave profiles (grey solid lines). Shallow and deep Vs structure is known for CSM, CAL, ANC, PUCP, MAY, VSV, and CMA stations. They were estimated from microtremor measurements (Calderon et al., 2012; Quispe et al., 2014). The layer with a Vs ~2200 m/s was detected in all these models. The theoretical amplification for these sites was computed from this layer to the ground surface. Figure 38 shows peaks and troughs of the theoretical site amplification can be identified in those of the spectral inversion technique, however the amplification levels differ for some sites. The locations where the microtremor observation was conducted are more than 50 m away from the site where the earthquake stations are installed. This might explain the misfit between the observed and calculated amplification factors.

From the inversion results obtained in this study, we observed that stations such as CSM, MOL, PQR, SMP, UNI1, UNI2, UNI3, and UNI4 mainly display the predominant peaks at frequencies higher than 3 Hz, while some sites such as ANC, RIN, VSV, and PPI show several predominant peaks with large amplification in a wide frequency range. On the contrary, the site responses for CMA and CAL stations display spectral decrease from low to high frequency. The reason why the factors of

the site amplification change in the frequency range is in relation to the subsurface condition. This is going to be explained in details in the following section.

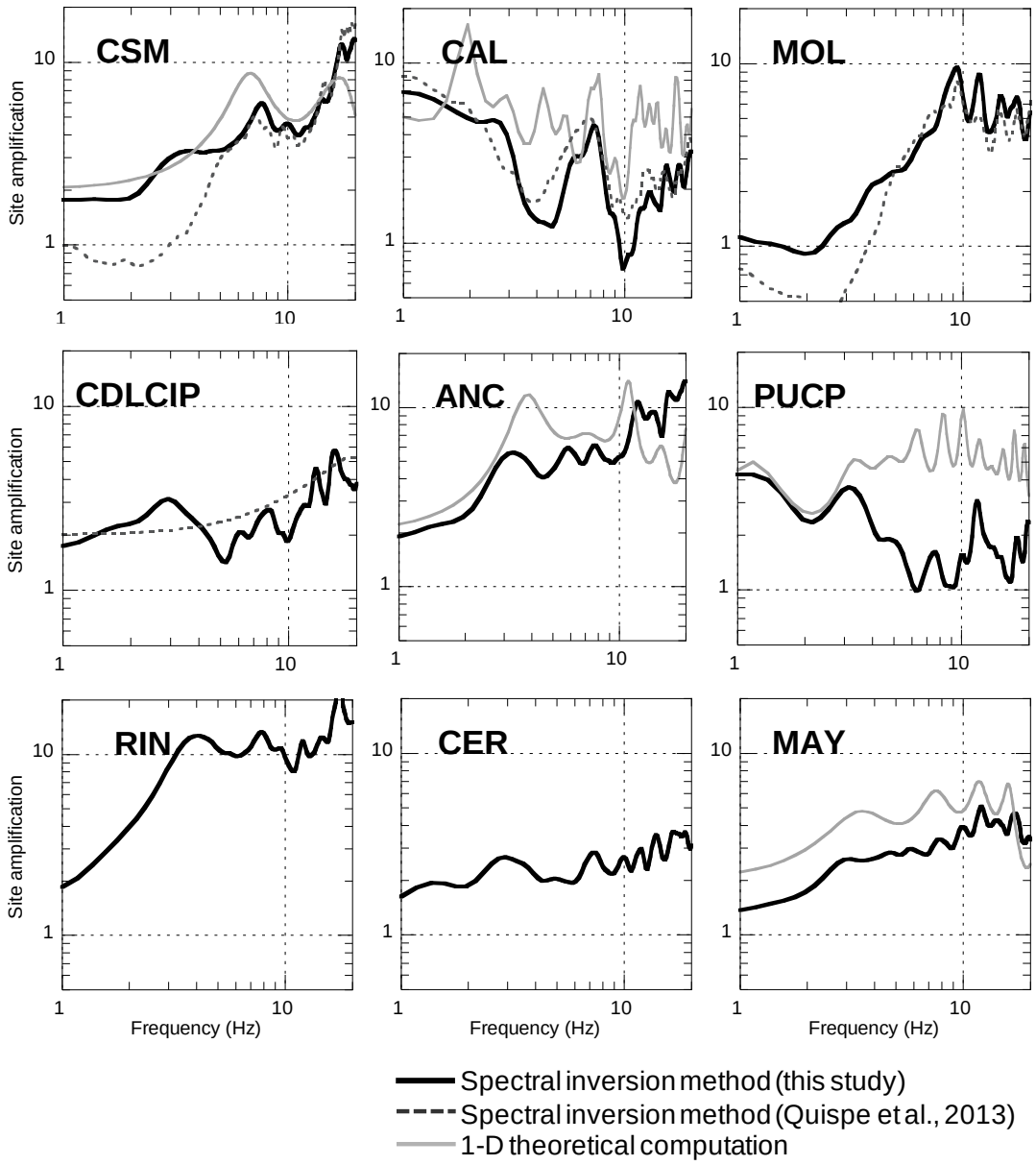

Figure 38. Amplification factors at sediment sites calculated by the inversion technique and 1-D theoretical computation. The black solid lines represent the site response estimated in this study, while the grey dashed lines represent the results previously estimated by Quispe et al. (2013). The grey solid lines indicate the theoretical transfer function from the bottom layer (Vs ~2200 m/s) to the ground surface. Vs structure at MOL, SMP, UNI1, UNI2, UNI3, and UNI4 stations is unknown.

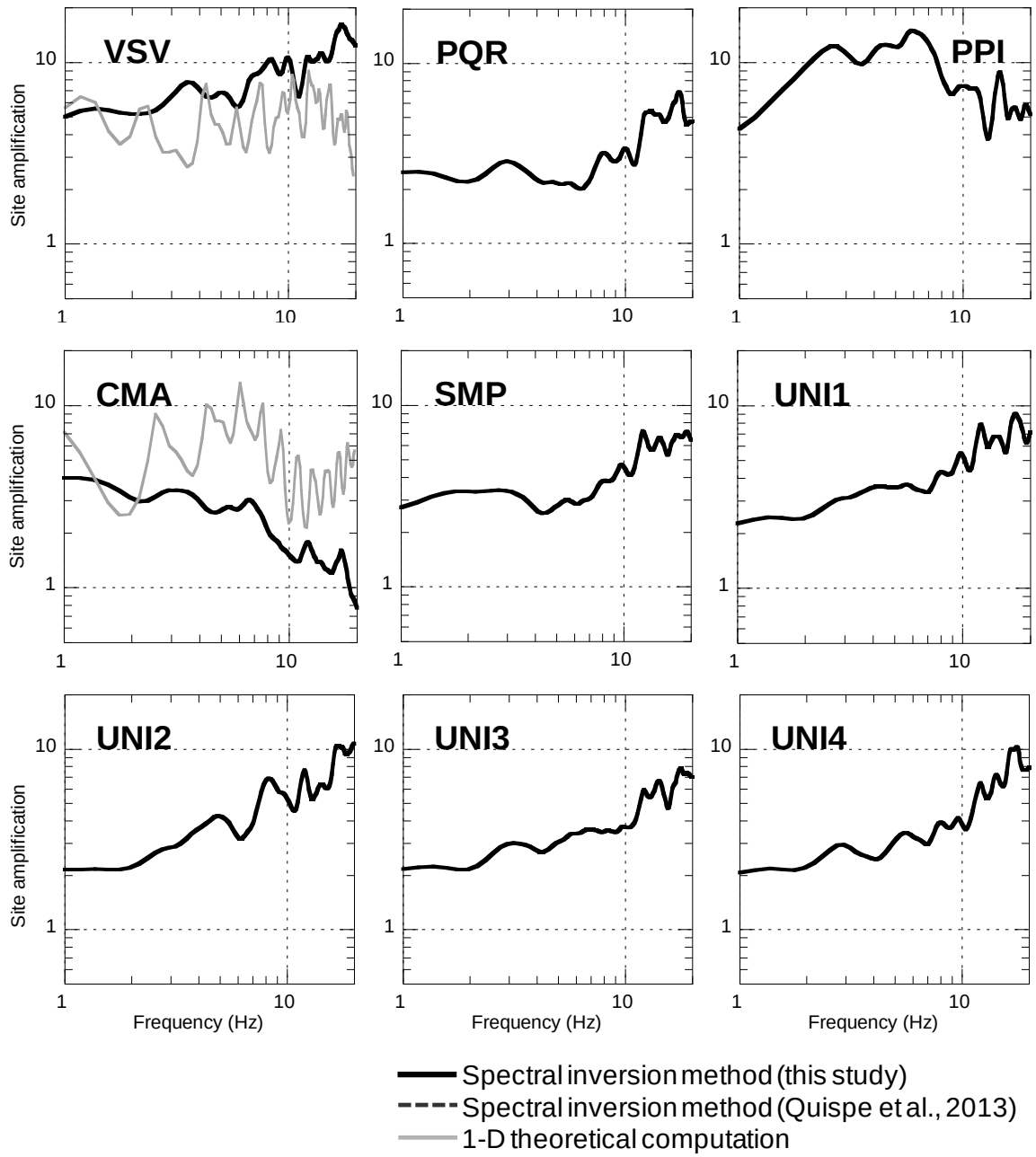

Figure 38 (*continued*). Amplification factors at sediment sites calculated by the inversion technique and 1-D theoretical computation. The black solid lines represent the site response estimated in this study, while the grey dashed lines represent the results previously estimated by Quispe et al. (2013). The grey solid lines indicate the theoretical transfer function from the bottom layer (Vs ~2200 m/s) to the ground surface. Vs structure at MOL, SMP, UNI1, UNI2, UNI3, and UNI4 stations is unknown.

3.5 Discussion

3.5.1 Comparison among Different Techniques

Site response calculated from the spectral inversion method was compared with two empirical techniques, the observed Standard Spectral Ratio technique (SSR) (Borcherdt, R. D., 1970) and the observed Horizontal-to-Vertical Spectral Ratio technique (HVSR) (Lermo and Chávez-García, 1993) for earthquake data. Same database used in the inversion technique was evaluated for the calculation of SSR and HVSR. Figure 39 displays the results estimated from these empirical techniques. Black solid line represents the site effect derived from the inversion calculation at each station. Grey solid line represents the amplification for the S-wave portion of records calculated from the SSR, and grey dashed line indicates the results obtained using the H/V ratio technique. SSR calculation for few sites is not presented as shown in Figure 39, because not enough earthquake data was simultaneously recorded both for reference and sediment sites. The LMO rock site was also used as a reference site for SSR calculation. Note that due to the consideration of free surface amplification, results obtained from SSR and HVSR were multiplied by a factor of 2.

Figure 39 shows similarity in the shape of site spectra between the three techniques, which supports the validity of the inversion results in relation to predominant frequency peaks. Nonetheless, it is important to mention the definition of absolute amplification is systematically different from each technique. In the Spectral Inversion Method, the three effects – path, source and site – are automatically separated. The site response is defined as the ratio between the surface motion and the input motion from the bottom layer of the model for the reference site. The Standard Spectral Ratio technique defines site amplification as the ratio of surface motion at each site to surface motion at the reference site. Site response calculated from SSR includes the slight amplification of the reference site, while in the inversion technique is not included. The propagation path effect is also included in the SSR. Although the separation distance between sediment and reference sites is less than the hypocentral distance, the effect of propagation path of seismic energy is not the same for each one.

In terms of the Horizontal-to-Vertical Spectral Ratio technique, site amplification is defined as the ratio of horizontal motion at surface to vertical motion at surface. Site response estimated from HVSR differs from the inversion technique, since vertical component is affected by amplification of the same order of magnitude as horizontal components (Riepl et al., 1998).

The three empirical techniques offers information about significant frequencies, but differences are still observed as shown in Fig. 39, due to the difference of their definitions. Amplification spectra estimated from the spectral inversion method are only attributed to the effect of sedimentary soil layers over a basement, indicating this technique is the most appropriate and accurate for analyzing amplification effects compared with the SSR and HVSR techniques. The author does not play down the applicability of these spectral ratio techniques at all. The SSR and HVSR techniques are still in use since both of them have the advantage of being fast and easy to apply for gaining some information about frequencies at which important amplification might appear, which can be important for practical applications.

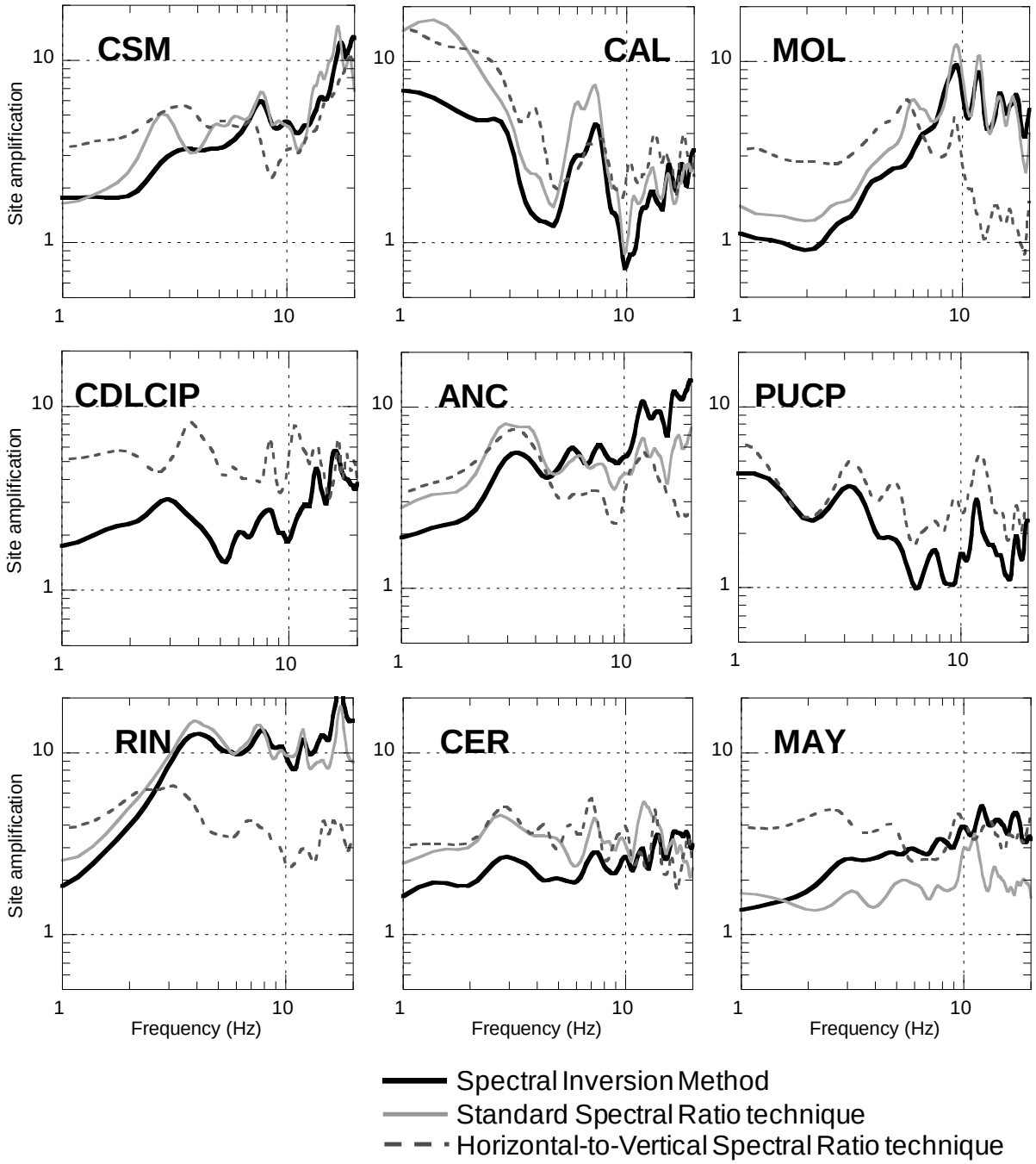

Figure 39. Comparison of site response estimates for the S-wave portions of records. Black solid lines represent the site response estimated from the inversion technique, while the grey solid and dashed lines represent the results estimated from the standard and horizontal-to-vertical spectral ratio techniques, respectively.

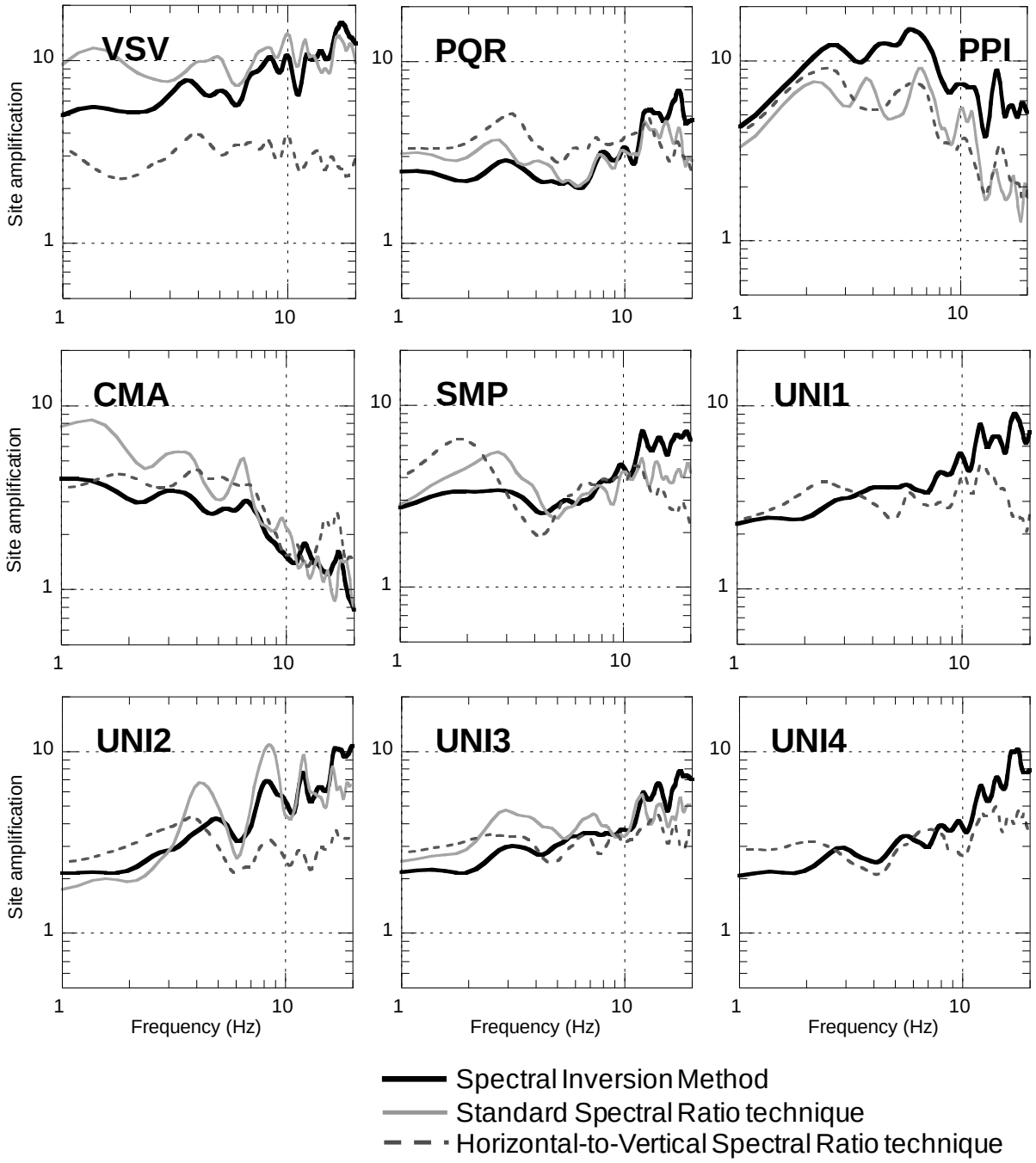

Figure 39 (*continued*). Comparison of site response estimates for the S-wave portions of records. Black solid lines represent the site response estimated from the inversion technique, while the grey solid and dashed lines represent the results estimated from the standard and horizontal-to-vertical spectral ratio techniques, respectively.

3.5.2 Surface Geology and Local Site Amplification

In this section, the site response of the sediment sites is discussed based on the inversion results. The geological map of Lima shows all the sediment sites are located on Quaternary deposits (Fig. 29), but the surface condition for each site differs. The predominant alluvial material over Lima Metropolitan Area is the Lima Conglomerate. The distribution and properties of the various subsurface soils overlying the conglomerate are displayed in the soil distribution map of Lima proposed by CISMID (2005). The subsurface conditions were grouped into four soil types – gravels, silty sands, aeolian sands, and clays – to simplify the variety of soil materials (Sekiguchi et al., 2013).

According to this map (CISMID, 2005), CSM, MOL, CDLCIP, PUCP, CER, PQR, SMP, UNI1, UNI2, UNI3 and UNI4 stations are located on alluvial gravel. All of them are installed in different districts of Lima province as presented in Table 6. These sites show the highest amplifications levels at frequencies above 3 Hz, corresponding to the site response of the Lima conglomerate, previously reported by Quispe et al. (2013, 2014). The Lima conglomerate extends from near the ground's surface to the bedrock, with S-wave velocities increasing gradually with depth from ~400 to ~1500 m/s (Repetto et al., 1980; Calderon et al., 2012; Quispe et al., 2014).

RIN (La Molina district) and PPI (Puente Piedra district) sites are installed on layers of sand and silt overlying the Lima conglomerate (CISMID, 2005). These sites show several peaks at frequencies higher than 5 Hz (Fig. 38), representing the resonance between the top layers (Vs ranging within ~100 and ~500 m/s) and the alluvial deposits (Quispe et al., 2014). RIN and PPI sites show dominant peaks with high amplification at frequencies below 5 Hz, attributed to the velocity contract between the deep soil layers – underlying the engineering bedrock (Vs ~500 m/s) – and the top layers. This study as well as microtremor observations conducted at RIN and PPI sites (Calderon et al., 2012; Quispe et al., 2014) reveal these stations are located on layers of sand and silt with a thickness larger than 10 m, in contrary to what CISMID (2005) reported, so the soil classification map needs to be updated.

According to the soil distribution map, MAY station is also installed on silty sand deposits, but the amplification factors at this site is similar to those in gravel deposits. Microtremor observations conducted at this site (Quispe et al., 2014) as well as the results estimated in this study suggest that this station might be located on alluvial gravels.

VSV station is situated on thick aeolian sand deposits (CISMID, 2005; Calderon et al., 2012). The soil formation is the predominant soil type in the Villa El Salvador district, where the VSV recording site is installed. Large amplification factors in the frequency range over 5 Hz is attributed to the effects of the deposit with Vs ranging from ~200 and ~500 m/s, while the amplification factors at frequencies lower than 5 Hz correspond to the contribution of the high velocity layers (Vs ~1000 m/s) underlying the engineering basement.

Figure 38 shows the first resonance mode at ANC site is at a frequency between 3 to 4 Hz, also reported by Quispe et al. (2014). The soil distribution map of Lima proposed by CISMID (2005) provides scarce information at this site, located on the outskirts of Lima – Ancón district. Available geotechnical reports show the surface condition at the ANC site is predominantly aeolian sand layers with S-wave velocities between ~200 and ~500 m/s (Quispe et al., 2014).

Amplification levels at CMA site increase from high to low frequencies as shown in Fig. 38, and higher amplification is expected for frequencies lower than 1 Hz, also reported by Calderon et al. (2012). This study cannot define the amplification level at frequencies lower than 1 Hz because most of the analyzed S-wave Fourier Spectra are not so powerful at this frequency, as previously mentioned. The shallow soil condition at CMA shows two unconsolidated materials, a soft clay layer (Vs ~250 m/s) with a thickness of about 10 m, and a thick fine soil layer (Vs ~450 m/s). Stiff layers are found underlying these unconsolidated materials at a depth of ~150 m, with a Vs raging from ~1000 to ~2500 m/s gradually increasing with depth (CISMID, 2005; Calderon et al., 2012).

CAL site exhibits a dominant peak at a frequency of ~7 Hz, and also the amplification factor increases from high to low frequencies (Calderon et al., 2012; Quispe et al., 2013), as shown in Fig. 38. Large amplification at frequencies lower

than 5 Hz is the result of the velocity contrast between the ~25 m shallow materials (Vs ~250 m/s) and the high velocity layers (Vs larger than ~500 m/s). The shallow materials are mainly composed of clays, silts and sands (Repetto et al., 1980; CISMID, 2005). CAL and CMA stations are installed in Callao province. Historically large ground motions have been reported during important earthquakes in Callao because of the soil subsurface conditions (Espinoza et al., 1977).

After site response of each site has been discussed based on the results obtained from the Spectral Inversion Method, as well as using as a reference the Vs profiles obtained at the stations (Calderon et al., 2012; Quispe et al., 2014) and geotechnical reports (CISMID, 2005), this study concludes the common features of site amplification for several soil formations. Figure 40 shows the site response for all the stations installed on the same subsurface soil condition – gravels, sands (silty and aeolian sands) and clays. Figure 40 (a) reveals gravel deposits tend to amplify at frequencies higher than 3 Hz. This material has S-wave velocities increasing gradually with depth from ~400 to ~1500 m/s, as previously explained. The sand deposits amplify in a wide frequency range as shown in Fig. 40 (b). Large amplification factors in the frequency range over 5 Hz is attributed to the effects of the top layers – sands – with Vs ranging from ~100 to ~500 m/s, while amplification factors at frequencies lower than 5 Hz correspond to the high velocity contrast between the top and high velocity layers (Vs > ~800 m/s). From Fig. 40 (c) is observed that clay deposits also control the amplification in a wide frequency range, but clays have the particular characteristic of amplifying from high to low frequency compared to sands. The shallow layers are mainly composed of clays with Vs varying between ~100 and ~500 m/s, this material controls the amplification at frequency higher than 5 Hz. Large amplification at frequencies lower than 5 Hz is the result of the high velocity contrast between the shallow and deep layers (Vs > ~1000 m/s).

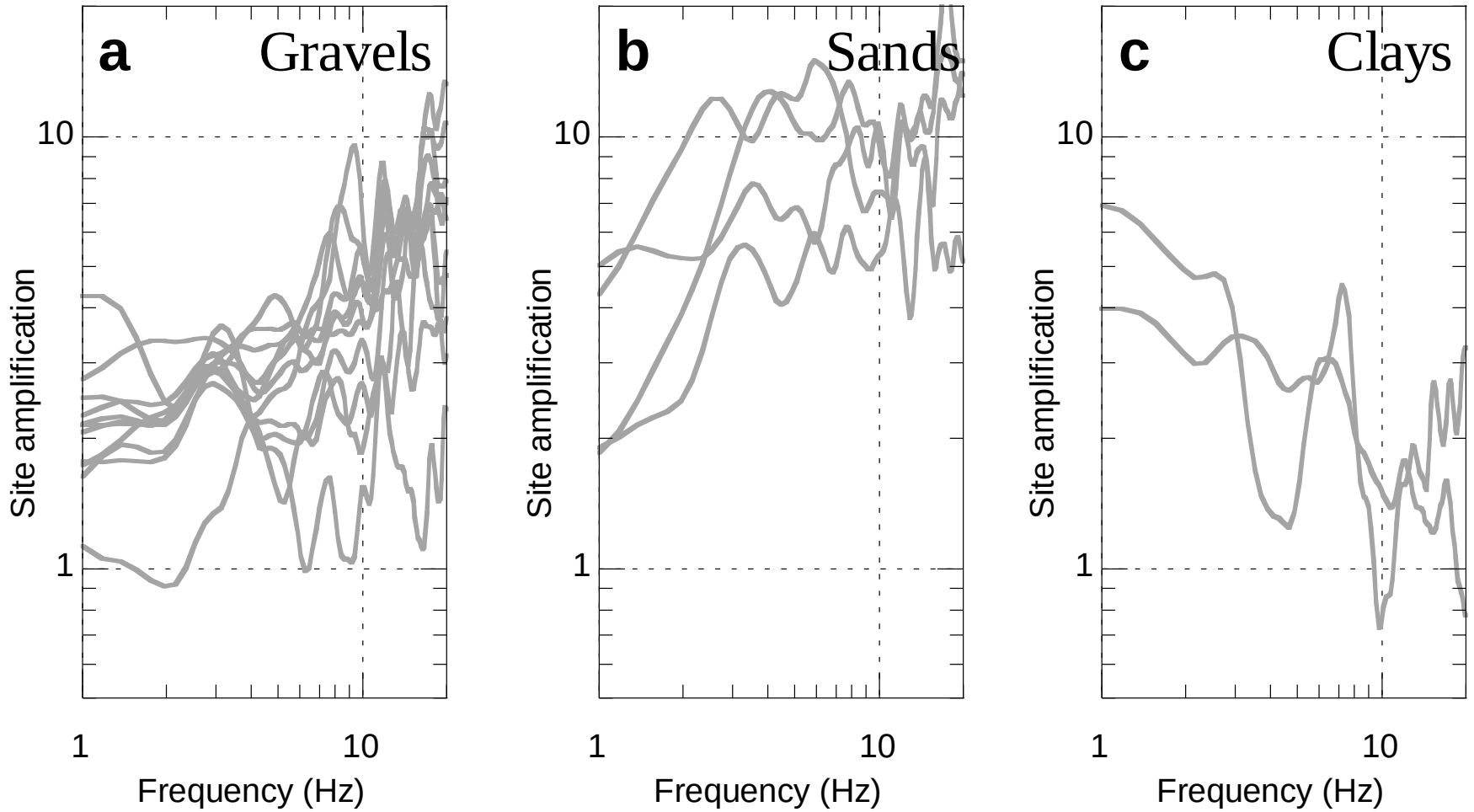

Figure 40. Site response for stations installed on (a) gravels, (b) sands, and (c) clays were plotted together in order to observe and discuss the common features for each soil formation.

CHAPTER 4

ESTIMATION OF FREQUENCY-DEPENDENT QS FOR SEDIMENTARY LAYERS FROM INVERSION OF SITE AMPLIFICATION

4.1 Methodology

The evaluation of site response in Lima Metropolitan Area is commonly estimated from Vs structure information (Calderon et al., 2012; Sekiguchi et al., 2013; Quispe et al., 2014). In these studies, the theoretical amplification factor has been computed with the assumption that quality factor for S-waves (Qs) is independent on frequency (f), since Qs as a function of frequency (f) and S-wave velocity (Vs) is still unknown for Lima Metropolitan Area. For example, Calderon et al. (2012) assumed $Qs = 25$ for all layers, while Quispe et al. (2014) used this representation of $Qs = Vs/10$.

In this chapter, S-wave velocities and frequency-dependent Qs are estimated at the earthquake recording sites. Microtremor observations have already been conducted for most of the sites in order to estimate the Vs structure (Calderon et al., 2012; Quispe et al., 2014), as explained in previous sections, but the separation distance between the field observation and the seismic station is more than 40 m away as shown in Table 9. It is now widely recognized that the surface soil conditions at two sites within a short distance may differ considerably. Nonetheless, the Vs models obtain from microtremor measurements are used as a reference for defining the new Vs models.

Table 9. Locations of Earthquake recording stations and microtremor array observations.

Station ID	Geographical coordinates of Earthquake station		Separation distance*
	Latitude (deg)	Longitude (deg)	(m)
CSM	-12.013	-77.050	~90
CAL	-12.066	-77.156	~160
MOL	-12.089	-76.930	N/A
ANC	-11.777	-77.150	~80
RIN	-12.087	-76.923	~100
CER	-12.103	-76.998	~200
MAY	-12.055	76.944	~40
UNI1	-12.021	-77.049	N/A
UNI2	-12.020	-77.048	N/A
UNI3	-12.022	-77.049	N/A
UNI4	-12.020	-77.050	N/A
VSV	-12.213	-76.938	~60
PQR	-12.073	-77.032	~260
SMP	-12.018	-77.056	N/A
PPI	-11.852	-77.074	~50
CMA	-12.060	-77.123	~120

*separation distance between earthquake station and central station in microtremor exploration

S-wave velocities and frequency-dependent Qs are estimated by inverting the observed site response. The observed amplification factors are the results obtained from the spectral inversion method, previously presented in Chapter 3. The S-wave velocities and Qs are estimated by finding the best fitting model between the observed and calculated amplification factors.

Qs as a function of frequency (f) and S-wave velocity (Vs) is modeled as the form of (Satoh, 2003):

$$Qs = \frac{Vs}{b} f^{a} \tag{9}$$

where a and b are constants determined in the inversion of the amplification factors, together with S-wave velocity and thickness. The constants a and b are assumed to be common to all the layers at a site.

The inversion technique to minimize the misfit between the observed, $G^O(f_i)$, and calculated, $G^C(f_i)$, amplification factors is the simulated annealing method. The details of the simulated annealing can be seen in Yamanaka (2005). In this study, the misfit function was defined as:

$$misfit = \sum_{i=1}^{N}[G^O(f_i) - G^C(f_i)]^2 \quad (10)$$

where N and f_i represent the number of the observed data and frequency, respectively. In the calculation of the final optimal $G^C(f_i)$, 10 inversion with 200 generations were conducted using different random numbers. The unknown parameters to be determined in the inversion were S-wave velocity (Vs) and thickness, as well as a and b that define the frequency-dependent Qs. Density values were set from 1.8 to 2.5 g/cm^3, depending on the soil type. Table 10 shows an example of the search limits at CSM site, as previously mentioned the search limits were defined considering the Vs models obtained from microtremor surveys (Calderon et al., 2012; Quispe et al., 2014).

Table 10. Search limit of parameters in inversion of amplification at CSM site.

Layer	**Vs (m/s)**	**Thickness (m)**	**Density (g/cm^3)**	**Quality factor**		
				b	**a**	**fo**
1	[290-400]	[1-10]	1.8			
2	[500-850]	[5-30]	2.0			
3	[1300-1700]	[5-20]	2.2	[1-50]	[0.1-1.0]	[1-21]
4	[1700-2000]	[50-100]	2.3			
5	[2200-2250]	-	2.4			

4.2 Identified S-wave Velocities and Frequency-Dependent Qs

The observed and theoretical amplification factors with the assumption that Qs depends on frequency for the sediment sites are shown in Figs. 41 (a1) ~ (p1), represented by grey dashed and black solid lines, respectively. In these figures are also plotted the transfer function when assuming Qs is independent on frequency (grey solid line), these results were previously shown in Fig. 38 for some stations. In Figs. 41 (a2) ~ (p2), the inverted S-wave velocity models (black line) and the underground structure model estimated from microtremor measurements (Calderon et al., 2012; Quispe et al., 2014) (grey line) are also shown. The observed dispersion curve obtained from the microtremor data (open circles) and the models that explain the observed phase velocity (grey line) are shown in Figs. 41 (a3) ~ (p3). These results were obtained by Calderon et al. (2012) and Quispe et al. (2014). The theoretical dispersion curve computed from the inverted Vs model is also shown in Figs. 41 (a3) ~ (p3) represented by a black line. The identified S-wave velocities and damping factors are displayed in Tables 11 (a) ~ (p).

The results show the site amplification characteristics of surface layers above the bottom layer (Vs ~2200 m/s) at the sediment sites can be explained well by the 1-D models with appropriate S-wave velocities and frequency-dependent damping factors as shown in Figs. 41 (a1) ~ (p1). As mentioned previously, the S-wave velocity models estimated from microtremor data (Calderon et al., 2012; Quispe et al., 2014) were used as a reference to define the search limit. The soil structure was necessary modified so that theoretical amplification factors with frequency-dependent Qs could explain well the observed site response. These differences are also observed in the theoretical transfer function when assuming frequency-dependent and frequency-independent Qs, black solid and grey dashed lines in Figs. 41 (a1) ~ (p1), respectively.

Figures 41 (a2) ~ (p2) display how much the inverted Vs profiles differ from models estimated from microtremor exploration. The explanation might be in relation to the separation distance between the center of the array configuration and the location where the earthquake recording station is installed. Table 9 gives pertinent information on distance between the center of the circular microtremor array

configuration and the seismic station. For stations such as CSM, CAL, ANC, RIN, MAY, VSV, PPI and CMA, the inverted Vs model shows a slight difference compared to the models proposed by Calderon et al. (2012) and Quispe et al. (2014). These differences are also observed in the phase velocity dispersion curve as shown in Figs. 41 (a3) ~ (p3). Phase velocity of surface waves reflects the S-wave velocity of the medium. However, two sites – CER and PQR – present higher phase velocities (open points and grey line) than the theoretical one computed from the inverted Vs model (black line) as shown in Figs. 41 (f3) and (i3), respectively. A possible explanation of these differences is discussed in the next section.

Microtremor measurements have not been conducted at MOL, SMP, UNI1, UNI2, UNI3, and UNI4 stations to date. So, the S-wave velocities estimated by inverting the observed site response should be used as a reference for future works.

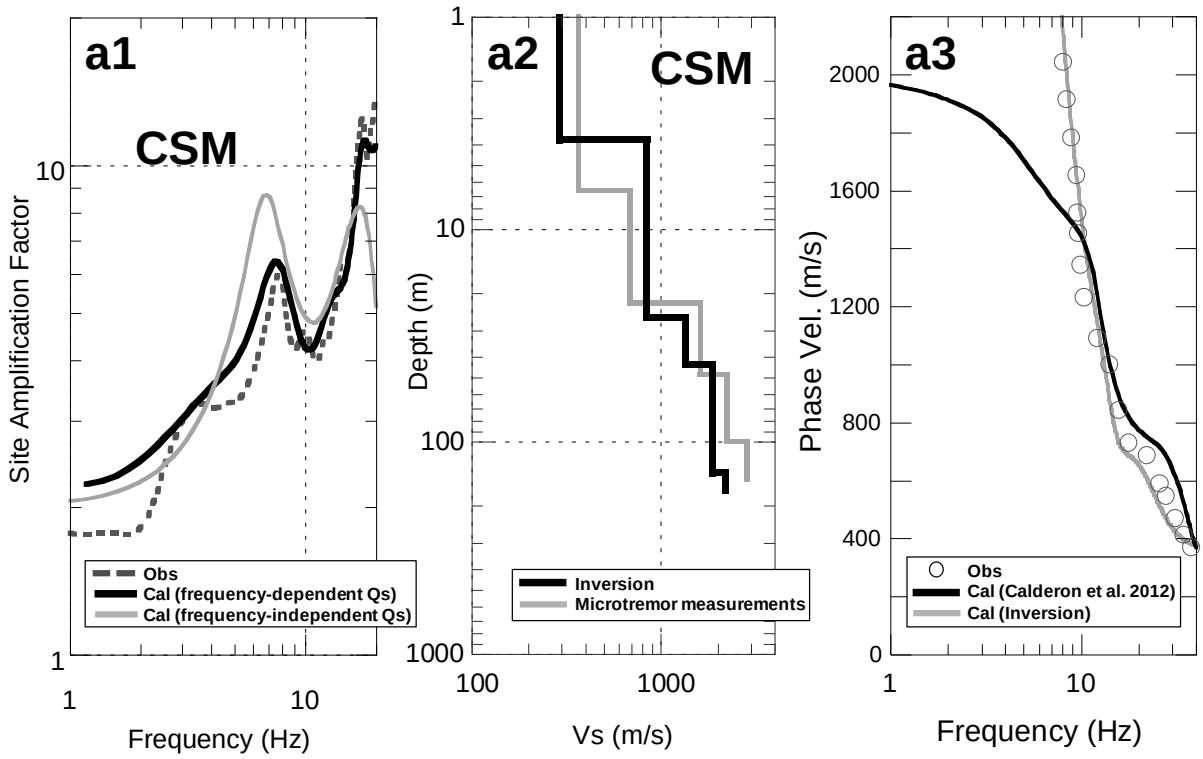

Figure 41 (a). (a1) Comparison of observed site response (grey dashed line) and theoretical amplification factors with the assumption frequency-dependent Qs (black solid line) and frequency-independent Qs (grey solid line). (a2) Black and grey lines indicate S-wave velocity models obtained from inversion and microtremor measurements (Calderon et al., 2012), respectively. (a3) Open points represent observed dispersion curve estimated from microtremor data, and the grey line indicates the model that explain the observed phase velocity estimated by Calderon et al. (2012). The black line represents the theoretical dispersion curve computed from the inverted Vs model.

Table 11 (a). S-wave velocities and frequency-dependent Qs estimated by inverting observed site response at CSM station.

Layer	Vs (m/s)	Thickness (m)	Density (g/cm^3)	Quality factor		
				b	a	fo
1	290.03	3.78	1.8			
2	843.26	22.16	2.0			
3	1337.12	16.84	2.2	39.8	0.34	18.0
4	1863.27	97.34	2.3			
5	2208.65	-	2.4			

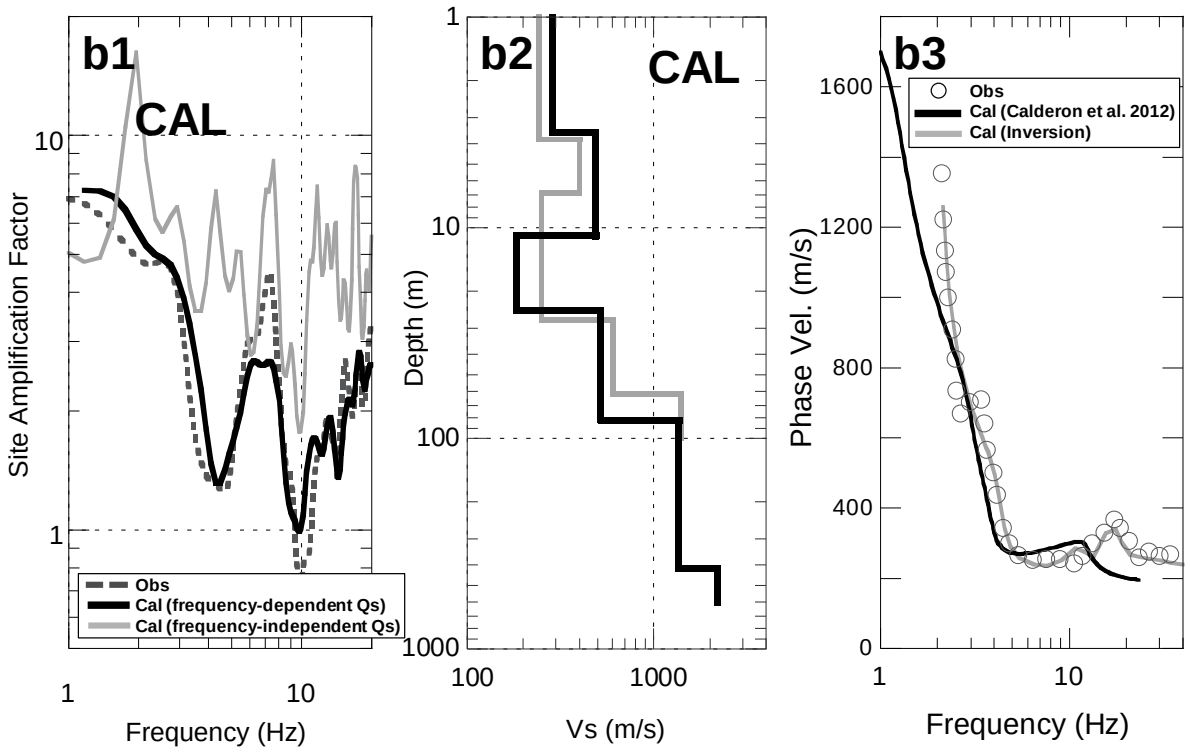

Figure 41 (b). (b1) Comparison of observed site response (grey dashed line) and theoretical amplification factors with the assumption frequency-dependent Qs (black solid line) and frequency-independent Qs (grey solid line) (b2) Black and grey lines indicate S-wave velocity models obtained from inversion and microtremor measurements (Calderon et al., 2012), respectively. (b3) Open points represent observed dispersion curve estimated from microtremor data, and the grey line indicates the model that explain the observed phase velocity estimated by Calderon et al. (2012). The black line represents the theoretical dispersion curve computed from the inverted Vs model.

Table 11 (b). S-wave velocities and frequency-dependent Qs estimated by inverting observed site response at CAL station.

Layer	Vs (m/s)	Thickness (m)	Density (g/cm^3)	Quality factor		
				b	a	fo
1	287.84	3.52	1.8	48.5	0.29	7.7
2	489.07	7.45	1.9			
3	183.49	13.92	1.8			
4	520.44	57.57	2.1			
5	1371.40	333.69	2.2			
6	2206.62	-	2.4			

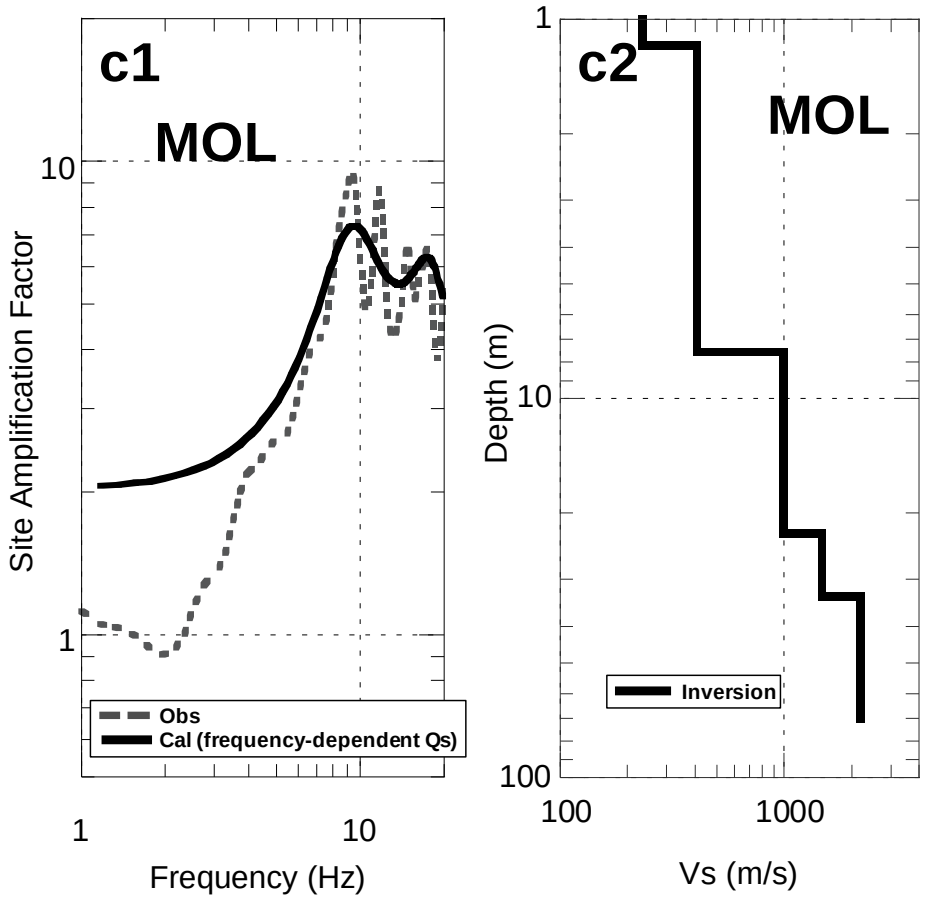

Figure 41 (c). (c1) Comparison of observed site response (grey dashed line) and theoretical amplification factors with the assumption frequency-dependent Qs (black solid line). (c2) Black line indicates S-wave velocity model obtained from inversion. No S-wave velocity subsurface structure was previously available at MOL station.

Table 11 (c). S-wave velocities and frequency-dependent Qs estimated by inverting observed site response at MOL station.

Layer	Vs (m/s)	Thickness (m)	Density (g/cm^3)	Quality factor		
				b	a	fo
1	231.68	1.17	1.8			
2	408.18	6.39	1.9			
3	994.54	15.20	2.1	43.0	0.65	2.5
4	1482.18	10.36	2.3			
5	2206.25	-	2.4			

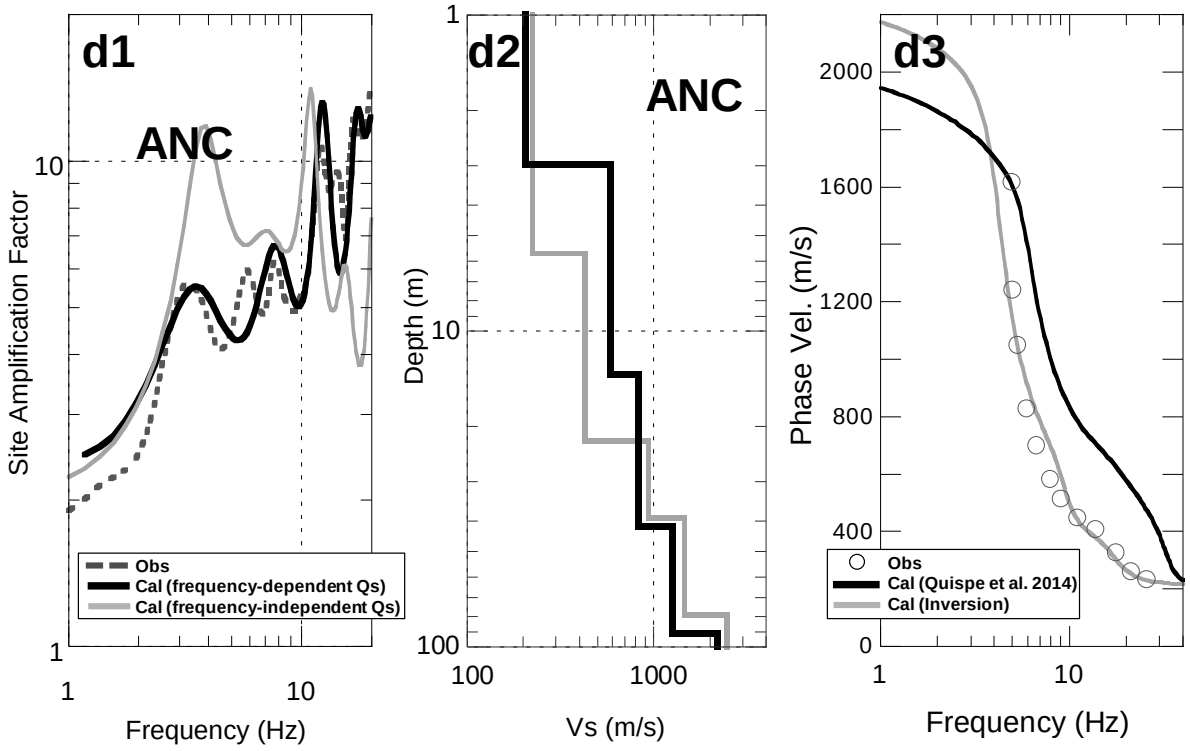

Figure 41 (d). (d1) Comparison of observed site response (grey dashed line) and theoretical amplification factors with the assumption frequency-dependent Qs (black solid line) and frequency-independent Qs (grey solid line). (d2) Black and grey lines indicate S-wave velocity models obtained from inversion and microtremor measurements (Quispe et al., 2014), respectively. (d3) Open points represent observed dispersion curve estimated from microtremor data, and the grey line indicates the model that explain the observed phase velocity estimated by Quispe et al. (2014). The black line represents the theoretical dispersion curve computed from the inverted Vs model.

Table 11 (d). S-wave velocities and frequency-dependent Qs estimated by inverting observed site response at ANC station.

Layer	Vs (m/s)	Thickness (m)	Density (g/cm^3)	Quality factor		
				b	a	fo
1	204.82	2.97	1.8			
2	592.24	10.78	1.9			
3	828.52	27.88	2.0	30.0	0.44	11.9
4	1257.67	49.29	2.2			
5	2204.75	-	2.4			

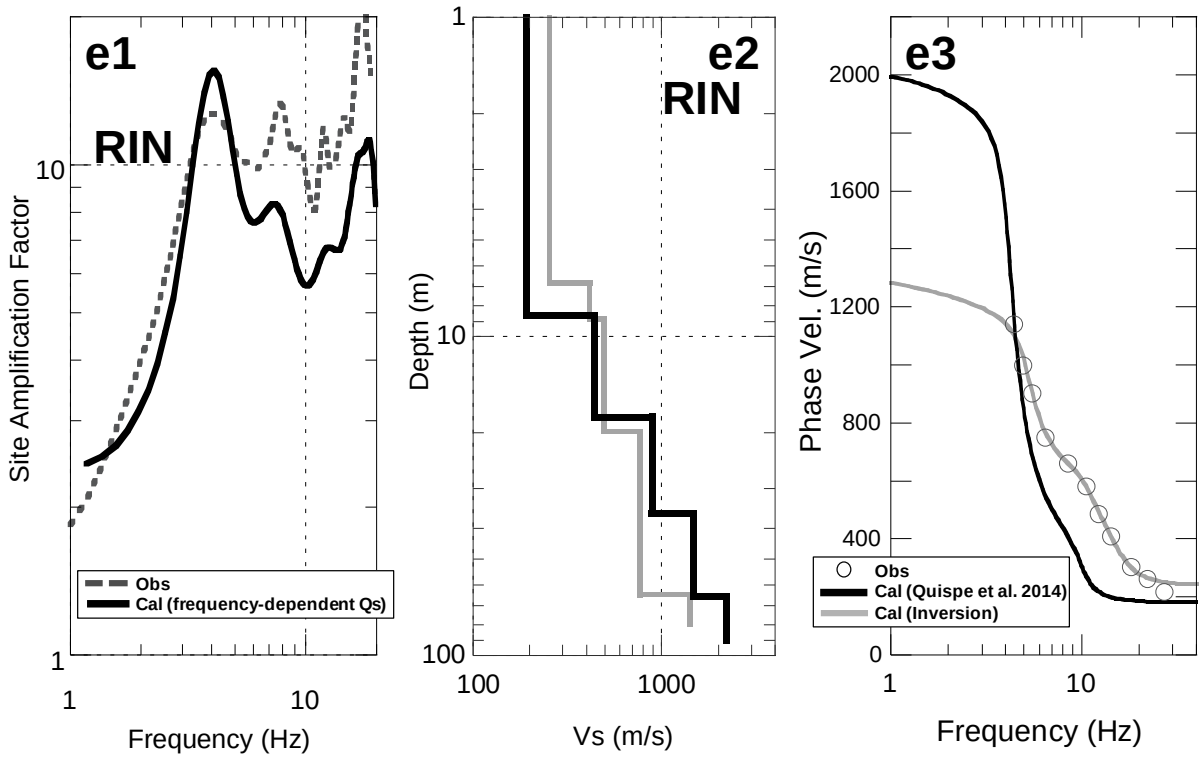

Figure 41 (e). (e1) Comparison of observed site response (grey dashed line) and theoretical amplification factors with the assumption frequency-dependent Qs (black solid line). (e2) Black and grey lines indicate S-wave velocity models obtained from inversion and microtremor measurements (Quispe et al., 2014), respectively. (e3) Open points represent observed dispersion curve estimated from microtremor data, and the grey line indicates the model that explain the observed phase velocity estimated by Quispe et al. (2014). The black line represents the theoretical dispersion curve computed from the inverted Vs model.

Table 11 (e). S-wave velocities and frequency-dependent Qs estimated by inverting observed site response at RIN station.

Layer	Vs (m/s)	Thickness (m)	Density (g/cm^3)	Quality factor		
				b	a	fo
1	191.26	8.59	1.8			
2	438.16	9.35	1.9			
3	891.73	17.91	2.0	2.2	0.86	14.3
4	1486.15	29.35	2.3			
5	2234.29	-	2.4			

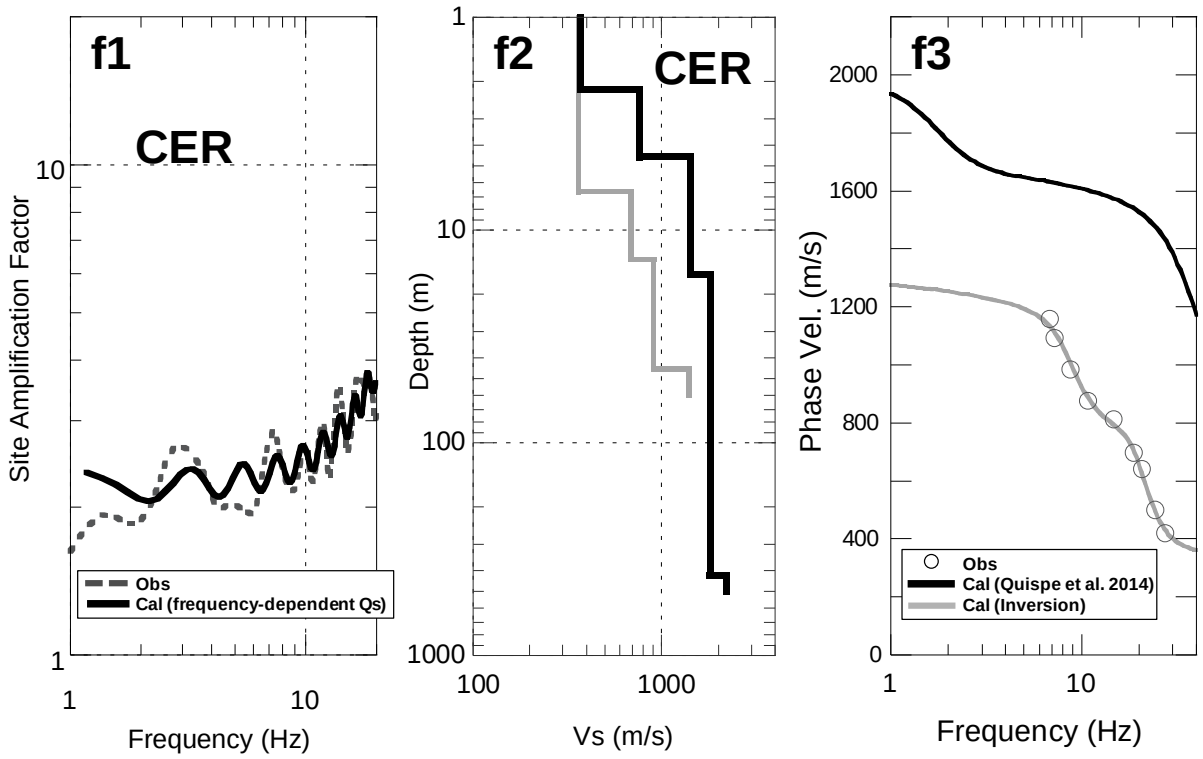

Figure 41 (f). (f1) Comparison of observed site response (grey dashed line) and theoretical amplification factors with the assumption frequency-dependent Qs (black solid line). (f2) Black and grey lines indicate S-wave velocity models obtained from inversion and microtremor measurements (Quispe et al., 2014), respectively. (f3) Open points represent observed dispersion curve estimated from microtremor data, and the grey line indicates the model that explain the observed phase velocity estimated by Quispe et al. (2014). The black line represents the theoretical dispersion curve computed from the inverted Vs model.

Table 11 (f). S-wave velocities and frequency-dependent Qs estimated by inverting observed site response at CER station.

Layer	Vs (m/s)	Thickness (m)	Density (g/cm^3)	Quality factor		
				b	a	fo
1	374.06	2.19	1.8			
2	756.77	2.34	2.0			
3	1421.36	11.78	2.2	41.4	0.50	8.7
4	1825.86	404.93	2.3			
5	2219.29	-	2.4			

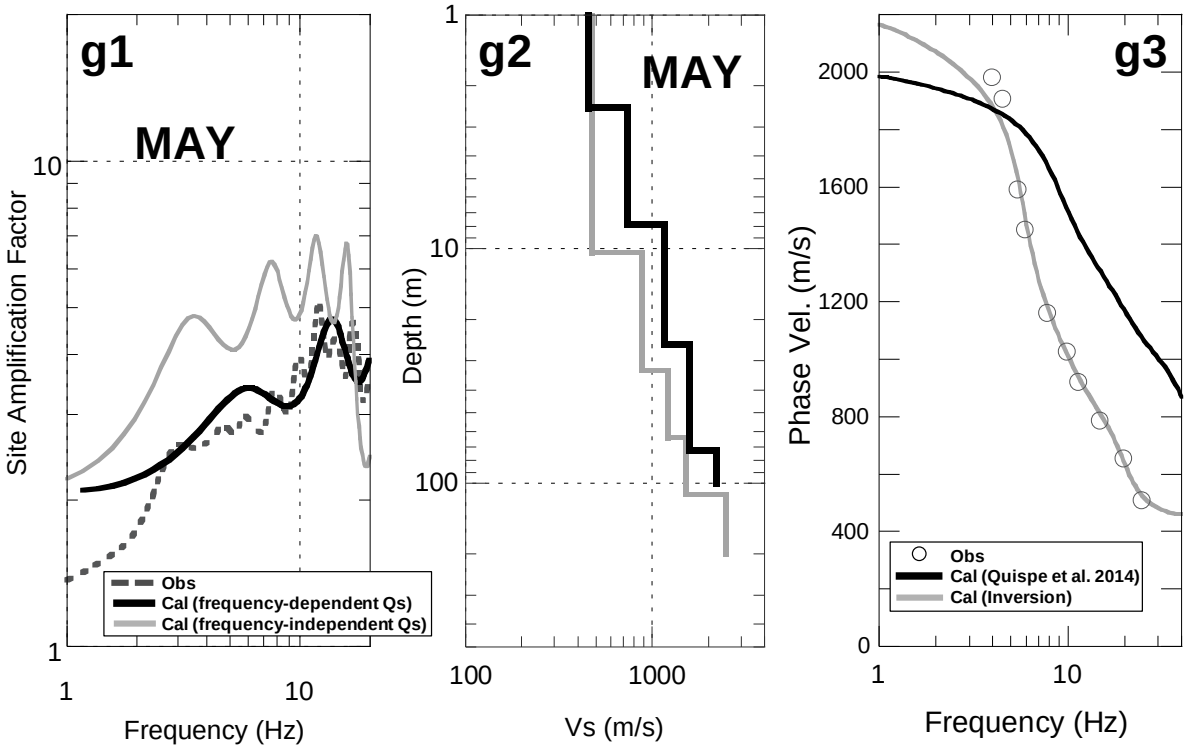

Figure 41 (g). (g1) Comparison of observed site response (grey dashed line) and theoretical amplification factors with the assumption frequency-dependent Qs (black solid line) and frequency-independent Qs (grey solid line). (g2) Black and grey lines indicate S-wave velocity models obtained from inversion and microtremor measurements (Quispe et al., 2014), respectively. (g3) Open points represent observed dispersion curve estimated from microtremor data, and the grey line indicates the model that explain the observed phase velocity estimated by Quispe et al. (2014). The black line represents the theoretical dispersion curve computed from the inverted Vs model.

Table 11 (g). S-wave velocities and frequency-dependent Qs estimated by inverting observed site response at MAY station.

Layer	Vs (m/s)	Thickness (m)	Density (g/cm^3)	Quality factor		
				b	a	fo
1	455.90	2.50	1.9			
2	734.24	5.30	2.0			
3	1167.03	17.67	2.2	43.9	0.49	3.8
4	1591.59	46.94	2.3			
5	2213.19	-	2.4			

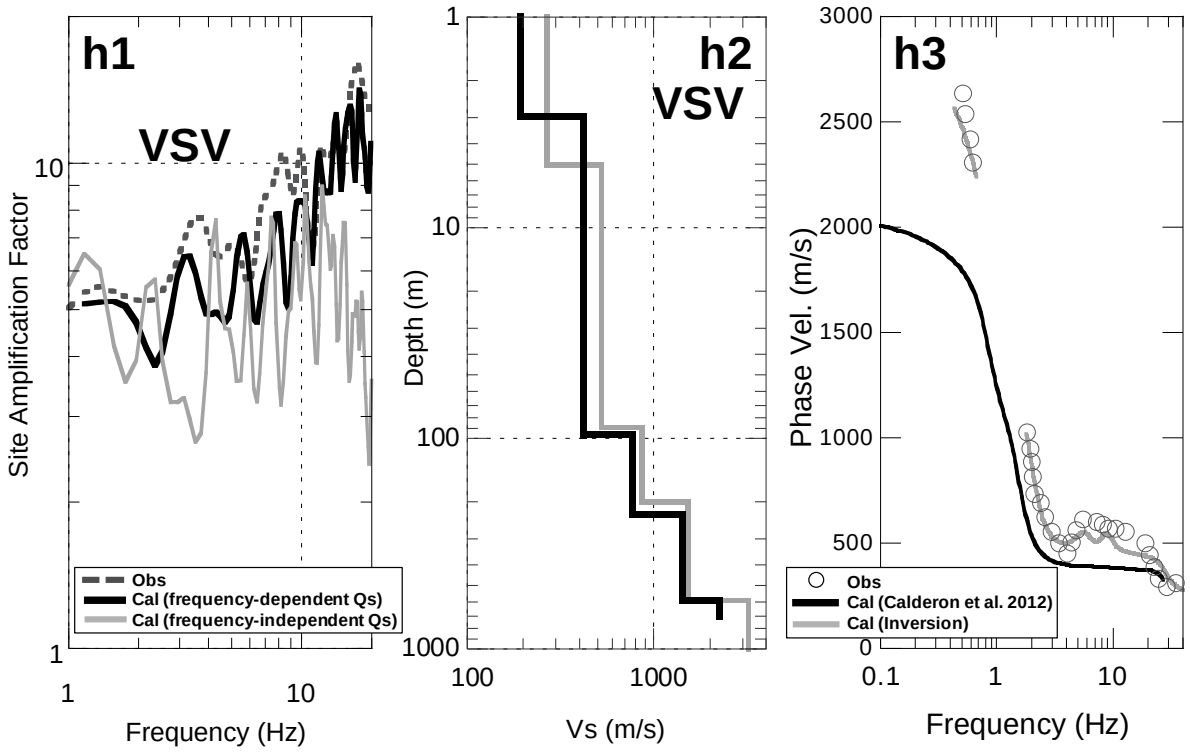

Figure 41 (h). (h1) Comparison of observed site response (grey dashed line) and theoretical amplification factors with the assumption frequency-dependent Qs (black solid line) and frequency-independent Qs (grey solid line). (h2) Black and grey lines indicate S-wave velocity models obtained from inversion and microtremor measurements (Calderon et al., 2012), respectively. (h3) Open points represent observed dispersion curve estimated from microtremor data, and the grey line indicates the model that explain the observed phase velocity estimated by Calderon et al. (2012). The black line represents the theoretical dispersion curve computed from the inverted Vs model.

Table 11 (h). S-wave velocities and frequency-dependent Qs estimated by inverting observed site response at VSV station.

Layer	Vs (m/s)	Thickness (m)	Density (g/cm^3)	Quality factor		
				b	a	fo
1	193.49	2.96	1.8			
2	421.30	93.27	1.9			
3	770.90	132.78	2.0	2.3	0.78	14.9
4	1424.04	361.96	2.3			
5	2238.85	-	2.4			

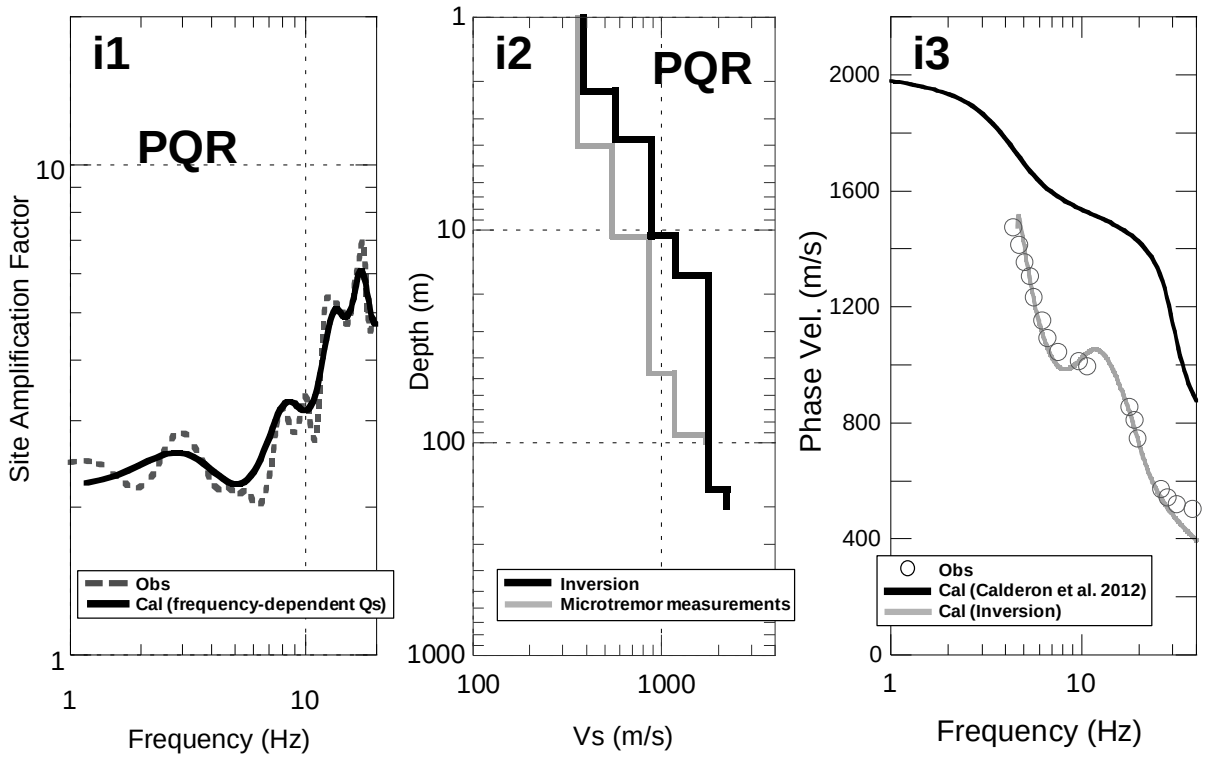

Figure 41 (i). (i1) Comparison of observed site response (grey dashed line) and theoretical amplification factors with the assumption frequency-dependent Qs (black solid line). (i2) Black and grey lines indicate S-wave velocity models obtained from inversion and microtremor measurements (Calderon et al., 2012), respectively. (h3) Open points represent observed dispersion curve estimated from microtremor data, and the grey line indicates the model that explain the observed phase velocity estimated by Calderon et al. (2012). The black line represents the theoretical dispersion curve computed from the inverted Vs model.

Table 11 (i). S-wave velocities and frequency-dependent Qs estimated by inverting observed site response at PQR station.

Layer	Vs (m/s)	Thickness (m)	Density (g/cm^3)	Quality factor		
				b	a	fo
1	385.48	2.22	1.8			
2	571.11	1.54	1.9			
3	886.22	6.94	2.0	44.7	0.38	12.1
4	1185.10	5.75	2.1			
5	1785.48	149.30	2.3			
6	2217.81	-	2.4			

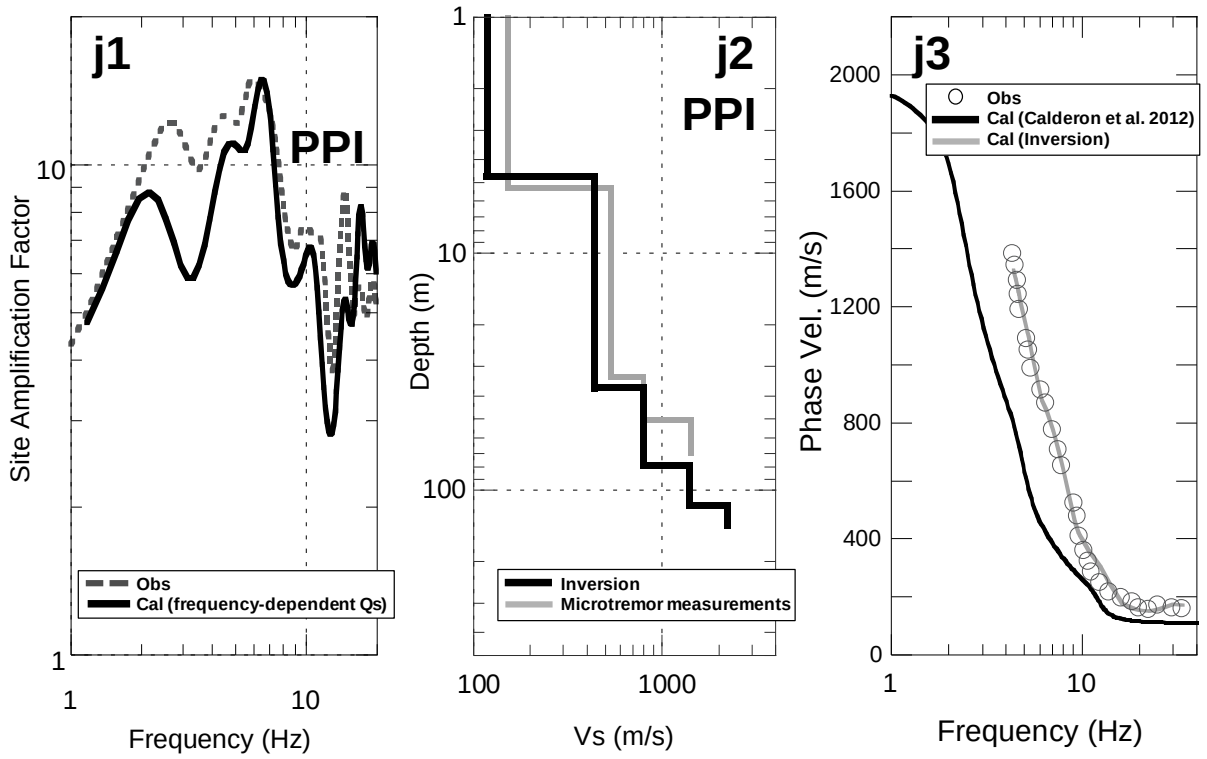

Figure 41 (j). (j1) Comparison of observed site response (grey dashed line) and theoretical amplification factors with the assumption frequency-dependent Qs (black solid line). (j2) Black and grey lines indicate S-wave velocity models obtained from inversion and microtremor measurements (Calderon et al., 2012), respectively. (j3) Open points represent observed dispersion curve estimated from microtremor data, and the grey line indicates the model that explain the observed phase velocity estimated by Calderon et al. (2012). The black line represents the theoretical dispersion curve computed from the inverted Vs model.

Table 11 (j). S-wave velocities and frequency-dependent Qs estimated by inverting observed site response at PPI station.

Layer	Vs (m/s)	Thickness (m)	Density (g/cm^3)	Quality factor		
				b	a	fo
1	117.52	4.70	1.8			
2	441.20	32.36	1.9			
3	797.47	41.50	2.0	15.6	0.63	2.4
4	1390.26	37.06	2.3			
5	2233.56	-	2.4			

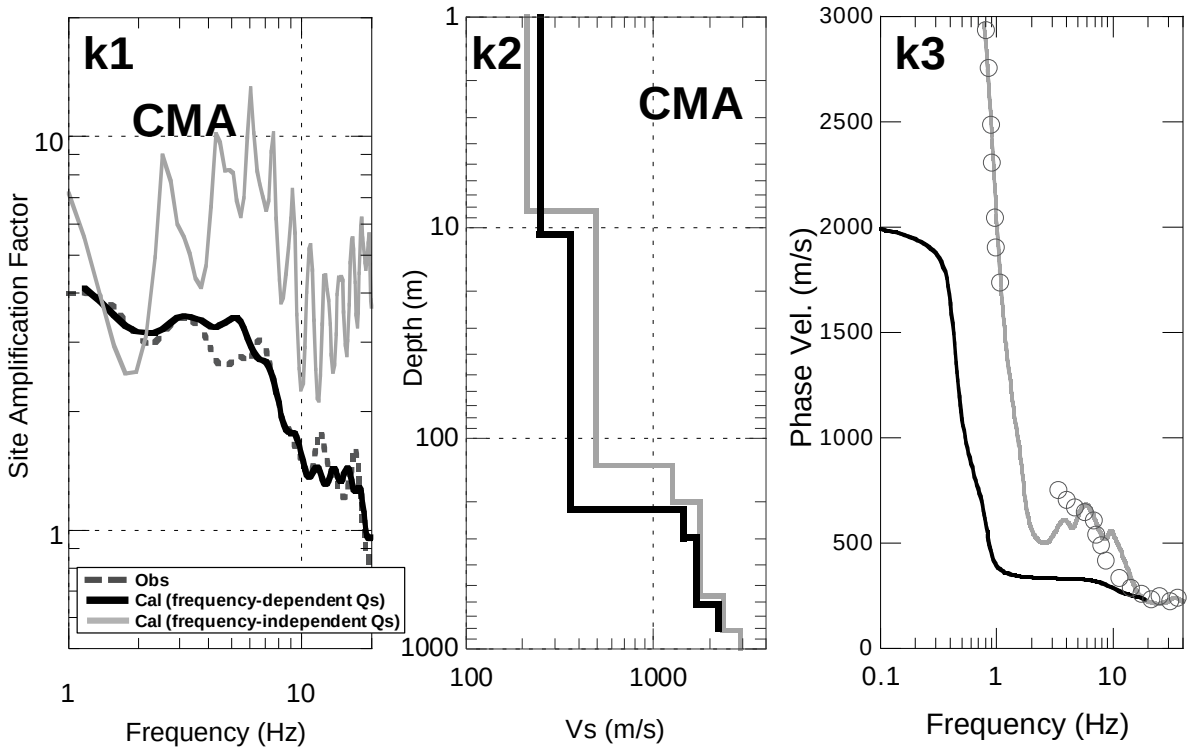

Figure 41 (k). (k1) Comparison of observed site response (grey dashed line) and theoretical amplification factors with the assumption frequency-dependent Qs (black solid line) and frequency-independent Qs (grey solid line) (k2) Black and grey lines indicate S-wave velocity models obtained from inversion and microtremor measurements (Calderon et al., 2012), respectively. (k3) Open points represent observed dispersion curve estimated from microtremor data, and the grey line indicates the model that explain the observed phase velocity estimated by Calderon et al. (2012). The black line represents the theoretical dispersion curve computed from the inverted Vs model.

Table 11 (k). S-wave velocities and frequency-dependent Qs estimated by inverting observed site response at CMA station.

Layer	Vs (m/s)	Thickness (m)	Density (g/cm^3)	Quality factor		
				b	a	fo
1	249.04	10.76	1.8			
2	360.89	206.33	1.9			
3	1447.75	79.22	2.2	39.3	0.27	17.0
4	1708.16	316.85	2.3			
5	2216.61	-	2.4			

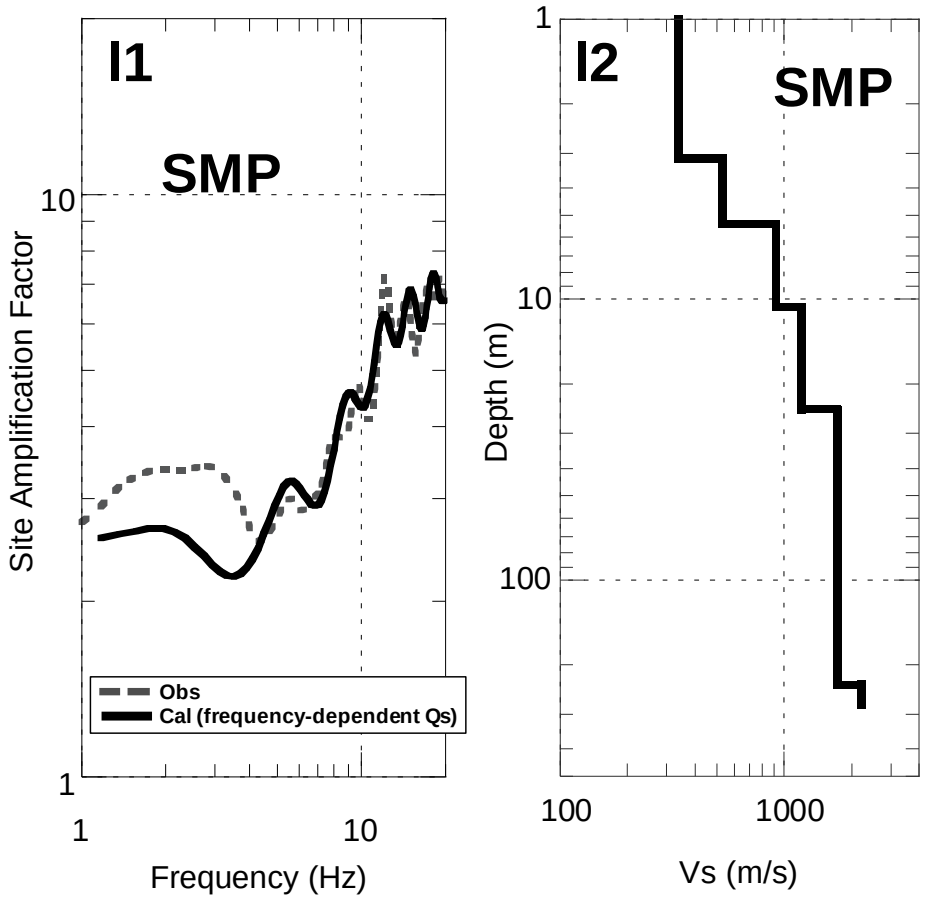

Figure 41 (l). (l1) Comparison of observed site response (grey dashed line) and theoretical amplification factors with the assumption frequency-dependent Qs (black solid line). (l2) Black line indicates S-wave velocity model obtained from inversion. No S-wave velocity subsurface structure was previously available at SMP station.

Table 11 (l). S-wave velocities and frequency-dependent Qs estimated by inverting observed site response at SMP station.

Layer	Vs (m/s)	Thickness (m)	Density (g/cm^3)	Quality factor		
				b	a	fo
1	337.77	3.14	1.8			
2	531.74	2.26	1.9			
3	921.06	5.19	2.0	30.4	0.35	6.5
4	1196.57	14.13	2.2			
5	1723.46	211.77	2.3			
6	2231.42	-	2.4			

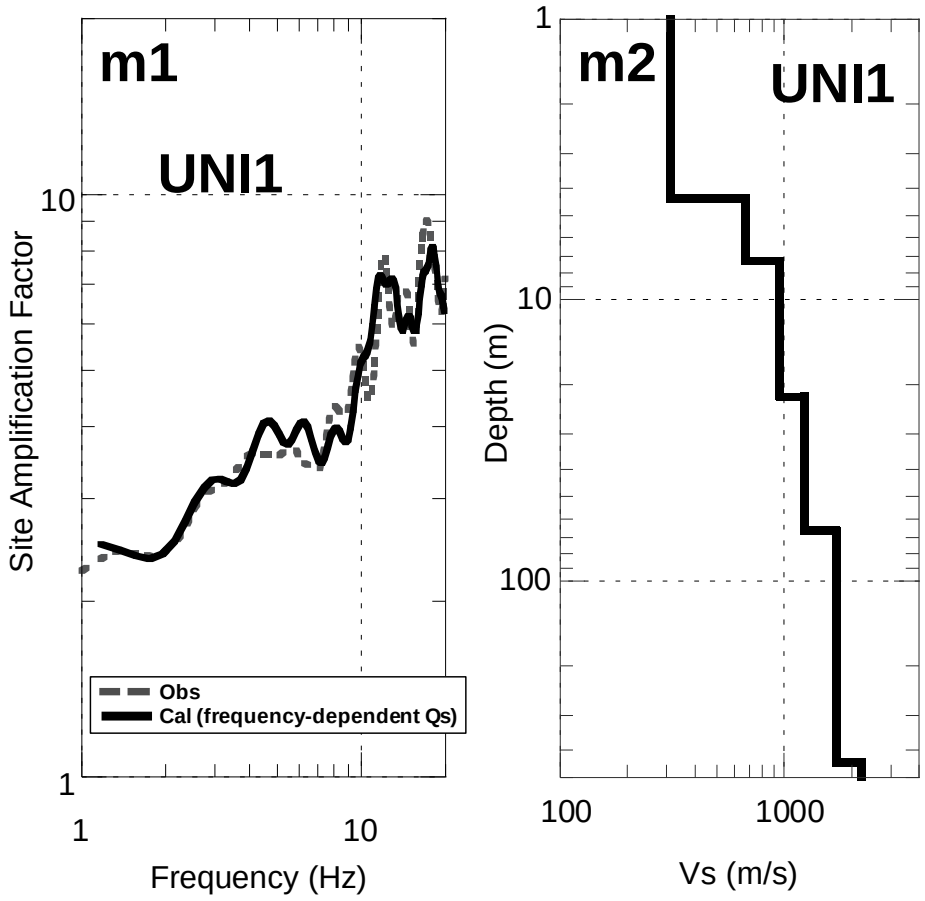

Figure 41 (m). (m1) Comparison of observed site response (grey dashed line) and theoretical amplification factors with the assumption frequency-dependent Qs (black solid line). (m2) Black line indicates S-wave velocity model obtained from inversion. No S-wave velocity subsurface structure was previously available at UNI1 station.

Table 11 (m). S-wave velocities and frequency-dependent Qs estimated by inverting observed site response at UNI1 station.

Layer	Vs (m/s)	Thickness (m)	Density (g/cm^3)	Quality factor		
				b	a	fo
1	309.76	4.38	1.8	41.1	0.38	20.9
2	674.00	2.87	1.9			
3	963.31	14.75	2.0			
4	1232.75	44.12	2.1			
5	1708.76	377.25	2.3			
6	2235.70	-	2.4			

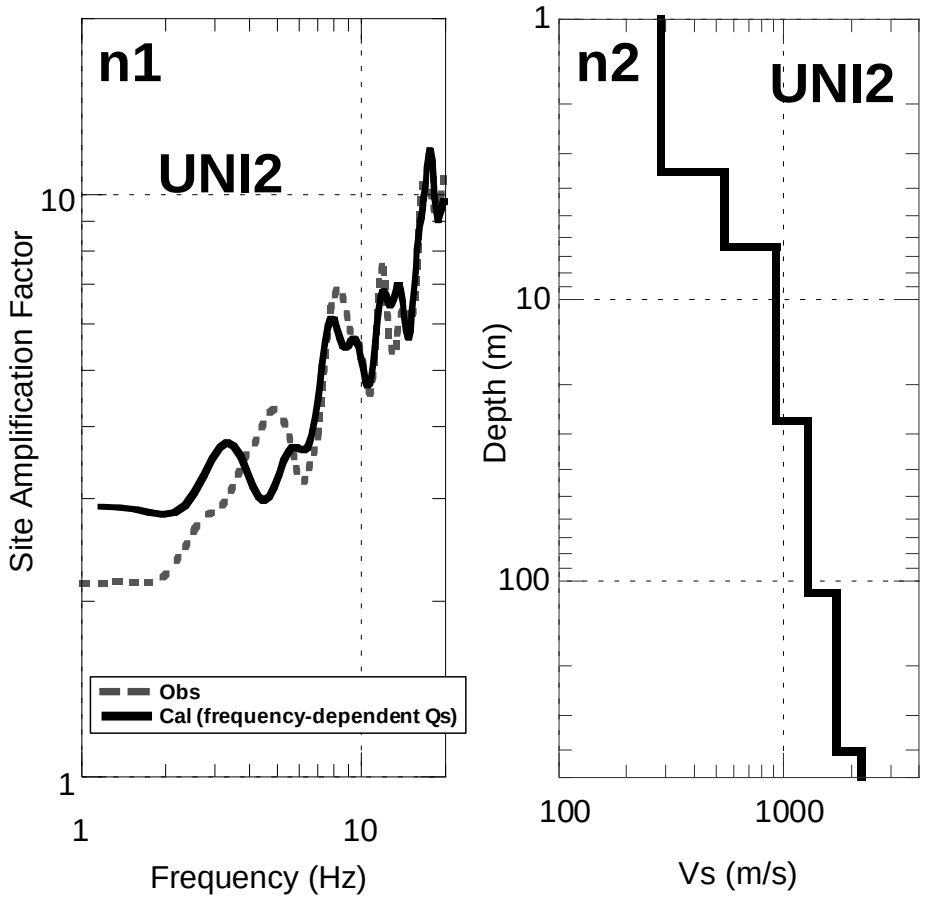

Figure 41 (n). (n1) Comparison of observed site response (grey dashed line) and theoretical amplification factors with the assumption frequency-dependent Qs (black solid line). (n2) Black line indicates S-wave velocity model obtained from inversion. No S-wave velocity subsurface structure was previously available at UNI2 station.

Table 11 (n). S-wave velocities and frequency-dependent Qs estimated by inverting observed site response at UNI2 station.

Layer	Vs (m/s)	Thickness (m)	Density (g/cm^3)	Quality factor		
				b	a	fo
1	283.80	3.51	1.8			
2	549.64	2.96	1.9			
3	927.33	20.55	2.0	46.9	0.60	12.3
4	1291.33	83.49	2.2			
5	1719.64	293.19	2.3			
6	2212.65	-	2.4			

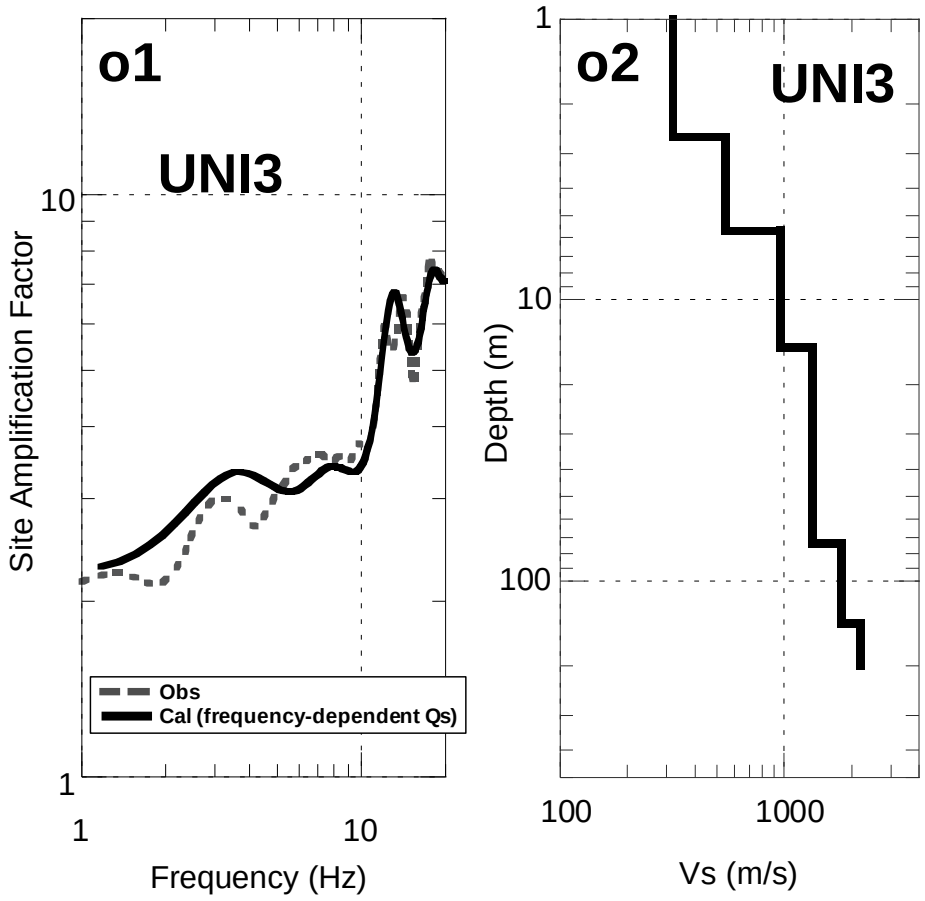

Figure 41 (o). (o1) Comparison of observed site response (grey dashed line) and theoretical amplification factors with the assumption frequency-dependent Qs (black solid line). (o2) Black line indicates S-wave velocity model obtained from inversion. No S-wave velocity subsurface structure was previously available at UNI3 station.

Table 11 (o). S-wave velocities and frequency-dependent Qs estimated by inverting observed site response at UNI3 station.

Layer	Vs (m/s)	Thickness (m)	Density (g/cm^3)	Quality factor		
				b	a	fo
1	317.29	2.63	1.8			
2	550.97	3.02	1.9			
3	970.36	9.16	2.0	37.4	0.41	8.8
4	1341.42	58.44	2.2			
5	1806.25	68.07	2.3			
6	2206.88	-	2.4			

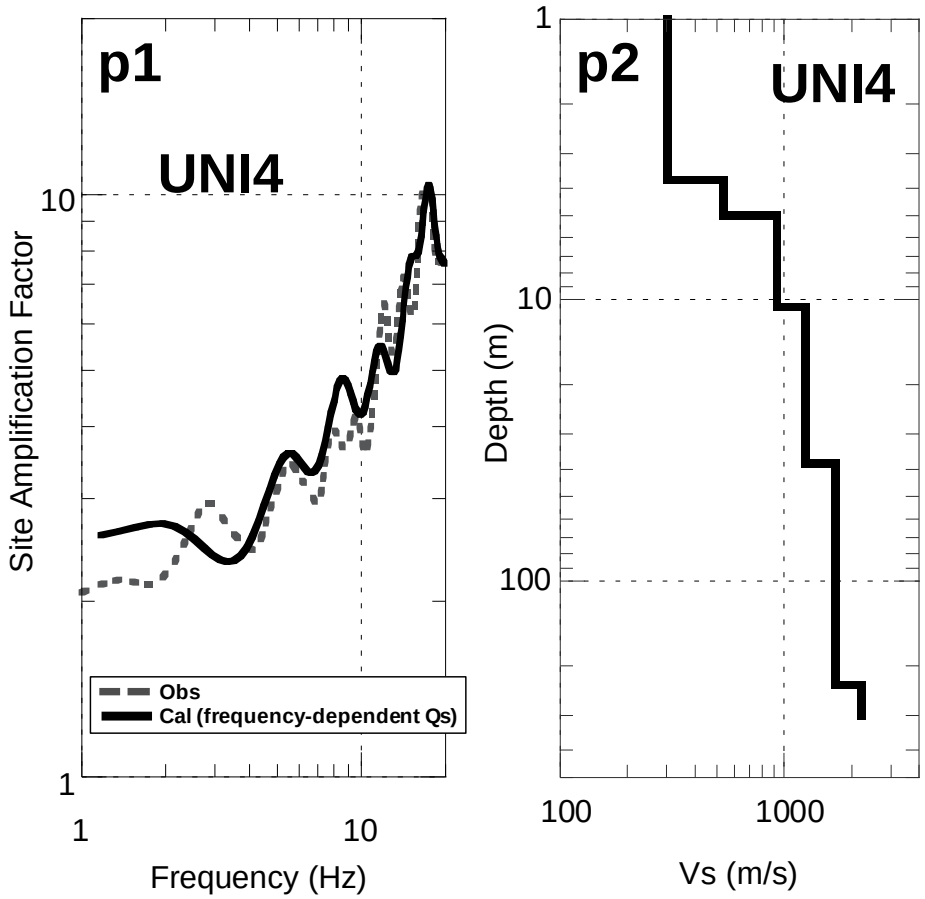

Figure 41 (p). (p1) Comparison of observed site response (grey dashed line) and theoretical amplification factors with the assumption frequency-dependent Qs (black solid line). (p2) Black line indicates S-wave velocity model obtained from inversion. No S-wave velocity subsurface structure was previously available at UNI4 station.

Table 11 (p). S-wave velocities and frequency-dependent Qs estimated by inverting observed site response at UNI4 station.

Layer	Vs (m/s)	Thickness (m)	Density (g/cm^3)	Quality factor		
				b	a	fo
1	302.14	3.74	1.8			
2	537.69	1.27	1.9			
3	932.73	5.50	2.0	39.5	0.60	15.4
4	1247.07	27.61	2.2			
5	1694.86	196.17	2.3			
6	2224.00	-	2.4			

4.2.1 Discussion

As previously mentioned, the theoretical dispersion curve computed from the inverted Vs models presents much higher phase velocities than those estimated by Calderon et al. (2012) and Quispe et al. (2014) for CER and PQR sites as shown in Figs. 41 (f3) and (i3), respectively. Table 9 displays the separation distance between the center of the array configuration and the place where the earthquake station was installed is less than 300 m for these two stations. The inverted results were expected to be similar to those of Calderon et al. (2012) and Quispe et al. (2014). In order to explain this discrepancy, S-wave velocities were fixed to be values of S-wave velocity profiles obtained from microtremor data. Figures 42 (a) and (b) display the results obtained from this calculation. The theoretical transfer function – computed when fixing S-wave velocity and thickness to the value obtained from microtremor data – cannot explain the observed site response in the frequency range of interest as shown in Figs. 42 (a1) and (b1). The theoretical and observed site amplifications are represented by black solid and grey dashed lines in Fig. 42 (a1) and (b1), respectively. Figures 42 (a2) and (b2) display the inverted Vs model (black line) and the S-wave velocity profile obtained from microtremor data (grey line).

The frequency-dependent Qs estimated by inverting the observed site response at the earthquake recording sites CER and PQR are consistent, although the theoretical dispersion curve is completely different than those obtained by Calderon et al. (2012) and Quispe et al. (2014). The author recommends another technique such as the joint inversion should be applied in order to simultaneously satisfy site amplification and phase velocity dispersion curve in the future.

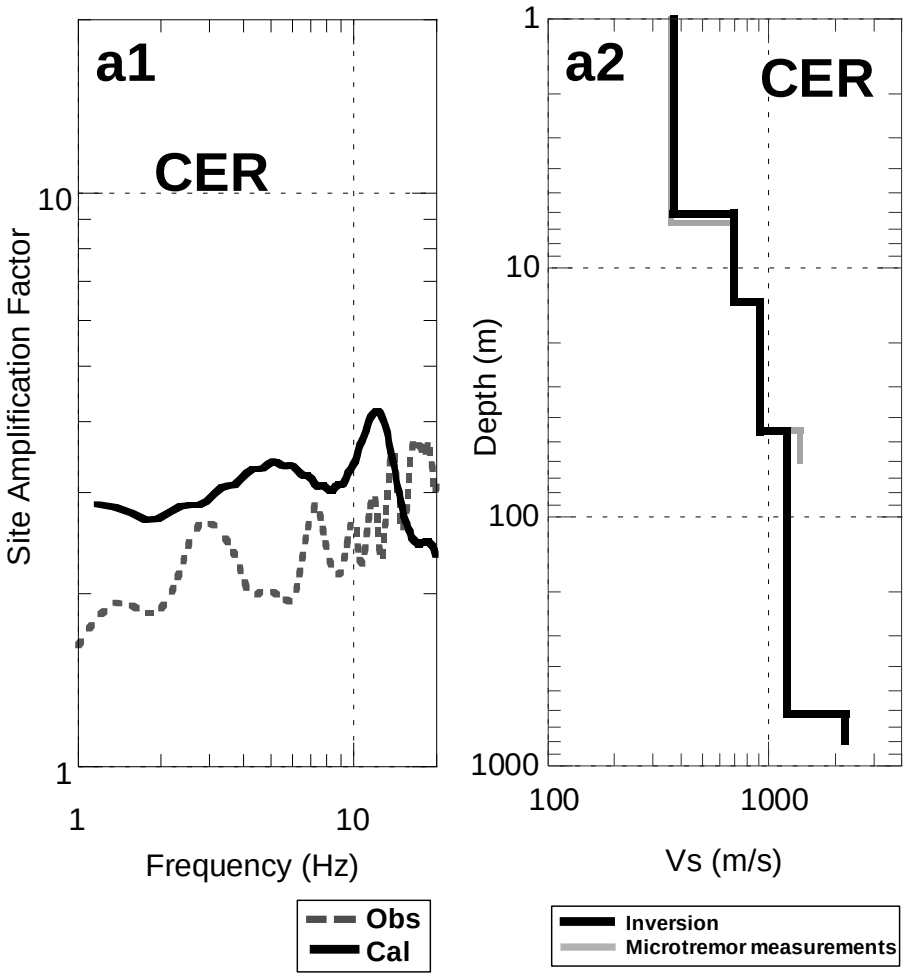

Figure 42 (a). (a1) The grey dashed line represents the observed site response estimated from the spectral inversion method, while the black solid line indicates the theoretical transfer function computed when fixing S-wave velocity and thickness to be values of microtremor data (Quispe et al., 2014). (a2) The S-wave velocity profile obtained from microtremor array observations at CER site is represented by a grey line (Quispe et al., 2014), while the inverted Vs model is represented by a black line.

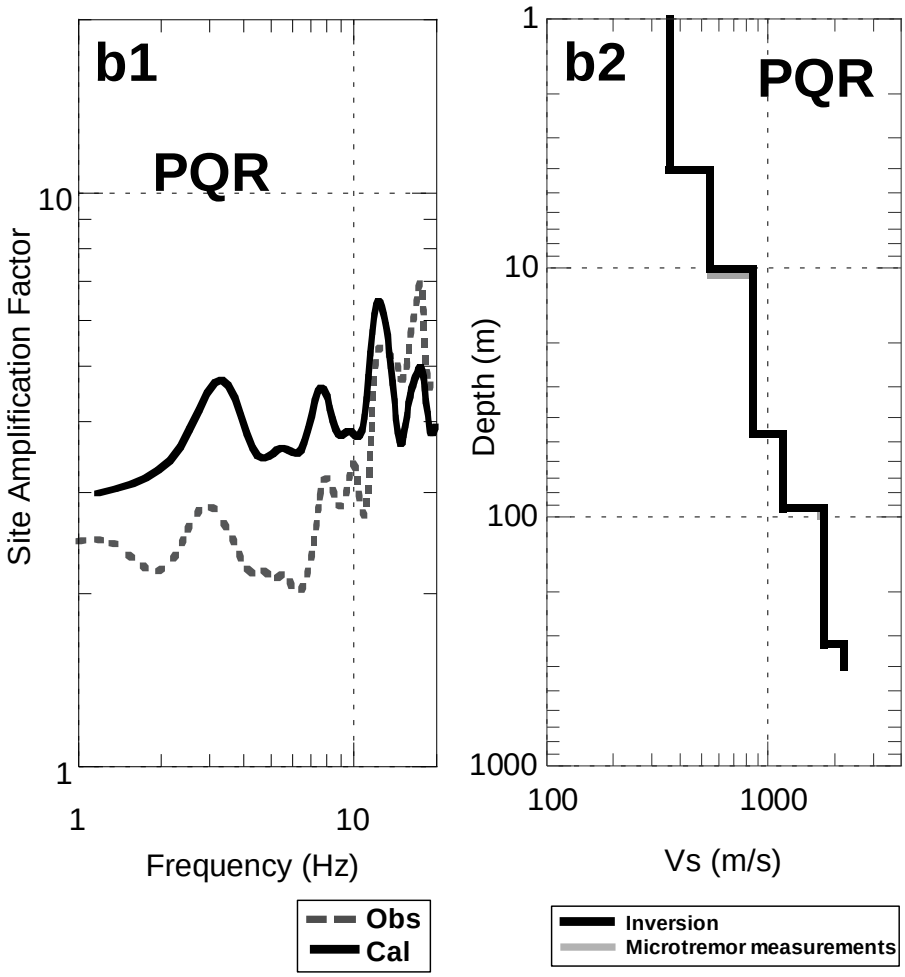

Figure 42 (b). (b1) The grey dashed line represents the observed site response estimated from the spectral inversion method, while the black solid line indicates the theoretical transfer function computed when fixing S-wave velocity and thickness to be values of microtremor data (Calderon et al., 2012). (a2) The S-wave velocity profile obtained from microtremor array observations at PQR site is represented by a grey line (Calderon et al., 2014), while the inverted Vs model is represented by a black line.

4.3 Regionality

The observed site response obtained from the Spectral Inversion Method shows that three predominant soil formations control the amplification at Lima Metropolitan Area – gravels, sands and clays, as previously discussed in Chapter 3. The quality factor Qs as a function of frequency (f) and S-wave velocity (Vs) $-Qs = (Vs/b)f^a -$ was also grouped based on the predominant subsurface soil conditions over Lima. The average of a, b and f_0 values was computed for sites installed on same surface conditions, and subsequently the standard deviation. The averages and standard deviations for each soil type are shown in Table 12. The b-values of gravels and clays are quite similar, as well as quite larger than the b-values of sands, whereas value of a for sands is the largest one compared to gravels and clays. Regarding the corner frequency fo, this parameter for each soil type is almost the same as shown in Table 12.

Table 12. Averages and standard deviations for each soil type.

Soil Types (# of stations)*		**Quality factor *Qs=(Vs/b)f^a***		
		b *Average ± Standard Deviation*	***a*** *Average ± Standard Deviation*	***f_0*** *Average ± Standard Deviation*
Gravels	(09 sites)	40.5 ± 4.7	0.47 ± 0.12	11.7 ± 5.8
Sands	(04 sites)	12.5 ± 13.3	0.68 ± 0.18	10.9 ± 5.8
Clays	(02 sites)	43.9 ± 6.5	0.28 ± 0.01	12.4 ± 6.6

*Number of stations installed on same surface conditions

The inverted 1-D soil profiles estimated from microtremor measurements (Calderon et al., 2012; Quispe et al., 2014) as well as the models computed by inverting the observed site response were gathered and plotted together on Fig. 43. A representative Vs profile for each soil type was chosen, which is represented by a black thick line in Fig. 43. Theoretical amplification factors with frequency-dependent Qs – identified in this study – were calculated by one-dimensional shear wave propagation theory for vertical incident S-wave (using the representative Vs profile in

Fig. 43), indicated by a black thick line in Fig. 44. The theoretical transfer function with frequency-independent Qs ($Qs = 25$) was also computed and plotted in Fig. 44, represented by a grey thin line. The representation of $Qs = 25$ for all layers was previously used by Calderon et al. (2012) in Lima Metropolitan Area.

The results reveals Qs as a function of frequency and Vs are less sensitive for gravel and sand deposits, while for clays the frequency-dependent quality factor Qs has a strong influence on the site response in a wide frequency range, as shown in Fig. 44. This study indicates clay deposits are the softest soil materials over Lima Metropolitan Area. This material has S-wave velocities ranging within ~200 and ~500 m/s, with a thickness relatively large, as previously explained in chapters 2 and 3. Qs significantly affects the attenuation of materials at high frequencies when the thickness of the shallow layers is large and Vs is small.

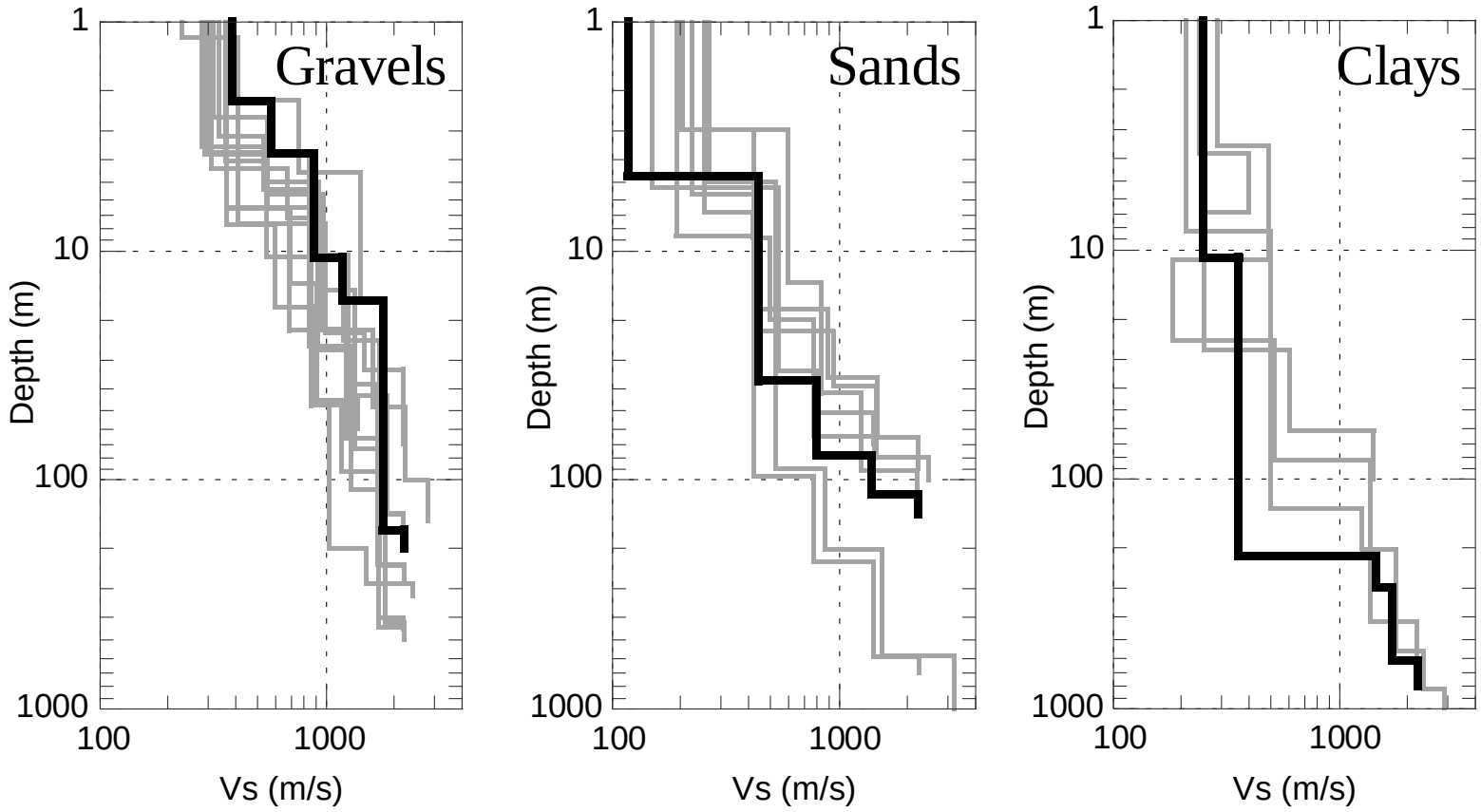

Figure 43. A representative Vs profile was chosen for each soil type in order to compute the theoretical transfer function. The black thick line indicates the representative Vs model, while the grey thin lines indicate profiles estimated from microtremor data as well as profiles computed from inverting the observed site response.

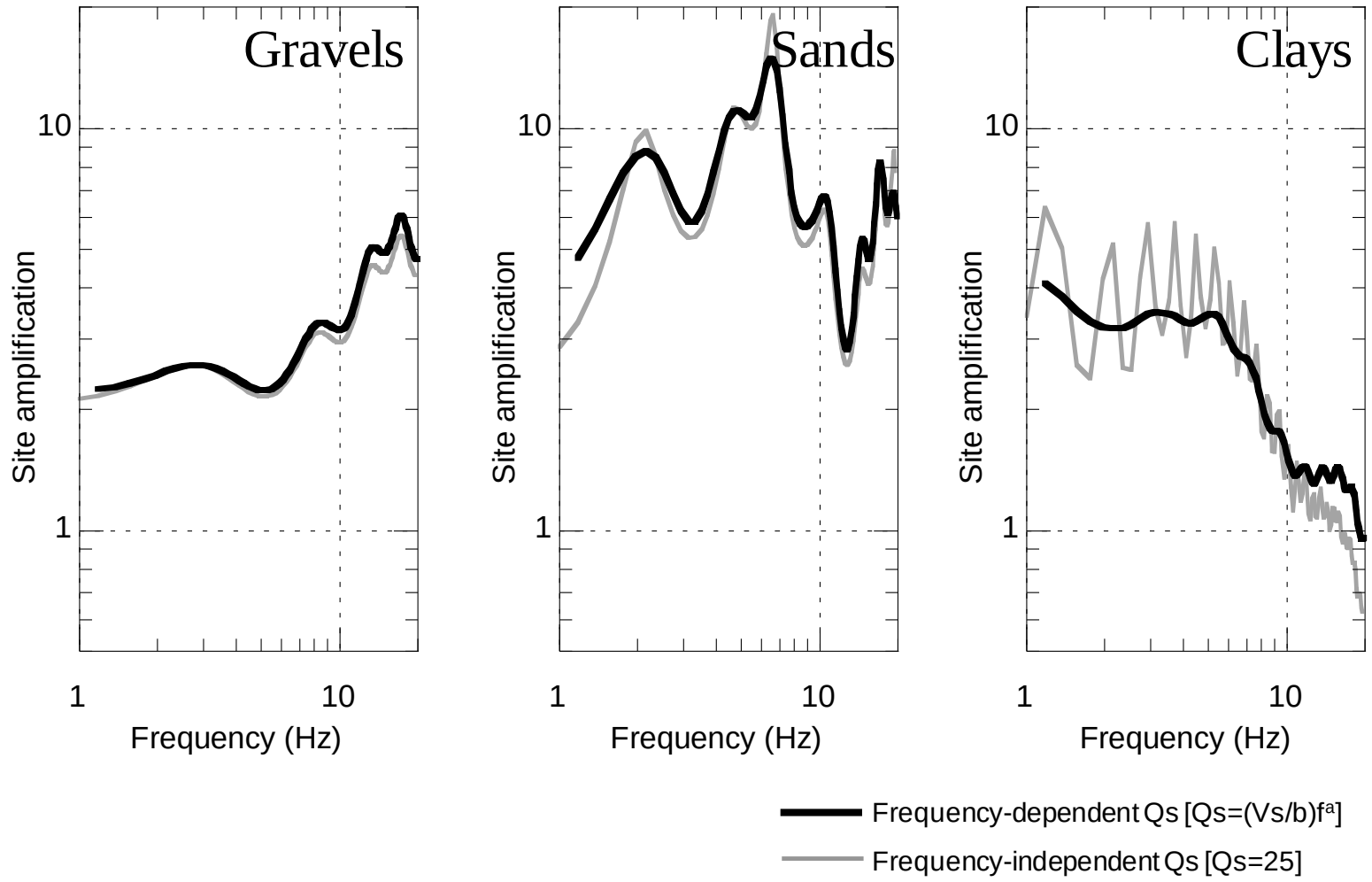

Figure 44. Comparison of theoretical transfer functions with Qs modeled as $Qs = (Vs/b)f^{a}$ represented by a black thick line, and frequency-independent Qs $(Qs = 25)$ represented by a grey thin line.

4.4 Contribution of the Shallow and Deep Structure on the Site Response

The observed site response evaluated from the Spectral Inversion Method contains the effect of the shallow and deep structure, since amplification is coming from the bottom layer with a S-wave velocity ~2200 m/s to the ground surface, as previously discussed in the Chapter 3 of the present thesis. The site amplification map of Lima has already been proposed by Sekiguchi et al. (2013) in the frequency range from 1 to 20 Hz. This map was constructed using a correlation between the Average Site Amplification (*AvSAF*) and the S-wave velocity for the first 10 m (*AVs10*), as shown in the Eq. 11:

$$AvSAF = 122/AVs10 + 0.76 \quad (11)$$

The parameter *AVs10* characterizes soil amplification for the shallow structure, indicating the site amplification map provides information about the contribution of the shallow structure on the site response at a site, represented as $AvSAF_{Shallow}$ in this study.

Calderon et al. (2012) and Quispe et al. (2014) determined the *AVs10* using the Vs profiles determined from the microtremor observations. This parameter is shown in Table 13. Table 9 displays there is a separation distance between the center of the array configuration and the earthquake station, indicating the *AVs10* determined by Calderon et al. (2012) and Quispe et al. (2014) is not the most suitable for the examined sites. In this section, the average value of shear-wave velocity from the surface to 10 m deep (*AVs10*) is computed using the new Vs models obtained by inverting the observed site response. The models have been shown in Figs. 41 (a2) ~ (p2) by black lines. These values are also shown in Table 13. Equation (11) has been used in order to compute the $AvSAF_{Shallow}$, using the *AVs10* determined by the new Vs profiles. $AvSAF_{Shallow}$ is also displayed in Table 13.

The Average Site Amplification in the frequency range from 1 to 20 Hz is also estimated using the observed site response, represented as $AvSAF_{S\&D}$ in Table 13. As

mentioned above, site response estimated in this study is affected by the shallow and deep structure.

The contribution of the deep structure on the site response $(AvSAF_{Deep})$ is also calculated, since this study evaluated how the top and deep layers control the amplification in the frequency range from 1 to 20 Hz ($AvSAF_{S\&D}$), while Sekiguchi et al. (2013) estimated soil amplification attributed to the shallow structure in the same frequency range ($AvSAF_{Shallow}$). Table 13 also displays the $AvSAF_{Deep}$ for each site, and these values are plotted together with the location of earthquake stations (blue triangles) on the soil distribution map of Lima (CISMID, 2005), as displayed in Fig. 45.

Figure 45 reveals the effect of deep structure on the site response is not related to the subsurface soil condition, but to the deep geology structure. For example, stations installed on clay deposits – located on the coastal area – show values of about zero, while sites located on gravels – represented by green color in the map – vary between ~1 and ~4. The author mentions the thickness of the clay deposits is large with a low S-wave velocity (Vs < ~500 m/s), and they overly layers with a S-wave velocity larger than ~1000 m/s, as shown in Fig. 43 (c). The high velocity contrast between the top and deep layers is the explanation of the large amplification at frequencies lower than 1 Hz, as previously reported by Repetto et al. (1980) and Calderon et al., (2012). Figure 45 shows $AvSAF_{Deep}$ has values of zero for stations installed on clays because the amplification at frequencies lower than 1 Hz is not considered in this study. These values might change if the average site amplification is calculated at frequencies lower than 1 Hz. The near surface attenuation is also another reason why the site response of clays at frequencies higher than 1 Hz is lower than sands and gravels. This study has already proved the attenuation effects on clays have a strong influence of the site response, as previously discussed in the section 4.3.

As an example, the Standard Spectral Ratio (SSR) technique (Borcherdt, R. D., 1970) is applied to calculate the spectral ratio for one station installed on clays (CAL), sands (RIN), and gravels (CMD) using the seismic event that occurred in 2008/03/29 12:51 with a local magnitude ML5.3 and a focal depth 51 km. This event was also recorded by the LMO station, the reference site in this study. Figure 46 reveals the

clay deposits (black solid line) suffer from much higher amplification than sands (grey dashed line) and gravels (grey solid line) in the frequency range between 0.1 and 1 Hz, while the sands and gravels mainly amplify at frequencies higher than 1 Hz.

Figure 47 shows the $AvSAF_{Deep}$ versus the depth – depth to the bottom layer with a S-wave velocity ~2200 m/s (open diamonds)– is plotted together with the Average Site Amplification in the frequency range from 0.1 to 1 Hz – using the results obtained from the spectral ratio – versus depth (solid points). A tendency toward a negative correlation of $AvSAF_{Deep}$ versus depth (black line) is obtained. The regression line between amplification estimated at low frequency (from 0.1 to 1 Hz) versus depth is not shown in Fig. 47 because of the limited number of data, but the gradient of the regression line is expected to be positive if average site amplification is evaluated at frequencies lower than 1 Hz. Table 13 also displays the values of the depth to the bottom layer with a S-wave velocity ~2200 m/s at each site. The values of Average Site Amplification in the frequency range from 0.1 to 1 Hz computed from the SSR for the three analyzed sediment sites, as well as the depth to the bottom layer with a Vs ~2200 m/s are shown in Table 14, these results might be used as a reference for analyzing the site response at frequencies lower than 1 Hz in the future.

Table 13. Estimation of the contribution of the shallow and deep structure on the site response.

Sediment site	AVs10 Calderon et al. (2012) Quispe et al. (2014)	AVs10 by inverting the Observed Site Response	Frequency range 1 - 20 Hz			Depth to the layer with a Vs ~2200 m/s
			$AvSAF_{S\&D}$	$AvSAF_{Shallow}$	$AvSAF_{Deep}$	
CSM	436.49	489.93	5.81	2.02	3.79	140
MOL	N/A	431.91	4.67	2.08	2.59	33
CER	434.33	781.28	2.68	1.83	0.85	421
UNI1	N/A	470.80	5.24	2.04	3.20	443
UNI2	N/A	463.86	5.92	2.05	3.88	404
UNI3	N/A	547.61	4.61	1.97	2.65	141
UNI4	N/A	497.60	5.15	2.01	3.14	234
PQR	452.90	645.52	3.80	1.90	1.91	166
SMP	N/A	539.41	4.78	1.97	2.81	236
ANC	282.83	379.08	7.34	2.16	5.18	91
RIN	294.33	207.80	11.65	2.69	8.96	65
MAY	474.00	685.34	3.40	1.88	1.52	72
VSV	355.31	312.36	9.64	2.30	7.34	591
PPI	228.13	192.36	8.05	2.79	5.26	116
CMA	238.55	249.04	2.00	2.50	-0.50	613
CAL	278.54	392.51	2.44	2.14	0.29	416

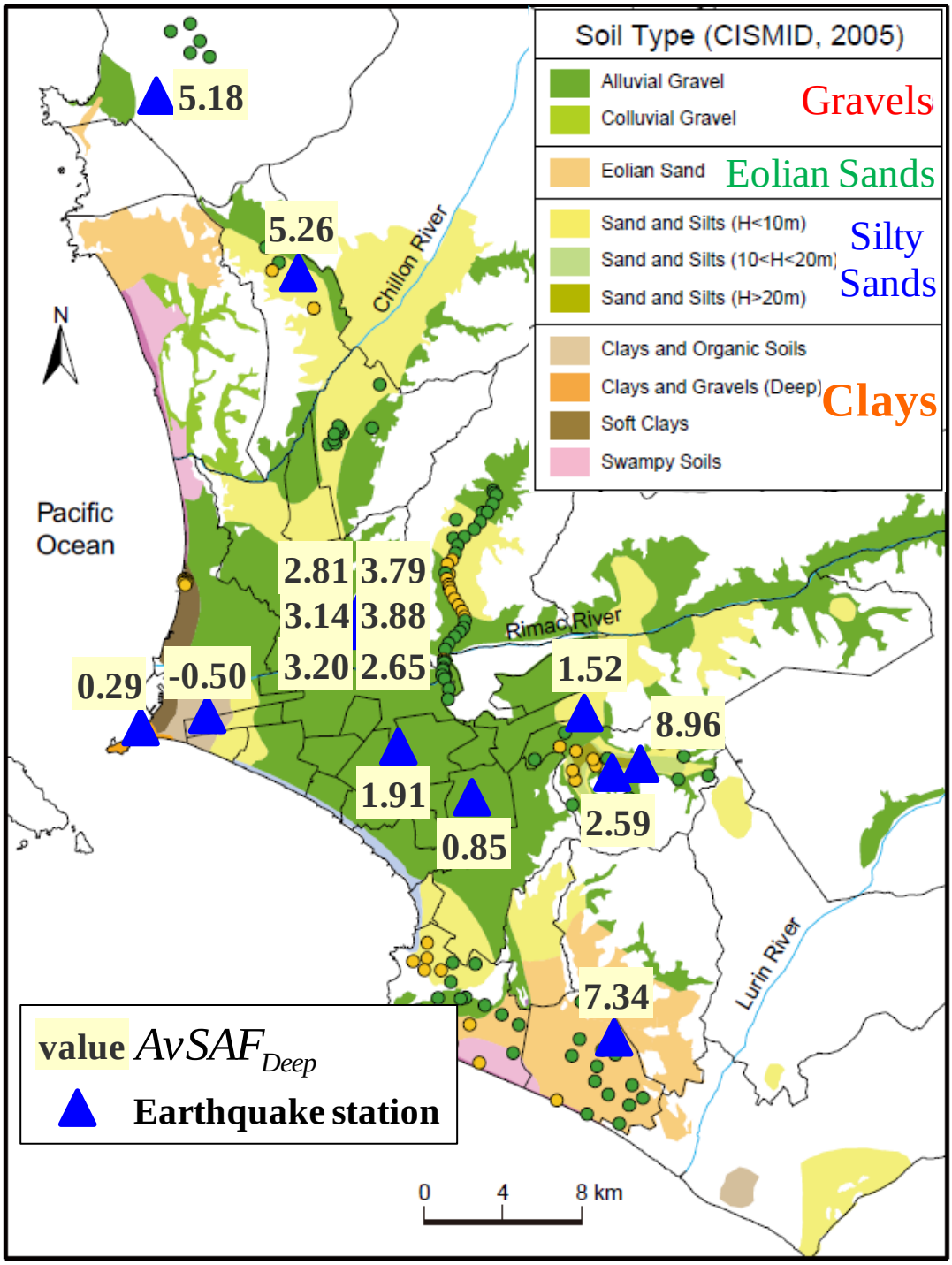

Figure 45. The contribution of the deep structure on the site response $(AvSAF_{Deep})$ has been computed, and this value is shown with the location of the earthquake station (blue triangles) on the soil distribution map of Lima Metropolitan Area (CISMID, 2005).

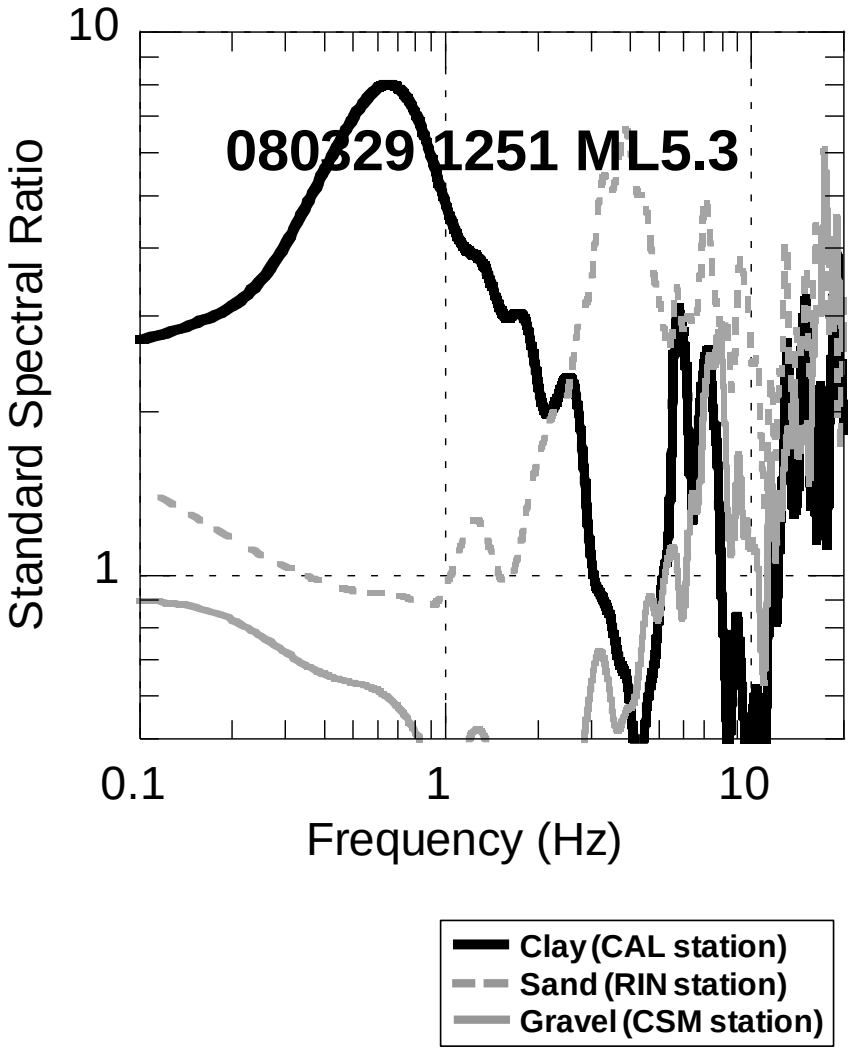

Figure 46. Calculation of the Standard Spectral Ratio technique (Borcherdt, R. D., 1970) for earthquake stations installed on clays (CAL site), sands (RIN site) and gravels (CDLCIP site). The reference site has been the rock station coded LMO. The earthquake used in the calculation was the 2008/03/29 12:51 with a local magnitude ML5.3 and focal depth 51 km. The solid black, dashed and solid grey lines represent the spectral ratio for stations situated on clays, sands, and gravels.

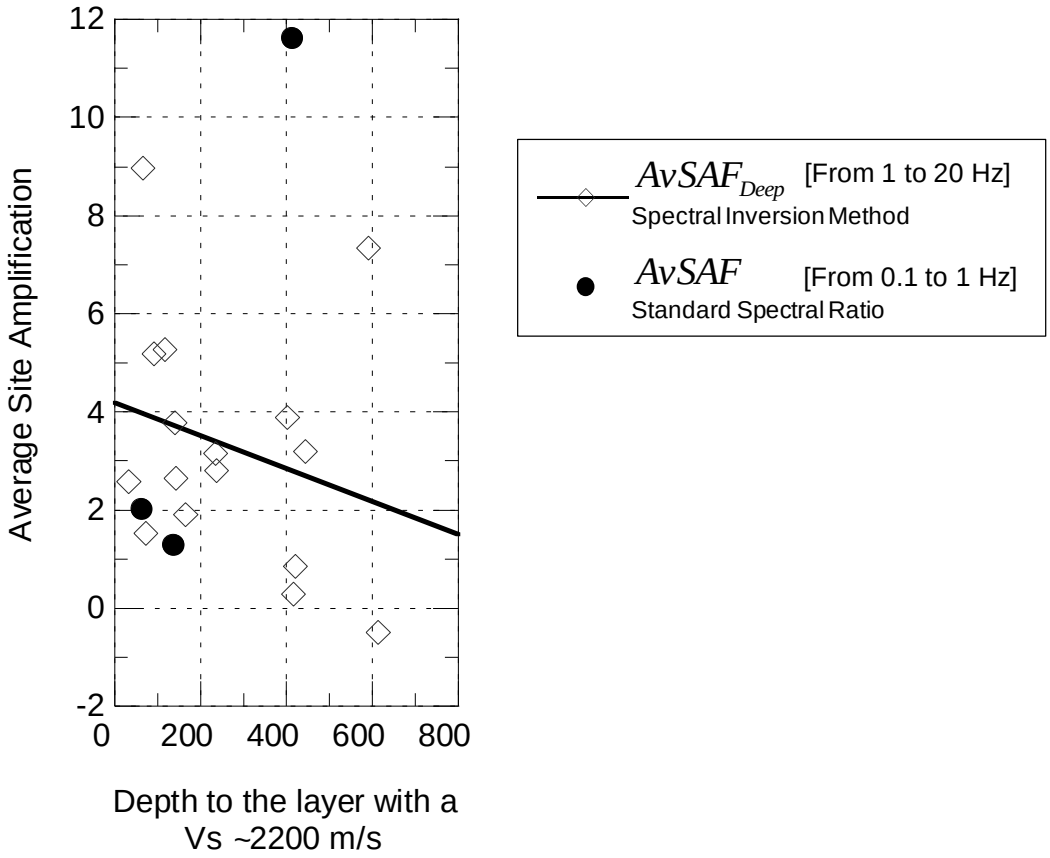

Figure 47. Average Site Amplification attributed to the deep structure in the frequency range from 1 to 20 Hz $\left(AvSAF_{Deep}\right)$ is plotted versus the depth to the bottom layer with a Vs ~2200 m/s. The open diamonds represent the $AvSAF_{Deep}$ versus depth, and the regression line of these results is represented by a black line. The average site amplification in the frequency range from 0.1 to 1 Hz – computed from the results obtained from the Standard spectral Ratio – versus depth are also plotted in the figure, represented by solid points.

Table 14. Average Site Amplification in the frequency range from 0.1 to 1 Hz – using the results obtained from the Standard Spectra Ratio technique shown in Fig. 46.

Sediment site	**Standard Spectral Ratio AvSAF 0.1 - 1 Hz**	**Depth to the layer with a Vs ~2200 m/s**
CSM	1.25	140
RIN	1.98	65
CAL	11.59	416

CHAPTER 5

CONCLUSIONS AND FUTURE TAKS

5.1 Conclusions

5.2 Future tasks

5.1 Conclusions

- This study contributes to the state of the art of Earthquake engineering as it exists in Peru today. Several limitations – such as the lack of data as well as the access to it – have been overcome in this study in order to have a comprehensive understanding and characterization of local site amplification in Lima Metropolitan Area. Outcomes from this research are expected to be used for updating the zonation map of Lima (CISMID, 2005; 2010).
- Field observations were carried out in order to estimate the S-wave velocity profiles at six selected sites, based on the location of strong motion stations. Five stations are located on sedimentary layers –gravels and sands, while one station is installed on outcropping hard rock.
- This study succeeded to estimate the Vs profiles at the five sediment sites, but also this work defined the S-wave velocity ranges for the different subsurface soil conditions over Lima. These Vs ranges were defined using the results obtained from the microtremor measurements conducted in this study as well as results from previous studies (Calderon et al., 2012). This study indicates the gravel deposits have S-wave velocities ranging from ~400 to ~1500 m/s – gradually increasing with depth. The sand deposits have S-wave velocities between ~100 and ~500 m/s, and the Vs of the clay deposits is ranging within ~200 and ~500 m/s.
- The Vs structure at one station located on rock was determined in this study too, information previously unknown. The profile reached a depth of ~30 m, where the bottom layer has a S-wave velocity of about ~2200 m/s. In this study, the rock station coded LMO was the only site located on rock. This station was chosen as the reference site for evaluating the site response in Lima Metropolitan Area. That is why this information was pivotal in this research.
- This study succeeded to gather earthquake records, pivotal information for the evaluation of observed site amplification. Several requests and activities were made more than one year before this doctoral program started in 2012. One of them was to have open access to the seismic records, since most of them are not

available to the public. The installation of new earthquake recording stations (totally 10 equipments) was also made as part of this study, and the author was mainly involved too. The collection of the earthquake data – that started before this doctoral program – has also been a big effort in this study. Without this information, this study would not have important contributions to the state of the art of Earthquake Engineering as it exists in Peru today.

- The observed site response was evaluated by applying the Spectral Inversion Method in the frequency range from 1 to 20 Hz. This study applied this technique because is one of the most appropriate and accurate techniques for analyzing site amplification. Amplification estimated in this study is only attributed to the effect of sedimentary soil layers over a basement with a S-wave velocity ~2200 m/s, indicating the site response is affected by the shallow and deep structure. Previous studies (Calderon et al., 2012; Sekiguchi et al., 2013, Quispe et al., 2012) have had the limitation of understanding how the sedimentary layers control the amplification because of the lack of knowledge, the limitation in data, and the access to it. This study overcomes such limitations and presents new results that were previously unknown in Lima Metropolitan Area.
- This study characterizes the site response for the different subsurface soil formations over Lima Metropolitan Area such as gravels, sands, and clays. Stations installed on gravel deposits shows the gravel deposits tend to amplify at frequencies higher than 3.0 Hz, confirming what previously was reported by Quispe et al. (2013, 1014). This material has S-wave velocities increasing gradually with depth from ~400 to ~1500 m/s. Deposits of sand (Vs between ~100 and ~500 m/s) overlying gravel deposits respond with high amplification at frequencies higher than 5.0 Hz, while the deep layers (Vs > ~800 m/s) underlying the sand deposits influence significantly at frequencies lower than 5.0 Hz, attributed to the velocity contrast between the shallow and deep layers. Stations located on clay deposits also control the amplification in a wide frequency range, but the amplification spectrum increases in amplitude from high to low frequency. Large amplification at frequencies lower than 5 Hz is

attributed to the high velocity contrast between the clay deposits (Vs varying within ~200 and ~500 m/s) and the deep layers with a Vs > 1000 m/s.

- The observed site response estimated in this study reveals areas underlie sands and clays suffer from site effect, explaining the excessive earthquake damage previously observed in areas such as La Molina district and Callao province. This study also contributes to the understanding of local site effects in areas such as Villa El Salvador, Ancón and Puente Piedra districts, places where the dynamic information is still scarce, so the soil distribution and microzonation maps should be updated using as a reference this work.
- Path and source parameters were also evaluated in this work. The estimated Qs-value of the propagation path is modeled as $95.6f^{0.66}$ for the crust and mantle. Source factors – such as seismic moment M_0 and corner frequency f_c – were also calculated for each earthquake used – totally 55 seismic events. The slope obtained from fitting M_0 and f_c yields a value of -3.82.
- The quality factor Qs as a function of frequency f and S-wave velocity Vs was estimated for the different subsurface soil conditions over Lima. This parameter controls the amplification together with the S-wave velocity. The frequency-dependent Qs was unknown in Lima. Previous studies (Calderon et al., 2012; Quispe et al., 2014) made the assumption that Qs is independent of frequency. This study proves this parameter Qs has a strong influence on the site response together with the S-wave velocity distribution, especially areas underlie clays.
- In this study, the frequency-dependent Qs was estimated by inverting the observed site amplification obtained from the Spectral Inversion Method. Qs was modeled as a function of frequency f and Vs $Qs = (Vs/b)f^a$. Parameters a and b were estimated from the inversion. The frequency-dependent Qs was classified into three groups based on the main soil formations over Lima Metropolitan Area – gravels, sands, and clays. This study indicates b value for gravels and clays are similar each other and also much larger than sands, while this material presents the higher a value compared to gravels and clays.
- This study reveals the frequency-dependent Qs has strong influence on clays deposits, while the effect on gravels and sand is negligible. This conclusion

indicates the importance of knowing the quality factor for the evaluation of site response, especially for clay deposits in Lima Metropolitan Area.

5.2 Future Tasks

1. Small and large microtremor measurements were conducted at Lima Metropolitan Area in order to characterize the shallow and deep layers (Calderon et al., 2012; Quispe et al., 2014). Few S-wave velocity profiles detected the seismic bedrock (Vs ~3000 m/s), because the coherence calculated from most of the large arrays were very low at low frequency, that it was not possible to use the data from them. The map for the depth to the seismic bedrock is still unknown for Lima because of the above-mentioned reasons. Nonetheless, a preliminary conclusion using the available information (Calderon et al., 2012; Quispe et al., 2014) shows the basement with a S-wave velocity ~3000 m/s is shallower in gravel deposits than sands and clays, as shown in Fig. 22. The map for the depth to the seismic bedrock should be proposed in order to know the distribution of the sedimentary layers over the basement (Vs ~3000 m/s) in Lima.
2. Most of the analyzed earthquakes in this study were small events with a length of S-waves from 2 to 4 s, offering a low resolution for frequencies lower than 1 Hz, that is why this study just analyzed the site response in the frequency range from 1 to 20 Hz. Nevertheless, previous studies (Repetto, et al., 1980; CISMID, 2005; Calderon et al., 2012) have reported large amplification for frequencies lower than 1 Hz is expected for areas underlie clays. As evidence, this study applied the Standard Spectral Ratio technique (Borcherdt et al., 1970) using the earthquake record from 2008/03/29 12:51 (ML5.3 and depth 51 km) as show in Fig. 46. Figure 46 proves areas underlying clays suffer from much higher amplification at frequencies lower than 1 Hz than gravels and sands. This study stresses the importance of

analyzing the site response at frequencies lower than 1 Hz for the prediction of long period ground motions in Lima Metropolitan Area.

3. New contributions in relation to the site response have been obtained in this study such as the observed site response, S-wave velocity distribution and frequency-dependent quality factor Qs. These outcomes should be used as a reference for updating the Zonation Map of Lima Metropolitan Area (CISMID, 2005; 2010) as a future work.
4. This study cannot still explain the discrepancies between S-wave velocity obtained from microtremor data and the new Vs model computed by inverting the observed site response for CER and PQR stations. It is recommended to reanalyze this information by using different techniques in order to confirm or discuss the results obtained in this study.

REFERENCES

Aguilar, Z., 2005 Seismic Microzonation of Lima, Japan-Peru Workshop on Earthquake Disaster Mitigation, Japan-Peru Center for Earthquake Engineering and Disaster Mitigation (CISMID), Faculty of Civil Engineering, National University of Engineering, Lima, Peru.

Aki, K., 1957 Space and Time Spectra of Stationary Stochastic Waves, with Special Reference to Microtremors, Bulletin of the Earthquake Research Institute, Vol. 35, pp. 415–457.

Bill Stephenson, W. R., Benites, R. A., and Davenport, P.N., 2009 Localised Coherent Response of the La Molina basin (Lima, Peru) to earthquakes, and Future Approaches suggested by Parkway basin (New Zealand) experience, Soil Dynamics and Earthquake Engineering , Vol. 29, pp. 1347–1357.

Borcherdt, R. D., 1970 Effects of Local Geology on Ground Motion near San Francisco Bay, Bulletin of the Seismological Society of America, Vol. 60 No. 1, pp. 29–61.

Brune, J. N., 1970 Tectonic Stress and the Spectra of Seismic Shear Waves from Earthquakes, Journal of Geophysical Research, Vol. 75, No. 26, pp. 4997 – 5009.

Cabrejos, H., 2013 Amplificación Sísmica en la Ciudad de Lima aplicando la técnica de Cocientes Espectrales, Facultad de Ingeniería Civil, Universidad Nacional de Ingeniería, Lima, Peru (In Spanish).

Calderon D., 2012 Dynamic Characteristics of the Soils in Lima, Peru, by estimating Shallow and Deep Shear-wave velocity profiles, Graduate School of Engineering, Chiba University, Japan.

Calderon, D., Sekiguchi, T., Nakai, S., Aguilar, Z., and Lazares, F., 2012 Study of Soil Amplification Based on Microtremor and Seismic Records in Lima Peru, Journal of Japan Association for Earthquake Engineering, Vol. 12, No. 2, pp. 1-20.

CISMID, 2005 Study of the Vulnerability and Seismic Risk in 42 districts of Lima and Callao, Japan - Peru Center for Earthquake Engineering Research and Disaster Mitigation, National University of Engineering, Lima, Peru, (in Spanish).

CISMID, 2010 Seismic Microzonation of 6 districts in Lima, Japan - Peru Center for Earthquake Engineering Research and Disaster Mitigation, National University of Engineering, Lima, Peru, (in Spanish).

Dorbath, L., Cisternas, A., and Dorbath, C., 1990 Assessment of the Size of Large and Great Historical Earthquakes in Peru, Bulletin of the Seismological Society of America, Vol. 80, No. 3, pp. 551-576.

Espinoza, A. F., Husid, L. R., Algermissen, S. T. and De Las Casas, J., 1977 The Lima earthquake of October 3, 1974: Intensity Distribution, Bulletin of the Seismological Society of America, Vol. 67, No. 5, pp. 1429–1439.

Grutas, R. N. and Yamanaka, H., 2012 Shallow Shear-wave Velocity Profiles and Site Response Characteristics from Microtremor Array Measurements in Metro Manila, The Philippines, Exploration Geophysics, CSIRO Publishing, dx.doi.org/10.1071/EG12031.

Hayashi, K., 2008 Development of the Surface-wave methods and Its Application to Site Investigations, Kyoto University, Japan.

Husid, L. R., 1969 Características de Terremotos – Análisis General, Revista del IDIEM 8, pp. 21–42, Santiago, Chile, (In Spanish).

Instituto Nacional de Estadística e Informática (INEI), 2008 PERÚ: Perfil Sociodemográfico, (In Spanish).

Instituto Nacional de Estadística e Informática (INEI), 2012 Perú: Estimaciones y Proyecciones de Población Total por Sexo de las Principales Ciudades, (In Spanish).

Iwata, T., and Irikura, K., 1988 Source parameters of the 1983 Japan Sea Earthquake sequence, Journal of Physics of the Earth, Vol. 36, pp. 155-184.

Jordan, T., Isacks, B., Allmendinger, R., Brewer, J., Ramos, V., and Ando, C., 1983 Andean Tectonics related to Geometry of Subducted Nazca Plate, Geological Society of America Bulletin, Vol. 94, Issue 3, pp. 341–361.

Kanamori, H., 1972 Mechanism of Tsunami Earthquakes, Phys. Earth Planet. Inter., 6, pp. 346–359.

Kitsunezaki, C., Kobayashi, Y., Ikawa T., Horike M., Saito T., Kurota T., Yamabe K., and Okuzumi K., 1990 Estimation of P- and S-wave velocities in Deep Soil Deposits for evaluating Ground Vibrations in Earthquake, Journal of the Japan Society for Natural Disaster Science, Vol.9, No.3, pp. 1-17.

Lawson, C. L. and Hanson, R. J., 1974 Solving Least Squares Problem, New Jersey: Prentice-Hall, Inc., Englewood Cliffs, 1–337.

Le Roux, J. P., Tavares, C., and Alayza, F., 2000 Sedimentology of the Rímac-Chillón alluvial fan at Lima, Peru, as related to Plio-Pleistocene sea-level changes, glacial cycles and tectonics, Journal of South American Earth Sciences, 13, pp. 499–510.

Lermo, J., and Chávez-García, F. J., 1993 Site Effects Evaluation using Spectral Ratios with Only One Station, Bulletin of the Seismological Society of America, Vol. 83, pp. 1574–1594.

Lin, C., Chang, C., and Chang, T., 2004 The use of MASW method in the Assessment of Soil Liquefaction Potential, Soil Dynamics and Earthquake Engineering, Vol. 24, pp. 689 – 698.

McCann, M. W. J., and Shah, H. C., 1979 Determining Strong Motion Duration of Earthquakes, Bulletin of Seismological Society of the America, Vol.69, pp. 1253–1265.

Martínez, A., and Porturas, F., 1975 Planos Geotécnicos para Lima, Perú, Análisis y Visión en Ingeniería Sísmica, Pontificia Universidad Católica del Perú, Lima, Perú, (In Spanish).

Pulido, N., Tavera, H., Aguilar, Z., Calderón, D., Chlieh, M., Sekiguchi, T., Nakai, S., and Yamazaki, F., 2012 Mega-Earthquakes Rupture Scenarios and Strong Motion Simulations for Lima, Peru, The International Symposium for CISMID 25th Anniversary Technological Advances and Learned Lessons from Last Great Earthquakes and Tsunamis in the World, Paper No. TS-6-2, Lima, Peru.

Repetto, P., Arango, I., and Seed, H. B., 1980 Influence of Site Characteristics on Building Damage during the October 3, 1974 Lima Earthquake, Report-Earthquake Engineering Research Center, College of Engineering, University of California, Berkeley, California, EERC-80/41.

Riepl, J., Bard, P.-Y., Hatzheld, D., Papaionnou, C., and Nechtschein, S., 1998 Detail Evaluation of Site-Response Estimation Methods across and along the Sedimentary Valley of Volvi (EURO-SEISTEST), Bulletin of the Seismological Society of America, Vol. 88, No. 2, pp. 488–502.

Okada, H., 2003 The Microtremor Survey Method, Geophysical Monograph Series No. 12, Society of Exploration Geophysicists.

Park, C. B., Miller, R. D. and Xia, J., 1999a Multimodal Analysis of High Frequency Surface Waves, Proceedings of the Symposium on the Application of Geophysics to Engineering and Environmental Problems, pp. 115-121.

Sekiguchi, T., Calderon, D., Nakai, S., Aguilar, Z., and Lazares, F., 2013 Evaluation of Surface Soil Amplification for Wide areas in Lima, Peru, Journal of Disaster Research, Vol. 8 No. 2, pp. 259-265.

Sladen, A., Tavera, H., Simons, M., Avouac, J. P., Konca, A. O., Perfettini, H., Audin, L., Fielding, E. J., Ortega, F., and Cavagnoud, R., 2010 Source Model of the 2007 Mw 8.0

Pisco, Peru Earthquake: Implications for Seismogenic Behavior of Subduction Megathrusts, Journal of Geophysical Research, Vol. 115, B02405, doi:10.1029/2009JB006429.

Takemura, M., Ikeura, T., and Sato, R., 1990 Scaling Relations for Source Parameters and Magnitude of Earthquake in the Izu Peninsula Region, Tohoku Geophys. J. (Sci. Rep. Tohoku Univ., Ser. 5), Vol.32, pp. 77–89.

Takemura, M., Kato, K., Ikeura, T., and Shima, E., 1991 Site Amplification of S-waves from Strong Motion Records in Special Relation to Surface Geology, Journal of Physics of the Earth, Vol. 39, pp. 537–552.

Yamanaka, H., Nakamura, A., Kurita, K., and Seo, K., 1998 Evaluation of Site Effects by an Inversion of S-Wave Spectra with a Constraint Condition considering Effects of Shallow Weathered Layers, Zisin (Journal of the Seismological Society of Japan), Vol. 51, pp. 193 – 202, (In Japanese with English Abstract).

Yamanaka, H., 2005 Comparison of performance of heuristic search methods for phase velocity inversion in shallow wave methods, Journal of Environmental & Engineering, Vol. 10, pp. 163–173, doi:10.2113/JEEG10.2.163.

Yamanaka, H., 2007 Inversion of Surface-Wave Phase Velocity using Hybrid Heuristic Search Method, Butsuri Tansa, Vol. 60, No.3, pp. 265–275 (In Japanese with English abstract).

Yamanaka, H., Ohtawara, K., Grutas, R., Tiglao, R. B., Lasala, M., Narag, I. C., Bautista, B. C., 2011 Estimation of Site Amplification and S-Wave Velocity Profiles in Metropolitan Manila, the Philippines, from Earthquake Ground Motion Records, Exploration Geophysics, Vol. 42, pp. 69–79.

Yamazaki, F. and Zavala, C., 2013 SATREPS Project on Enhancement of Earthquake and Tsunami Disaster Mitigation Technology in Peru, Journal of Disaster Research, Vol. 8 No. 2, pp. 224-234.

Zaineh H., Yamanaka H., Dakkak R., Khalil A., and Daoud M., 2012 Estimation of Shallow S-Wave Velocity Structure in Damascus City, Syria, Using Microtremor Exploration, Soil Dynamics and Earthquake Engineering, Vol. 39, pp. 88 – 99.